Computational study on the early stages of the Methanol to Hydrocarbons process

Ștefan Adrian F. Năstase

Department of Computational Chemistry
Cardiff University

Supervisor: Professor C.R.A. Catlow

Second Supervisor: Dr. A.J. Logsdail

Abstract

The Methanol-To-Hydrocarbons (MTH) process is a very important step to produce a wide range of hydrocarbons such as fuel and olefins from various carbon sources. In this thesis, the focus is on understanding the nature of the active sites and reactions occurring in the initial stages of the MTH process by means of state-of-the-art simulation techniques, with the aim of determining the conditions enhancing the conversion rate of methanol and controlling the overall product selectivity.

The initial methanol adsorption stage in H-ZSM-5 and H-Y was studied using QM/MM static calculations. Adsorption and methoxylation energies were calculated and shown the H-ZSM-5 sites were achieved a higher adsorption and lower methoxylation energies than those of H-Y. Furthermore, after the formation of the hydrogen bonding network between the reactant and an addition polar molecule, a barrierless Brønsted proton transfer was observed. The nature and adsorption properties of the zeolite active sites were further analysed by using Molecular Dynamics and Metadynamics simulations. Our analysis proved the concerted effect that occurs when having vicinal Brønsted acid sites in the zeolite catalyst and highlighted the improved catalytic activity of such a configuration as opposed to a single acid site. The reactivity of the methoxy groups was analysed with QM/MM simulations, by determining the energy to migrate from one active site or directly form carbene with both pathways proving to be energetically demanding. An additional methanol reaction pathway to dimethyl ether (DME) was simulated with QM/MM methods. The type of active sites and orientation of DME were shown to significantly influence the stability of DME and are projected to further influence the conversion rate of the MTH process.

This thesis illustrates the power of complementary computational studies of sorbate reactivity in zeolites, with future work aiming to incorporate these studies into improving different microporous catalytic processes.

Contents

Chapter 1. Methanol to Hydrocarbons process catalysed by zeolites 1
- 1.1 Zeolites structure and functionality 1
- 1.2 Methanol to Hydrocarbons process 3
  - 1.2.1 Induction period. First C-C bond formation 4
  - 1.2.2 Steady state reaction 8
  - 1.2.2.1 Dual cycle mechanism 8
    - 1.2.2.2 Influence of zeolite type on product selectivity 10
  - 1.2.3 Deactivation stage 11
- 1.3 Studies of the initial stages of the MTH process 12
- 1.4 Hypothesis, Objectives and Structure 14

Chapter 2. Computational Methods 17
- 2.1 Embedded-cluster QM/MM calculations 17
  - 2.1.1 Molecular mechanics 18
    - 2.1.1.1 Intra, Inter-atomic potentials 18
  - 2.1.2 Electronic methods 21
    - 2.1.2.1 Density Functional Theorem 24
    - 2.1.2.1.1 Exchange Correlation functionals for DFT 25
    - 2.1.2.1.2 Dispersion corrections of DFT 26
    - 2.1.2.2 Møller–Plesset perturbation theory 28
    - 2.1.2.3 Basis sets 29
    - 2.1.2.4 Plane wave basis sets 31
    - 2.1.2.5 Periodic boundary conditions 32
  - 2.1.3 QM/MM 33
  - 2.1.4 Energy minimisation methods 35
  - 2.1.5 Transition state calculations 38
    - 2.1.5.1 Nudged elastic band method for finding minimum energy paths 38
    - 2.1.5.2 Dimer method 40
- 2.2 Periodic Ab Initio Molecular Dynamics 41
  - 2.2.1 Molecular dynamics 41
    - 2.2.1.1 Integration Algorithms 42
    - 2.2.1.2 Microcanonical ensembles 43

2.2.1.2.1 NVT ensemble 44
2.2.1.2.2 NPT ensemble 45
2.2.2 Metadynamics 46
2.2.3 Equilibration and production run.. 48
2.3 Resources 48

Chapter 3. Computational QM/MM investigation of the adsorption of MTH active species in H-Y and H-ZSM-5 51
3.1. Introduction 52
3.2. Methodology 53
3.2.1 Models 53
3.2.2 Energetic analysis 56
3.2.3. Electronic Parameters Analysis 58
3.3. Results and Discussion 58
3.3.1 Adsorption of methanol 58
3.3.2 Bi-methanol systems 66
3.3.3 Adsorption of methanol in presence of alternative molecular species 79
3.3.4. Electronic Parameters Analysis 86
3.3.5. Vibrational analysis of adsorbed methanol 89
3.4. Summary and Conclusions 95

Chapter 4. Acid site configuration analysis within the MTH process using AIMD simulations 99
4.1. Introduction 100
4.2. Methodology 101
4.2.1 Catalyst model 101
4.2.2 Structural analysis 104
4.2.3 Metadynamics 110
4.3. Results and discussion 117
4.3.1 Methanol dynamics at room temperature 117
4.3.2 Framework methylation 127

Chapter 5. QM/MM study of zeolite bound methoxy groups reactivity 135
5.1. Introduction 136

5.2. Methodology 137

5.2.1. Model description.. 137

5.2.2. Energy analysis 138

5.3. Results 138

5.3.2. Methyl migration away from the active site 142

5.3.3. Carbene migration.. 146

5.4. Conclusions.. 150

Chapter 6. QM/MM study on the stability and formation of dimethyl ether in zeolites H-Y and H-ZSM-5 152

6.1. Introduction.. 153

6.2. Methodology 154

6.3. Results 155

6.3.1. Adsorption of DME.. 155

6.3.2. Vibrational frequency analysis 160

6.3.3. Formation of DME 162

6.4 Conclusions... 165

Chapter 7. Summary, conclusions and future work 167

Summary, conclusions and future work.. 168

Chapter 1. Methanol to Hydrocarbons process catalysed by zeolites

The acid site distribution in zeolites as well as the nature of the active sites and adsorption properties has been the topic of considerable research in many fields particularly the petrochemistry and oil refining industries with the Methanol-to-Hydrocarbons (MTH) process.

In particular, it has proven difficult to experimentally characterize and determine the mechanism behind methanol activation in the initial stages of the MTH process, due to the complex nature of the chemical environment. Theory should provide support for these experiments, with modern computational modelling approaches now allowing the accurate prediction of the structure-property relationships and kinetic factors, but the limited discussion in the literature to date highlights how poorly understood the MTH process remains. In this thesis, the catalytic activity of Brønsted acid sites in zeolites was studied by the conversion of methanol over zeolites with varying reactant loadings and Si/Al ratios, to develop an improved understanding of methanol reactivity in the industrially relevant Methanol-to-Hydrocarbons process.

1.1 Zeolites structure and functionality

Zeolites or aluminosilicates are crystalline aluminosilicates made from interlinked tetrahedra of alumina (AlO_4) and silica (SiO_4) with the general formula $M_{x/n}[(AlO_2)_x(SiO_2)_y]\cdot mH_2O$, where M is the cation inserted to counter the negative charge created by the presence of Al^{3+} in the AlO_2 structure, alongside SiO_2. “M” can be a hydrogen cation or metal cation of valency “*n*”, ensuring Brønsted or Lewis acidity.[1,2] Aluminosilicates are formed by polymerisation of SiO_4 and AlO_4 tetrahedra leading to building blocks such as the 5 membered ring pentasil and 6 membered ring sodalite units. These units form periodic frameworks connected through bridging oxygen bonds in different vertices of the building blocks. Due to the different possible links that can be made between the building blocks, a wide range of structures can be formed with cages interconnected trough channels of molecular dimensions, oriented in one, two or three directions,[3] also described in Figure 1.1. The myriad of structures available and easy tuneable composition result in a set of properties that ensure numerous applications.[3]

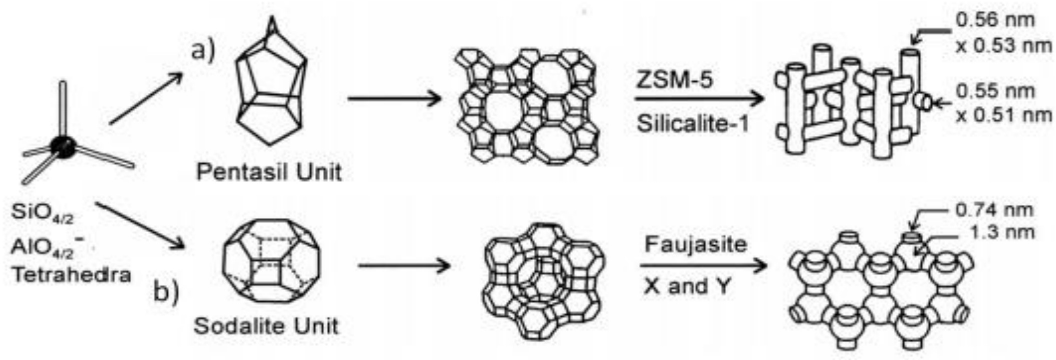

Figure 1.1. Schematics of the framework structures of a) MFI structure, ZSM-5 type and b) FAU structure, zeolite Y type and their composite building units formed from the TO_4 *tetrahedron. Figure adapted with permission from reference Weitkamp et al*[4].

The high thermal stability, 400 °C to 800 °C, depending on the counter-cations inserted and high surface area, in the range of 600-800 m^2/g, of zeolites grants the ability to absorb large quantities of adsorbate depending on reactant size, temperature and acidity of zeolites.[5,6] Also, because the absorption can be exothermic, aluminosilicates are employed as “heat batteries”, used to conserve and further transfer heat, typically in industrial factories.[7] The acidity of zeolites, specifically the Brønsted acid sites, are integral for the processes in the petrochemical industry. The OH bridging framework acts as the Brønsted acid site that can catalyse several petrochemical processes such as catalytic cracking[8] and the methanol to hydrocarbons process,[9,10] with the latter being the main focus of this thesis. The Brønsted proton can be donated to olefins or methanol thus polarising certain bonds and activating the reactant. In this manner, the reaction rate towards the formation of different hydrocarbons is increased.

Furthermore, the ordered and unique pore structure can ensure shape selectivity properties, useful to control the diffusion of reactants/products inside or out of the pores.[3,11] This property can be particularly useful in controlling the selectivity of different catalytic processes, as will be discussed later. Apart from structure dependent properties, the acidity of zeolites, specifically the Brønsted acid sites, are integral to the processes in the petrochemical industry. The OH bridging framework acts as the catalytic site used for several petrochemical processes such as catalytic cracking[8] and the methanol to hydrocarbons process,[9,10] with the latter being the main focus of this thesis.

1.2 Methanol to Hydrocarbons process

Continued demand for low-cost energy, coupled with decreasing natural fossil fuel reserves, has motivated an intensive scientific search for alternative energy sources to those our society has become dependent on.[12] Of the various energy sources under current consideration, the synthesis of liquid fuel from coal, biomass and other sources could play a key role in supplying affordable, portable energy prior to the expected uptake of completely renewable energy. To make the target hydrocarbons, one can use either the Fischer-Tropsch[13] or methanol-to-hydrocarbons (MTH) processes [9,10] after the initial gasification of the coal.

The use of methanol, obtained from a wide range of raw materials (biomass, synthesis gas, or carbon dioxide), to form olefins, aromatics or gasoline, made the Methanol-to-Hydrocarbons (MTH) process a viable alternative to the classical production routes. Development of the MTH process was led by Silvestri and Chang at the Mobil Company, whose studies on the methylation of isobutane concluded that the zeolitic material H-ZSM-5 can catalyse the formation of higher olefins and aromatics.[14] These observations initiated sustained industrial and academic investigations of the MTH process in zeolites,[15] which identified that the first step is dehydration of the methanol to form framework-bound methoxy- species; subsequently, dimethyl ether (DME), ethene, higher olefins and aromatics are all formed.

Currently, there is broad agreement on the general aspects of the successive steps taking place during the MTH chemistry. The MTH process has an induction period that is characterized by the low reactivity of methanol in the beginning of the process until certain "hydrocarbon pool" (HP) species are formed, which themselves act as a co-catalyst.[16,17,18] Depending on the various zeolite topologies and reaction conditions, a broad spectrum of HP species may be formed[19] that can also impact the deactivation rate, as will be further outlined bellow.

1.2.1 Induction period. First C-C bond formation

The initial stage in the MTH process is characterised by an induction period, in which the methanol conversion rate is low.[20,21] Several factors are suggested to influence the induction period, such as the presence of water[22] and a high reactant contact time with the catalyst.[23] Water is in a competitive adsorption equilibrium with methanol on the zeolite active sites and can determine the reverse reaction from methoxy back to methanol, limiting the progress of the process. However, water can also stabilise certain carbocationic intermediates that are crucial to the MTH process.[22,24] High reactant contact time[20], alongside high temperatures[21], favour the formation of the "hydrocarbon pool reaction centres" and drastically reduce the induction period. Also, depending on the type of zeolite used, the induction period can have different profiles under the same reaction conditions. Because of its small pores, H-SAPO-34 is able to limit the diffusion of hydrocarbons and accelerate the formation of the necessary "hydrocarbon pool" species, whereas in the case of H-ZSM-5, a catalyst with bigger pores than H-SAPO-34, this process is more prolonged even though H-ZSM-5 has a higher acidity.[21]

Ethene is reported to oligomerise and form the “HP reaction centres”, signalled by the increase in the conversion rate of methanol. Thus, the necessary step to occur in the induction period, and key component ending the induction period, is the formation of the first C-C bond compound, specifically ethene. A number of direct mechanisms have been proposed to account for the first C-C bond formation, which involved stable (dimethyl ether, methane, formaldehyde) or short life-time intermediate compounds (trimethyl oxonium, carbene).

C-C bond formation via formaldehyde or methane mechanism. Since formaldehyde and methane are present in the reaction mixture they were also considered to take part in the formation of reaction intermediates that could lead to the first C-C bond formation, in particular for the formation of ethanol, but the limited rate coefficient determined by a very small entropy that accompanies this reaction lead to their discounting this mechanism.[25]

Oxonium ylide mechanism. The oxonium ylide mechanism starts with the formation of trimethyl oxonium (TMO) via the reaction of dimethyl ether with a dimethyl oxonium ion (protonated dimethyl ether). Afterwards, the TMO is deprotonated by a basic site to form dimethyl oxonium methyl ylide (DOMY) that can undergo a Stevens rearrangement to form methylethyl ether or an intermolecular methylation, resulting in the formation of ethylmethyl oxonium ion (Fig. 1.2). The inability of the zeolite framework to deprotonate the TMO and stabilise the DOMY made this routes seem unfeasible.[26]

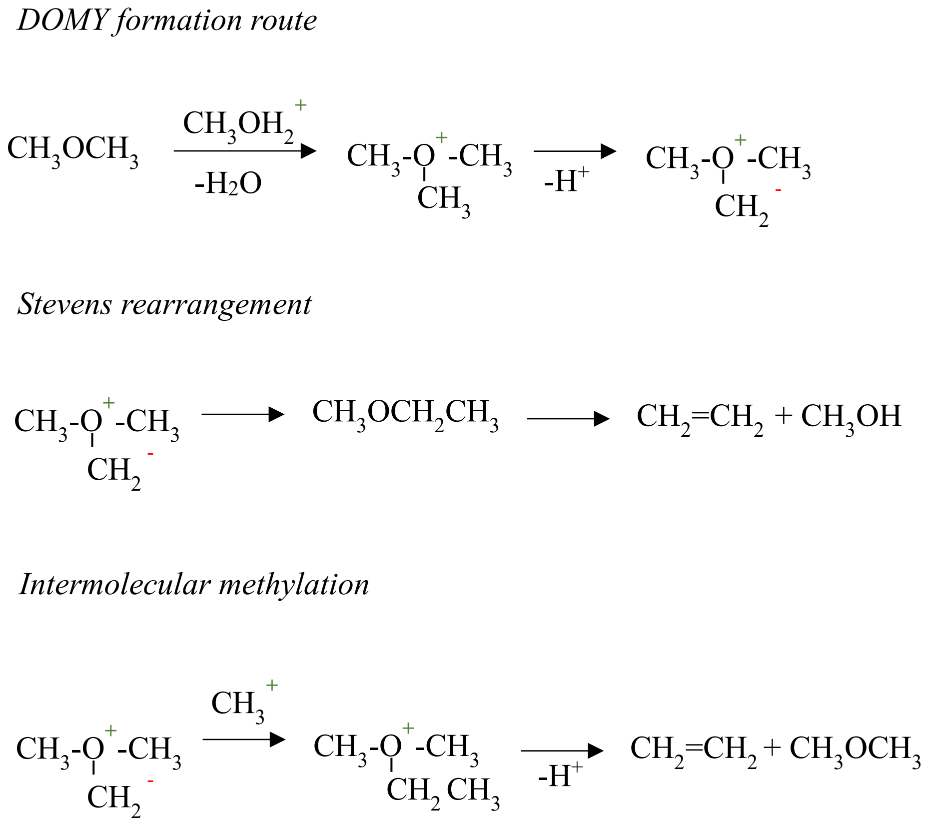

$$CH_3OCH_3 \xrightarrow[-H_2O]{CH_3OH_2^{+}} CH_3\text{-}\underset{\substack{|\\ CH_3}}{\overset{+}{O}}\text{-}CH_3 \xrightarrow[-H^{+}]{} CH_3\text{-}\underset{\substack{|\\ CH_2^{-}}}{\overset{+}{O}}\text{-}CH_3$$

$$CH_3\text{-}\underset{\substack{|\\ CH_2^{-}}}{\overset{+}{O}}\text{-}CH_3 \longrightarrow CH_3OCH_2CH_3 \longrightarrow CH_2{=}CH_2 + CH_3OH$$

$$CH_3\text{-}\underset{\substack{|\\ CH_2^{-}}}{\overset{+}{O}}\text{-}CH_3 \xrightarrow{CH_3^{+}} CH_3\text{-}\underset{\substack{|\\ CH_2\,CH_3}}{\overset{+}{O}}\text{-}CH_3 \xrightarrow[-H^{+}]{} CH_2{=}CH_2 + CH_3OCH_3$$

Figure 1.2. Illustration of oxonium ylide mechanism via TMO to ethene.

Carbene mechanism. An alternative to the previous route was the carbene mechanism, which involves the deprotonation of a zeolite bound methoxy to form a carbene (:CH_2) compound (Fig. 1.3), followed by either polymerisation to olefins or insertion in to a methanol or DME.[26] Experimental H/D exchange studies highlighted that C-D bond breaking can occur in H-ZSM-5[27] but not in H-SAPO-34[28]. Govind et al. conducted a theoretical study in a FER type zeolite, where they observed a stable carbene bound within the zeolite structure. However, the high activation energy of the methoxy deprotonation (78 kJ/mol) accompanied by a severe distortion of the framework ruled out the mechanism[29] proposing ethene formation via carbene.

$$\text{Z-OH} + CH_3OH \longrightarrow \text{Z-O-}CH_3 + H_2O$$

$$\text{Z-O-}CH_3 \xrightarrow[-H^+]{} \text{Z-O-}CH_2^- \longleftrightarrow \text{Z-O}\mathbf{:} + CH_2\mathbf{:}$$

Figure 1.3. Illustration of carbene mechanism via zeolite bound methoxy.

Free radical mechanism. The free radical mechanism introduced the idea of free methyl radicals formed from the interaction of DME with zeolite defects, such as silanol nests, that would dimerize to form the first C-C bond. [26] The presence of the free methyl radicals was argued by Hutchings *et al.* from the results of an experiment where the methanol feed contained NO, which acted as a radical scavenger, did not affect the activity or selectivity when using the ZSM-5 catalyst.[30] However, electron paramagnetic resonance studies reported signals of radical organic species (such as $\cdot H$, $:CH_2$, $:CH_2\text{-}CH_3$) after the methanol feed was stopped, but their actual involvement in reaction cycle has yet to be demonstrated.[26]

Concerted mechanism. Another proposed mechanism was the concerted mechanism where abstraction of a hydrogen from the methyl group of a methanol or DME molecule by a strong basic zeolite oxygen would allow a C-C bond formation with another methanol, DME, trimethyloxonium or zeolite bound methoxy group. [26] The calculated high energy barrier (over 200 kJ/mol) for the breaking of the covalent C-H bond by the available weak basic site made the previous route seem unlikely from an energetic standpoint.[25]

Although still debated, it is clear that the methoxide groups are an active component in the majority of the outlined mechanisms. As will be discussed next, further methoxides can take an active role not only in the induction period but are probably involved in every reaction step, up to the formation of larges olefins and aromatic hydrocarbons.[31,32,33,34,35]

1.2.2 Steady state reaction

1.2.2.1 Dual cycle mechanism

After the induction period, in which the "hydrocarbon pool" is formed of small olefins and different methylating agents (methanol, DME and methoxy), the conversion of methanol increases until it reaches a steady state.[36] The increase in methanol conversion rate to reach the steady state, is attributed to the formation of cyclic carbocationic species that act as a co-catalyst alongside the zeolite active site.[16,17,18] The "supramolecular" catalytic system composed of the organic carbocationic species and the inorganic zeolite framework was initially proposed by Haw *et al.* NMR and IR experiments shown that ethene or propene can form oligomeric species that subsequently convert into cyclic carboncations depending on the diffusion effects permitted by the zeolite framework. Specifically, the formation of poly-methyl benzene (PMB) requires a large space in the zeolite, such as a cross section or side pockets connected to narrow channels (H-SAPO-34, H-Beta)[37,38,39,40] to accumulate the large quantities of reactant ("ship-in-a-bottle" effect) and limit the diffusion to have enough time for the PMB to form. On the other hand, zeolites such as H-ZSM-5, H-SSZ-13[18,20] that connect supercages through wider pores, are more prone to form poly-methyl cyclopentenyl (PMCP).

Both these carbocationic species are part of the aromatic reaction cycle of the MTH process in the steady state, further expanded in Figure 1.4.

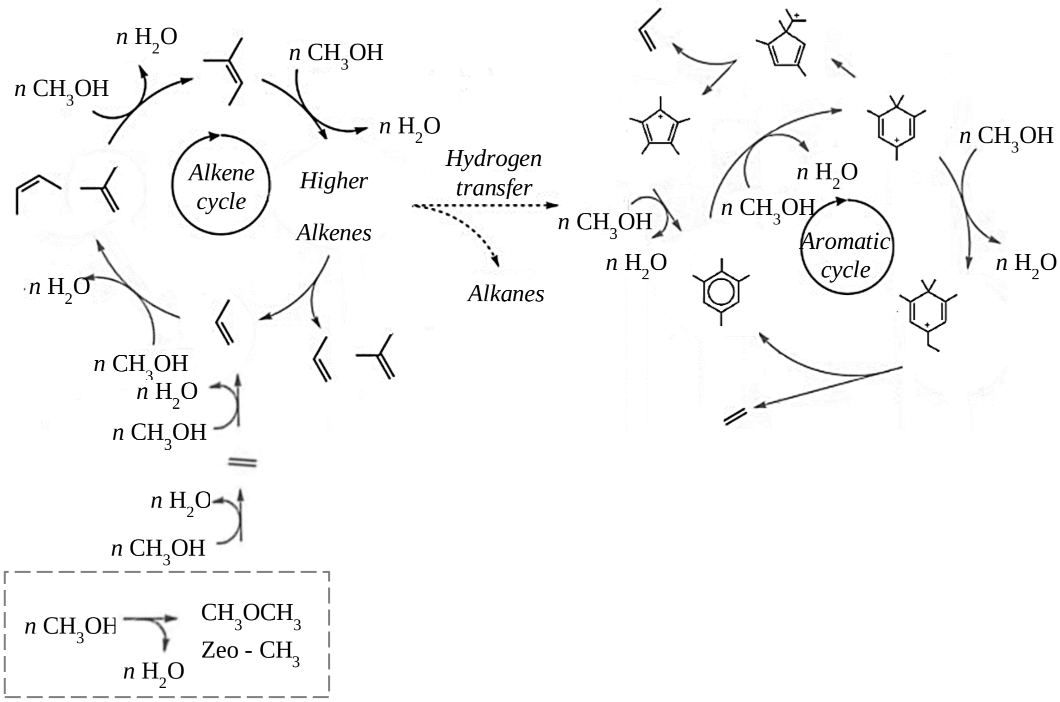

Figure 1.4. Illustration of the dual cycle mechanism of the MTH process, with initial stage highlighted in dashed box, alkene cycle (left), aromatic cycle (right), adapted with approval from Yarulina et al [45].

The carbocationic species can rearrange skeletally to one another and contribute to the formation of small olefins or polycyclic aromatics, depending on the working temperature. PMCP was found to decompose after increasing the temperature past 773 K, predominantly to toluene, followed by propene and traces of ethene.[18] At the same time, the carbocationic species are known have side-chain reactions that produce small olefins such as ethene or propene.[18,41,42] Depending on the number of methyl groups on the aromatic cycle, the selectivity can be directed towards a specific small olefin. Solid-state NMR studies reported that di and tri-MB cations would produce ethylcyclopentenyl intermediates, followed by the splitting off of ethene, while penta-MB would form propyl attached compounds, eventually generating propene.[43]

Apart from the aromatic cycle, small olefins will also take part in a separate reaction cycle, specifically the olefinic cycle, composed of a series of small olefins methylations, that will increase in size then to crack and form new small olefins.[44,36] Together, the aromatic and olefinic cycles form the dual-cycle mechanism that governs the steady state reaction.[45,46] Both are competitive with respect to the formation of ethene and propene. However, due to the energetics involved, the aromatic cycle is selective for ethene, whereas the olefinic, for propene.[41,42] In contrast, because the apparent free energies of the initial methylation steps and the lower overall free energy height involved, the alkene cycle dominates the overall process, which leads to propene forming in a higher yield than ethene.[41]

1.2.2.2 Influence of zeolite type on product selectivity

For the MTH process, it has been observed that the high reactivity of zeolite catalysts facilitates undesirable products. Side reactions can be suppressed by reducing the acidic character of the zeolite. In particular, weakening the strength or concentration of the acid sites,[47] coupled with "directing" the reactions towards the desired products by varying the pore size,[48] results in suppression of side reactions. Due to the molecular size of zeolite pores and large number of topologies available, the structure of the hydrocarbons can be "moulded" to a specific type.

A more comprehensive study at 400 ^{o}C and 80% methanol conversion highlighted that one dimensional, large pore zeolites such as ZSM-22 (TON 1D with 10-ring elliptical channel) and ZSM-23 (MTT 1D with 10-ring teardrop channel) are used to obtain C_{5+} aliphatics without any aromatic products formed. For aromatics, 10- or 12-member-ring zeolites, such as H/Na-ZSM-5 (MFI 3D 10-ring channel with cross-sections), mordenite (MOR 1D 12-ring channel with side pockets) and H-Beta (BEA 3D 12-ring channel with large cross-sections) are more appropriate. H-Mordenite was shown to give totally different product distributions than the previous zeolite catalytic systems. The product selectivity for these zeolites can be divided in ~60% C_1-C_5 aliphatics, 10-30% C_{6+} aliphatics and 10-20% aromatics.[49,50] Bjorgsen *et al.* noted that the acid strength can also determine the functional lifetime of the zeolite catalysts; on comparing the activity of two CHA topology-materials, the silicoaluminophosphate SAPO-34 and the zeolite SSZ-13, both with similar crystal size and acid site densities but different acid strength, the material with the highest acid strength (H-SSZ-13) yielded more coke and deactivated quicker.[46] Similar results were observed by Olsbye *et al.* for two zeolite catalysts with similar topologies but different acid site densities (i.e. different acidity); the more acidic ITQ-13 (ITH) and IM-5 (IMF) had higher conversion rates (for buthane/buthene and C_{6+} aliphatic/aromatic) but deactivated faster than the less acidic ZSM-22 (TON) and ZSM-23 (MTT).[49]

1.2.3 Deactivation stage

Several types of primary or secondary products may lead to catalyst deactivation, mainly because of their large size they can block the zeolite pores, which prevents the reactants from accessing the active sites or the intermediates necessary to methylate. Depending on the temperature regime, certain important intermediates, due to their large size, can hinder diffusion through the catalytic channels.[51,52] Ethyl, trimethyl-benzene and isopropyl, dimethyl-benzene were found to remain inert at medium temperatures (573 K) suspending the catalytic progress until the temperature was increased to 613 K which lead to the formation of alkenes.[52] By continuing to increase the temperature, after a series of methylation steps and skeletal rearrangements, the methylated monocyclic arenes would form other “coke species” such as poly-methylated naphthalene, anthracene that will block the zeolite pores.[53,54]

Catalyst deactivation is not only determined by the products obtained in the later stages, but also of those formed in the very beginning. Accurate control of the initial stages of the methanol conversion is needed since it can significantly impact the overall outcome of the MTH process. Disproportionation of methanol to formaldehyde influences the deactivation rate because formaldehyde would react with aromatic molecules resulting in the formation of polycondensed aromatics.[55] Also, the conversion of methanol to methane or CO_2 would be accounted as a carbon source loss, since both by-products are considered inert in common industrial conditions and cannot contribute to the formation of any desired hydrocarbons. Substituting methanol with DME was attempted in order to limit the production of the previously mentioned side-products. However, DME leads to a higher ratio of aromatic to aliphatic compounds and also a smaller water content that could be used to stabilise different intermediates and regenerate the necessary acid sites for methylation of the aromatic species, increasing the deactivation rate.[56]

1.3 Studies of the initial stages of the MTH process

Recent experimental investigations suggest that the framework methylation can occur spontaneously at room temperature in H-ZSM-5[28], which is a relatively low temperature, thus making it unclear what conditions control the methylation process. The low-temperature framework methylation, validated by diffuse reflectance FTIR (i.e. DRIFTS), quasielastic neutron scattering (QENS) and inelastic neutron scattering (INS) experiments[29,30], highlighted that when employing the right conditions, specifically, a high methanol loading (at least 3 methanol molecules per acid site) alongside a Si/Al ratio of 30, for two types of zeolite catalysts, the methylation occurs in H-ZSM-5 but not in H-Y[30]. Both experimental and theoretical[31] investigations showed that this reaction may occur faster when increasing the methanol loading, due to the formation of methanol clusters that could facilitate a spontaneous proton transfer that lowers the methylation activation barrier; however, there remains no explanation for how the spontaneous room-temperature methylation occurs.

Additional experimental studies report that an important aspect in methanol conversion is acid site configuration. At low temperatures and low reactant feed pressures, the dominant methanol conversion pathway for single or isolated acid sites is reported to be a direct formation of dimethyl ether[56] rather than framework methylation, which is active at high temperatures. In the case of vicinal or paired acid sites, experimental reports suggest that methanol undergoes a stepwise mechanism, to form dimethyl ether, via surface methoxy groups, at the same applied temperatures and pressures.[37]

Apart from the incremental growth of hydrocarbon chains, a methylated framework is believed to contribute to the initial formation of hydrocarbons. Wang *et al.* reported that a pure, methylated zeolite (CH_3-ZSM-5, CH_3-Y or CH_3-SAPO-34) could be heated (523 K) without reagents to produce paraffins, olefins and aromatics,[23,24] illustrating the crucial role of the methyl moiety and further highlighting the need to understand and fine tune the initial stages of the MTH process.

1.4 Hypothesis, Objectives and Structure

My study is based first on identifying the conditions that facilitate methanol conversion to methoxy and DME, and second to understand how the methoxy group may play an active role in the overall reaction. In order to isolate and precisely understand the potential events that can occur in the zeolite environment, state-of-the-art computational simulations have been used to consider static and dynamics aspects of these systems. Specifically, QM/MM static methods have been used to achieve a high degree of accuracy in evaluating the interactions involved and classical and enhanced Molecular Dynamics techniques to have a broader sample size of the possible reaction pathways that can occur in the zeolite pores.

Chapter 3 presents my study of the interactions between methanol and a zeolite during the initial stages of the MTH process that occur with various zeolite active sites, by using state-of-the-art modelling methods in the form of QM/MM static calculations. In Chapter 4, by means of classical and enhanced Molecular Dynamics techniques, I present my in-depth sampling of conformational space and associated analysis of the observables influencing methanol conversion to methoxy. The methyl migration outside the active site and reactivity to understand the initial stages of the first C-C bond formation, is further studied in Chapter 5. Finally, Chapter 6 considers an alternative pathway of methanol conversion to DME and the subsequent stability of DME on several acid sites in H-ZSM-5 and H-Y. A summary of the overall conclusions of my study and future work is presented in Chapter 7.

References

1 S. Marakatti, B. Halgeri and V. Shanbhag, *Cat Sci Tech*, 2014, **4**, 4065–4074.

2 C. Yokoyama and M. Misono, *Cat Tod*, 1994, **22**, 59–72.

3 C. Colella and W. S. Wise, *Micro Meso Mat*, 2014, **189**, 4–10.

4 J. Weitkamp, *Sol St Ion*, 2000, **131**, 175–188.

5 P. Wang, B. Shen and J. Gao, *Cat Tod*, 2007, **125**, 155–162.

6 M. Shamzhy, M. Opanasenko, P. Concepción and A. Martínez, *Chemi Soc Rev*, 2019, **48**, 1095–1149.

7 L. Qiu, V. Murashov and M. White, *Sol Stat Sci*, 2000, **2**, 841–846.

8 A. Corma and A.V. Orchillés, *Micro Meso Mat*, 2000, **35–36**, 21–30.

9 F.J. Keil, *Micro Meso Mat*, 1999, **29**, 49–66.

10 I. Dahl and S. Kolboe, *J Catal*, 1994, **149**, 458–464.

11 B. Smit and T. L. M. Maesen, *Nature*, 2008, **451**, 671–678.

12 J. Finn, P. E. H. Nielsen and P. M. D. Sørensen, *Biom Conv Bioref*, 2011, **1**, 85–90.

13 M. E. Dry, *Cat Tod*, 2002, **71**, 227–241.

14 C. D. Chang and A. J. Silvestri, *J Catal*, 1977, **47**, 249–259.

15 A. A. Avidan, *Stud Surf Sci Catal*, 1988, **36**, 307–323.

16 J. F. Haw and D. M. Marcus, *Top Catal*, 2005, **34**, 41–48.

17 J. Wang, Y. Wei, J. Li, S. Xu, W. Zhang, Y. He, J. Chen, M. Zhang, A. Zheng, F. Deng, X. Guo and Z. Liu, *Catal Sci Tech*, 2015, **6**, 89–97.

18 J. F. Haw, J. B. Nicholas, W. Song, F. Deng, Z. Wang, T. Xu and C. S. Heneghan, *JACS*, 2000, **122**, 4763–4775.

19 I. Kiricsi, H. Förster, G. Tasi and J. B. Nagy, *Chem Rev*, 1999, **99**, 2085–2114.

20 Y. Wei, D. Zhang, F. Chang and Z. Liu, *Catal Comm*, 2007, **8**, 2248–2252.

21 Y. Zhou, L. Qi, Y. Wei, C. Yuan, M. Zhang and Z. Liu, *Chinese J Catal*, 2016, **37**, 1496–1501.

22 K. De Wispelaere, C. S. Wondergem, B. Ensing, K. Hemelsoet, E. J. Meijer, B. M. Weckhuysen, V. Van Speybroeck and J. Ruiz-Martínez, *ACS Catal*, 2016, **6**, 1991–2002.

23 A. Hwang, M. Kumar, J. D. Rimer and A. Bhan, *J Catal*, 2017, **346**, 154–160.

24 Bailleul, Sven M.J. Rogge, Louis Vanduyfhuys and Veronique Van Speybroeck, *JACS*, 2019, **11**, 1–19.

25 K. Hemelsoet, J. V. der Mynsbrugge, K. D. Wispelaere, M. Waroquier and V. V. Speybroeck, *Chem Phys Chem*, 2013, **14**, 1526–1545.

26 M. Stöcker, *Micro Meso Mat*, 1999, **29**, 3–48.

27 I. B. Minova, S. K. Matam, A. Greenaway, C. R. A. Catlow, M. D. Frogley, G. Cinque, P. A. Wright and R. F. Howe, *ACS Catal.*, 2019, **9**, 6564–6570.

28 D. Marcus, K. McLachlan, M. Wildman, J. Ehresmann, P. Kletnieks and J. Haw, *Angew. Chem. Int. Ed.* 2006, **45**, 3133–3136.

29 N. Govind, J. Andzelm, K. Reindel and G. Fitzgerald, *Int J Molec Sci*, 2002, **3**, 423–434.

30 G. J. Hutchings, L. J. van Rensburg, W. Pickl and R. Hunter, *J. Chem. Soc., Faraday Trans. 1*, 1988, **84**, 1311–1328.

31 M. Stöcker, *Micro Meso Mat*, 1999, **29**, 3–48.

32 D. Lesthaeghe, V. Van Speybroeck, G. B. Marin and M. Waroquier, *Ind Eng Chem Res*, 2007, **46**, 8832–8838.

33 J. S. Martínez-Espín, K. De Wispelaere, T. V. W. Janssens, S. Svelle, K. P. Lillerud, P. Beato, V. Van Speybroeck and U. Olsbye, *ACS Catal*, 2017, **7**, 5773–5780.

34 W. Wang, A. Buchholz, M. Seiler and M. Hunger, *JACS*, 2003, **125**, 15260–15267.

35 W. Wang, M. Seiler and M. Hunger, *J Phys Chem B*, 2001, **105**, 12553–12558.
36 P. N. Plessow and F. Studt, *Catal Lett*, 2018, **148**, 1246–1253.
37 U. Olsbye, S. Svelle, K. P. Lillerud, Z. H. Wei, Y. Y. Chen, J. F. Li, J. G. Wang and W. B. Fan, *Chem. Soc. Rev.*, 2015, **44**, 7155–7176.
38 A. D. Chowdhury, K. Houben, G. T. Whiting, M. Mokhtar, A. M. Asiri, S. A. Al-Thabaiti, S. N. Basahel, M. Baldus and B. M. Weckhuysen, *Angew Chem Int*, 2018, 15840–15845.
39 W. Dai, C. Wang, M. Dyballa, G. Wu, N. Guan, L. Li, Z. Xie and M. Hunger, *ACS Catal.*, 2015, **5**, 317–326.
40 W. Song, J. B. Nicholas, A. Sassi and J. F. Haw, *Catal Let*, 2002, **81**, 49–53.
41 S. Wang, Y. Chen, Z. Wei, Z. Qin, H. Ma, M. Dong, J. Li, W. Fan and J. Wang, *J. Phys. Chem. C*, 2015, **119**, 28482–28498.
42 S. Xu, A. Zheng, Y. Wei, J. Chen, J. Li, Y. Chu, M. Zhang, Q. Wang, Y. Zhou, J. Wang, F. Deng and Z. Liu, *Angew Chem Int*, 2013, **52**, 11564–11568.
43 W. Song, H. Fu and J. F. Haw, *J. Am. Chem. Soc.*, 2001, **123**, 4749–4754.
44 R. M. Dessau and R. B. LaPierre, *J Catal*, 1982, **78**, 136–141.
45 I. Yarulina, A. D. Chowdhury, F. Meirer, B. M. Weckhuysen and J. Gascon, *Nat Catal*, 2018, **1**, 398–411.
46 U. Olsbye, S. Svelle, M. Bjrgen, P. Beato, T. V. W. Janssens, F. Joensen, S. Bordiga and K. P. Lillerud, *Angew Chem Int*, 2012, **51**, 5810–5831.
47 S. P. Greatbanks, I. H. Hillier, N. A. Burton and P. Sherwood, *J Chem Phys*, 1996, **105**, 3770–3776.
48 H. Fu, W. Song and J. F. Haw, *Catal Let*, 2001, **76**, 89–94.
49 S. Etemadi and U. Olsbye, *Master's Thesis "Catalytic investigations of zeolite based methanol to hydrocarbons catalysts",* 2015.
50 W. Wang, Y. Jiang and M. Hunger, *Cat Tod*, 2006, **113**, 102–114.
51 F. Bleken, M. Bjørgen, L. Palumbo, S. Bordiga, S. Svelle, K. Lillerud and U. Olsbye, *Top Catal*, 2009, **52**, 218–228.
52 H. Schulz, *Cat Tod*, 2010, **154**, 183–194.
53 B. P. C. Hereijgers, F. Bleken, M. H. Nilsen, S. Svelle, K.-P. Lillerud, M. Bjørgen, B. M. Weckhuysen and U. Olsbye, *J Catal*, 2009, **264**, 77–87.
54 D. Mores, J. Kornatowski, U. Olsbye and B. M. Weckhuysen, *Chem – A Euro J*, 2011, **17**, 2874–2884.
55 G. Henkelman and H. Jónsson, *J Chem Phys*, 2000, **113**, 9978–9985.
56 A. Zachariou, A. Hawkins, D. Lennon, S. F. Parker, Suwardiyanto, S. K. Matam, C. R. A. Catlow, P. Collier, A. Hameed, J. McGregor and R. F. Howe, *App Catal A: Gen*, 2019, **569**, 1–7.

Chapter 2. Computational Methods

This chapter serves as a preparatory chapter, introducing the methodology used throughout the rest of the thesis. The first section introduces an overview on the manner in which zeolite-adsorbate interactions can be modelled, using molecular mechanics and quantum mechanics. This is followed by an overview of several algorithms used to optimise the geometry of a model and find the minima and maxima on the potential energy surface. Finally, a description on the methods employed to simulate the dynamics of the system is also provided.

2.1 Embedded-cluster QM/MM calculations

The chemistry studied in this thesis involves a series of potential reactions that can occur spontaneously at room temperature or even 0 K, such as proton or hydride transfer and even methyl transfer, highly sensitive to the manner in which the electronic density is modelled. Large molecular systems can be modelled using molecular mechanics by employing a single classical expression (or force field) for the energy of a compound, with parameters obtained beforehand from fitting to experimental data or to ab initio calculations. However, these methods are less suitable, though, to model a wide variety of chemical reactions due to the amount of specific energy terms that would have to be included in order to simulate a broad range of interactions occurring between different types of atoms and molecules. Quantum mechanical methods treat electronic interactions explicitly, calculating approximate solutions to the Schrödinger equation of the system. In the same time, the use of pure *ab initio* methods is limited by the number of atoms that can be simulated. Previous studies[1,2] highlighted that small cluster models of the zeolite catalyst, containing only the active region without the overall framework lattice, would influence the stability of the zeolite Brønsted proton that, in turn, would affect the estimation of reaction and activation energies of chemical processes involving the acidic site. Thus, a QM/MM hybrid method is employed to have the main reactive region simulated with accurate quantum mechanical theory while the extended part being modelled by molecular mechanics, to limit the computational scale and precisely determine the energetic observables (such as reaction and activation energies, adsorption energies) characteristic of the studied reactions.

2.1.1 Molecular mechanics

2.1.1.1 Intra, Inter-atomic potentials[3]

Molecular Mechanics or force-field methods use classical models to calculate the energy of a molecule as a function of its conformation. The mechanical molecular model considers atoms as point entities that attract or repel each other, with the harmonic functions used to describe the ability of bonds to stretch, bend, and twist:

$$E_{tot} = E_{bond} + E_{angle} + E_{dihedral} + E_{elec} + E_{vdW} \tag{2.1}$$

where E_{tot} represents the total energy of the system, E_{bond} is the energy function for the stretching of a bond between two atoms, E_{angle} characterizes the energy for the bending of an angle within the molecule, $E_{dihedral}$ is the torsional energy for rotation around a bond, E_{elec} accounts for the energy contribution of electrostatic interactions, and E_{vdW} is the energy contribution from van der Waals interactions presented as follows:

$$E_{bond} = \frac{1}{2}\,\mathrm{k}_b(\mathrm{r}_{AB} - \mathrm{r}_0)^2 \tag{2.2}$$

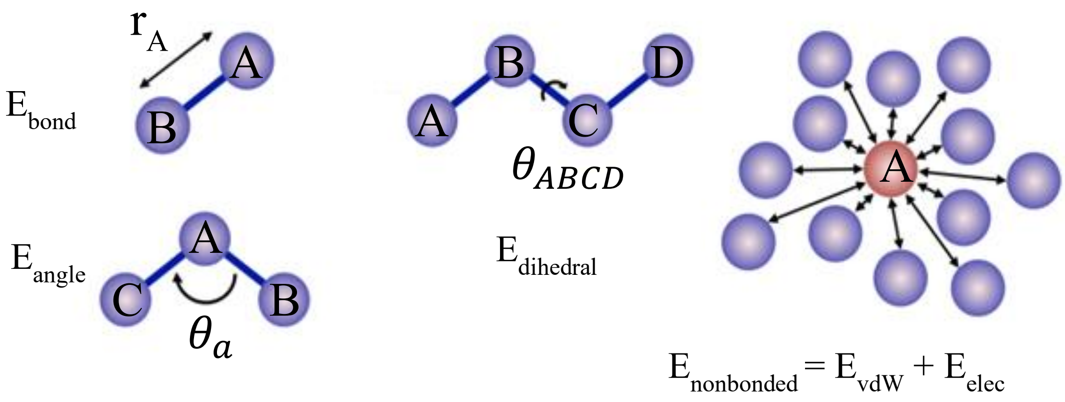

Figure 2.1. Schematic illustration of the terms in the force field, i.e. bond stretching (E_{bond}), bond-angle bending (E_{angle}), dihedral angle torsion ($E_{dihedral}$), and nonbonded as van der Waals (E_{vdW}) and electrostatic (E_{elec}) interactions. Adapted with permission from Riniker et al[4].

The bond potential equation in our work, is a harmonic potential based on Hooke's law. The k_b parameter controls the stiffness of the bond spring, while r_0 defines its equilibrium length. Unique k and r_0 parameters are assigned to each pair of bonded atoms based on their types (e.g. C-C, C-H, O-C, etc.). This equation estimates the energy associated with vibration around the equilibrium bond length. In order to describe more complex motions (such as dissociation) a more detailed expression based on Morse potential can be used:

$$E_{bond} = \mathrm{E}_0 \{1 - \exp(-\mathrm{a}(\mathrm{r}_{AB} - \mathrm{r}_0))\}^2 \tag{2.3}$$

where E_0 is the depth of the potential energy minimum and $a = \omega\sqrt{\frac{\mu}{2E_0}}$, where μ is the reduced mass and ω is the frequency of the bond vibration (related to the force constant k of the bond by $\omega = \sqrt{\frac{k}{\mu}}$). r_0 is the equilibrium distance of the bond. This potential can describe the bond over a wider range of distances than the harmonic function but the exponential term in the Morse potential adds computational expense.

The bending energy equation in our work, is also based on Hooke's law:

$$E_{angle} = \frac{1}{2}\, \mathrm{k}_a\, (\theta_a - \theta_0)^2 \qquad (2.4)$$

The $\mathrm{k_a}$ parameter controls the stiffness of the θ_a angle spring between specified atoms A, B and C while θ_0 defines its equilibrium angle. The force constants are smaller than those associated with bonding potentials as less energy is needed to deform an angle.

The dihedral angle energy potential in molecular mechanics is primarily used to correct the remaining energy terms rather than to represent a physical process. The dihedral angle (ϕ) is the angle between the *A-B* and *C-D* bonds in a bond *A-B-C-D*. The torsional energy function must be periodic, in that if the bond is rotated by 360° the energy must return to the same value.

The dihedral forces in this thesis are represented using the cosine potential form shown below:

$$E_{dihedral} = \mathrm{k}_d\, [1 + \cos(m\phi_{ABCD} - \phi_0)] \qquad (2.5)$$

where the constant k_d represents the size of the rotational barrier around the *C-D* bond and represents the divisions of periodicity throughout 360° (m=1 is periodic by 360° m=2 is periodic by 180°, m=3 is periodic by 120° etc).

The van der Waals interaction between non bonded atoms/molecules is introduced by the following the Lennard-Jones 12-6 potential:

$$E_{vdW} = 4\epsilon\left[\left(\frac{\mathrm{r}_0}{r_{AB}}\right)^{12} - \left(\frac{\mathrm{r}_0}{r_{AB}}\right)^{6}\right] \qquad (2.6)$$

The $\mathrm{E_{vdW}}$ potential increases greatly when the distance between two atoms (r_{AB}) is smaller than the sum of their radii (vdW radii), thus accounting for the repulsive effect. However, when the two atoms are far apart, the dispersion interaction vanishes as r^{-6}, determining an attractive effect (as displayed in Figure 2.2). The two atoms fluctuate around an equilibrium distance r_0 with a minimum interaction energy ϵ.

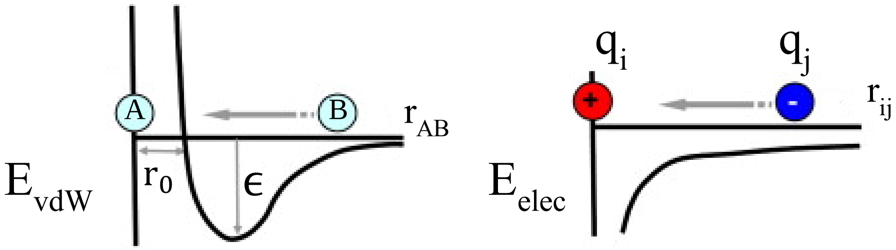

Figure 2.2. Schematic illustration of variation of E_{vdW} with distance between atoms A, B (r_{AB}) - left, and of E_{elec} with distance between charge q_i and q_j (r_{ij}) - right, adapted with permission from Notman et al[5].

In order to account for the atomic charges (q_i, q_j) that interact electrostatically by Coulombic forces, we insert the E_{elec} term:

$$E_{elec} = \sum_{i=1}^{N_i} \sum_{j=1}^{N_j} \frac{q_i q_j}{4\pi\varepsilon_0 r_{ij}} \tag{2.7}$$

The electrostatic energy is a function of the charge on the non-bonded atoms, their interatomic distance (r_{ij}), and a molecular dielectric expression (ε_0) that accounts for the attenuation of electrostatic interaction by the environment, varying as illustrated in Figure 2.2.

2.1.2 Electronic methods[3,6,7]

Electronic structure methods are employed to have a more accurate description of our chemical environment, especially to model reactions involving bond breaking/formation and charge distributions. The core of these techniques is based on quantum mechanics that can either be *ab initio* (if the method is not referenced to experimental data) or semi-empirical (if the method involves parameters from experimental data).

Any system in a pure state can be described by a wave-function, $\Psi(r,t)$, where t is a parameter representing time and r represents the coordinates of the system, with the probability of finding the system in particular state given by $|\Psi^2|$.

The energy and properties of the system are determined by solving Schrödinger equation:

$$\hat{H}\Psi(r,t) = \frac{h}{2\pi}\frac{\partial\Psi(r,t)}{\partial t} \tag{2.8}$$

where Ĥ is the Hamiltonian operator:

$$\hat{H} = -\frac{\hbar}{2m}\left(\frac{\partial^2}{\partial x^2}+\frac{\partial^2}{\partial y^2}+\frac{\partial^2}{\partial z^2}\right)+V(r,t) \tag{2.9}$$

with the first term representing the kinetic energy operator and second term describing the potential energy operator.

For systems where the external potential energy operator is time independent, the Schrödinger equation becomes:

$$\hat{H}\Psi = E\Psi \tag{2.10}$$

with E being the energy of the system, and the respective eigenvalues of the Hamiltonian.

The Hamiltonian of the system can be split into contributions as follows:

$$\hat{H} = T^{elec}(r) + T^{nuc}(R) + V^{nuc-elec}(R,r) + V^{elec}(r) + V^{nuc}(R) \tag{2.11}$$

where the kinetic (T) and potential (V) terms are functions of the electronic coordinates (r) and nuclear coordinates (R).

Since the nuclei are considerably heavier than electrons, their velocities are much smaller than electron velocities which renders the $T^{nuc}(R)$ operator to be negligible (Born-Oppenheimer approximation) and results in only the solution for the electron wavefunction necessary to be solved.

Based on the “Linear Combination of Atomic Orbitals” approximation, we can also assume that the total wavefunction is a total of smaller functions, known as basis functions.

$$\Psi = \sum_i c_i\phi_i \tag{2.12}$$

ϕ_i is the atomic orbitals and c_i being the weight of each of their contributions to the molecular orbital (Ψ).

In order to reduce the number of calculations performed on the electron-electron repulsion term V^{elec}, the Hartree-Fock method can be employed to solve the many electron problem. The electron-electron interactions can be reduced to the interaction of each electron with the spherical average of the potential of all other electrons and the nucleus, expressed as a charge centred on the nucleus (central-field approximation). The one-electron hamiltonian can be rewritten as the Fock operator $\hat{f}(i)$:

$$\hat{f}(i) = \underbrace{-\frac{1}{2}\nabla_i^2 - \sum_{A=1}^{M}}_{\hat{h}(i)} \frac{Z_A}{r_{iA}} + \underbrace{\sum_{j}^{N} \hat{J}_j(i) - \hat{K}_j(i)}_{Hartree - Fock\ potential, \upsilon_{HF}} \tag{2.13}$$

The $\hat{h}(i)$ part collects the terms dependent only on electron i in the field of M nuclei (indexed by A and atomic number Z), while the HF potential υ_{HF} involves the electron-electron interactions in an average potential. $\hat{J}_j(i)$ and $\hat{K}_j(i)$ are the Coulomb and exchange operators respectively. Taken together with the basis expansion, the HF equations can be written in matrix form, known as the Roothan-Hall equations:

$$FC = \varepsilon SC \tag{2.14}$$

where F is the Fock matrix, S is an overlap matrix, ε is the matrix containing the orbitals energies and C contains all basis set coefficients. The aim of these equations is to be solved iteratively until ε is minimised.

2.1.2.1 Density Functional Theorem[3,6,7]

An additional approximation to determining the energy of the system and include electron correlation effects is made in the form of DFT.

Instead of using the wavefunction to model our chemical environment we reduce our system to the electron density, specifically "non-interacting" electrons under the influence of an "external" potential (that takes the role of the electron-nuclei interaction). The use of the electron density is sufficient to model our systems of interest, since the integral of the density defines the number of electrons, the cusps in the density define the position of the nuclei and the heights of the cusps define the corresponding nuclear charges.

In this formulation, the electron density is expressed as a linear combination of basis functions:

$$\rho(r) = \sum_i |\phi_i(\boldsymbol{r})|^2 \tag{2.15}$$

where the sum is over all the occupied Kohn–Sham (KS) orbitals; $\boldsymbol{r}$ is known once these orbitals have been computed.

The exact ground-state electronic energy E of an $\boldsymbol{n}$ electron system can be written as:

$$E = T_{elec} + V_{elec-nuc} + J_{elec-elec} + E_{XC} \tag{2.16}$$

where T_{elec} represents the kinetic energy of the "non-interacting" KS electrons, $V_{elec-nuc}$ electron-nuclei interaction (or other "external" potential), $J_{elec-elec}$ the electron cloud self-interaction. E_{XC} is an energy contribution that relates to the correlation of motions in electrons, either from taking the same position ("Coulombic hole") or same spin ("Fermi hole"), alongside the kinetic energy of the real electrons.

Of the four terms, E_{XC} is the one we do not know how to obtain exactly. Although the Hohenberg–Kohn theorem tells us that E and therefore E_{XC} must be functionals of the electron density, we do not know the latter's exact analytical form and so are forced to use approximate expressions for it.

2.1.2.1.1 Exchange Correlation functionals for DFT[3,6,7]

A simple system of electrons in a molecule was represented by the local density approximation in which we have a homogeneous electron gas cloud containing nuclear charges distributed uniformly.

In the Local Density Approximation (LDA), the exchange–correlation functional is:

$$E_{XC}^{LDA} = \int \rho(r)\varepsilon_{XC}(\rho)d^3r \qquad (2.17)$$

where $\varepsilon_{XC}(\rho)$ is the exchange–correlation energy per electron in a homogeneous electron gas of constant density ρ.

This oversimplification led to the development of the Non-Local Density Approximation (NLDA) methods, which takes into account the inhomogeneous partition of electrons reflected by the gradient of the electron density.

A number of different gradient-corrected functionals were proposed; in general, the LDA with gradient corrections, which is called the generalized gradient approximation (GGA). One of the most known and widely used GGA functionals, with a simple form is the PBE functional:

$$E_{XC}^{PBE} = \int \rho(r)\varepsilon_{XC}\big(\rho, \nabla(\rho)\big)d^3r \, F_{XC}(\rho(r), \nabla(r)) \qquad (2.18)$$

with $F(\rho(r), \nabla(r))$ representing the reduced density gradient.

Compared to LDA, PBE was reported to more accurate results for atomisation energies and energy barriers involving small molecules.

In this thesis, Chapter 4, we used the revised version of PBE (revPBE), which has improved calculated values of molecular atomisation energies[8]. Since F_X dominates F_{XC}, here we describe the spin-polarized enhancement factor F_X only:

$$F_X^{revPBE} = 1 + k - \frac{k}{1 + \frac{\mu}{k}s^2} \qquad (2.19)$$

with $\mu = 0.21951$, $k = 1.245$ and s - a dimensionless function of the density gradient which serves as a measure of ‘‘nonlocality’’.

While GGA's are very successful, they still tend to over-estimate the binding and transition state energies. This issue is overcome, at a higher computational cost than GGA's, by employing hybrid functionals. Semi-empirical functionals, such as the B97 functional, have been developed that combine the Becke 1997 (B97) GGA exchange-correlation expansion - GGA (E_{GGA}^{97}) with a fraction (c_N) of exactly computed orbital exchange (E_x^{HF}):

$$E_{XC}^{97-3} = \sum_{i}^{15} c_i f_i(\rho, \nabla\rho) + c_{16} E_x^{HF} \qquad (2.20)$$

In this thesis, we used the B97-3[9] functional with the form:

$$E_{XC}^{97} = E_{GGA}^{97} + c_P E_x^{HF} \qquad (2.21)$$

With c_i and f_i representing expansion parameters and functions, respectively, of the electron density (ρ).

This functional has been parametrised to fit data comprising of several thermodynamic parameters (such as reaction barriers, ionisation and proton affinities)[9] crucial for our analysis in sections Chapters 3, 5 and 6.

2.1.2.1.2 Dispersion corrections of DFT[10]

Standard DFT has some shortcomings when describing long range London dispersion interactions and self-interactions. Dispersion interactions are particularly important in our simulations, as we will detail later on, since they can contribute to the stabilisation of large molecular structures such as methanol clusters and are necessary to give more accurate descriptions of our chemical environment.

The correction used in this thesis is based on the semi-empirical, atom pairwise sum over C_6R^{-6}, DFT-D3 method. In this scheme, the total energy of the system (E_{tot}) is equal to the sum of the Kohn-Sham energy E_{KS} and the dispersion correction E_{disp}:

$$E_{tot} = E_{KS} + E_{disp} \tag{2.22}$$

The dispersion energy is a sum of two and three-body energies:

$$E_{disp} = E_{(2)} + E_{(3)} \tag{2.23}$$

with the most important contribution coming from the two-body term:

$$E_{(2)} = \sum_{AB} \sum_{n=6,8,10,\ldots} s_n \frac{C_n^{AB}}{r_{AB}^n} f_{d,n}(r_{AB}) \tag{2.24}$$

Where r_{AB}^n represents the internuclear distance between atoms A, B (as represented in Figure 2.3), s_n is a scaling factor, C_n^{AB} denotes the averaged isotropic nth-order dispersion coefficient orders n=6,8,10,... for atom pair AB, both ensuring the correct asymptotic behaviour of the potential, while the higher order terms influence its shape at shorter distances, $f_{d,n}(r_{AB})$ is a damping function used to avoid near-singularities at small r_{AB} and double counting effects of electron correlation at medium distances.

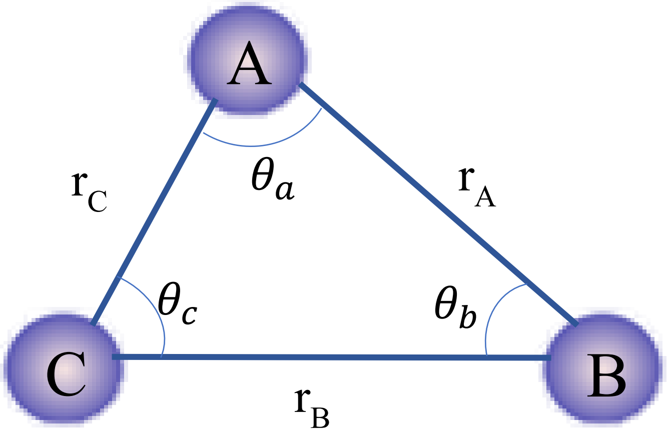

Figure 2.3. Atoms representation highlighting the geometrical features used in the damping functions of the second and third body terms of the dispersion correction.

The three-body term is represented by the sum over all atom triples ABC in the system as follows:

$$E_{(3)} = \sum_{ABC} f_{d,(3)}(\bar{r}_{ABC})\, E^{ABC} \tag{2.25}$$

with $f_{d,(3)}$ and $\bar{r}_{ABC}$ is $\sqrt[3]{r_{AB} r_{BC} r_{CA}}$ (geometrically averaged radii of atoms A, B, C displayed in Figure 2.3) are used as damping functions, and

$$E^{ABC} = \frac{C_9^{ABC}(3\, cos\theta_a\, cos\theta_b\, cos\theta_c + 1)}{(r_{AB} r_{BC} r_{CA})^3} \tag{2.26}$$

where θ_a, θ_b , and θ_c are the internal angles of the triangle formed by r_{AB}, r_{BC} and r_{CA} (as displayed in Figure 2.3), and C_9^{ABC} is a triple-dipole constant.

2.1.2.2 Møller–Plesset perturbation theory[3]

Whilst DFT is generally a good approximation, we would like to test methods that explicitly include correlation effects. The configuration interaction method is a rigorous way to add correlation to the Hartree-Fock results, the method is computationally very demanding because of the large number of excited Slater determinants that need - at least in principle - to be included.

The Hamiltonian is partitioned as

$$\widehat{H_{el}} \;=\; \widehat{H_0} + \lambda \widehat{H'} \tag{2.27}$$

where H_0 (Hartree-Fock Hamiltonian) is the sum of fock operators $\hat{f}(i)$, and $\widehat{H'}$ is the perturbation of the reference (H_0) multiplied by a variable real parameter λ.

The Schrödinger equation becomes

$$(\widehat{H_0} + \lambda \widehat{H'})\Psi = W\Psi \tag{2.28}$$

as a Taylor expansion in powers λ

$$\Psi = \lambda^0\Psi_0 + \lambda^1\Psi_1 + \lambda^2\Psi_2 + \cdots \qquad (2.29)$$

$$W = \lambda^0 W_0 + \lambda^1 W_1 + \lambda^2 W_2 + \cdots \qquad (2.30)$$

Calculating the second-order energy correction we arrive at

$$W_2 = E(MP2) = \sum_{i<j}^{occ}\sum_{a<b}^{virt} \frac{\langle \Phi_0|\hat{H}'|\Phi_{ij}^{ab}\rangle\langle \Phi_{ij}^{ab}|\hat{H}'|\Phi_0\rangle}{E_0 - E_{ij}^{ab}} \qquad (2.31)$$

where Φ_{ij}^{ab} denotes a Slater determinant with electrons i and j excited to the virtual orbitals a and b. This energy is typically referred to as the MP2 energy and is the most common energy to compute.

2.1.2.3 Basis sets[3]

A basis set is a set of functions used to describe the shape of the orbitals in an atom. Molecular orbitals and entire wave functions are created by taking linear combinations of basis-functions as follows:

$$\Phi(r) = f(x, y, z)\exp(-\alpha r^n) \qquad (2.32)$$

For n=1 we have Slater Type Orbitals (STOs) and for n=2, Gaussian Type Orbitals (GTOs) (Figure 2.4), where $f(x, y, z)$ is a polynomial function of the form $x^a y^b z^c$ with x, y, z representing the cartesian coordinates and a, b, c the order, r is the distance from the nucleus and α determines the radial extent of the orbital. If the polynomial function $f(x, y, z)$ is zeroth order (sum of a, b, and c is zero) we form an s-type orbital, and if it is a first order (sum of a, b, and c is one) we describe a p type orbital, etc.

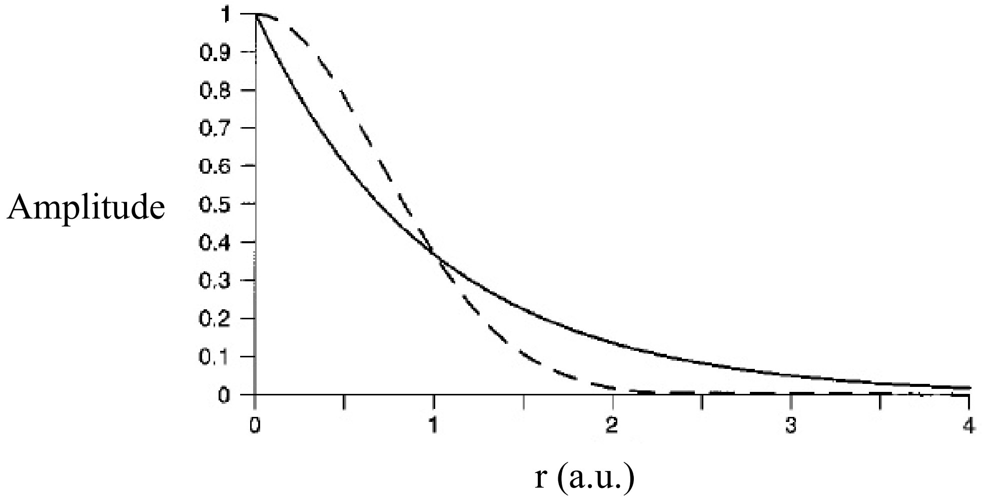

Figure 2.4. Comparison of STO (solid line) and GTO (dashed line) s type basis functions performance[11].

In order to improve the accuracy of the orbital representation, a polarisation function (P) can be added to account for the distortion of the orbital in the presence of other nuclei that particularly take part in the bond formation with the atom of interest.

Since the external charge density is more responsible for the reactivity of an atom, the orbitals corresponding to the valence electrons are represented by more than one basis set. If the valence basis set is split into two functions we have a DZVP basis set (such as the one developed by Goedecker *et al.*[12]), employed in Chapter 4 or into three functions we have a TZVP basis set (such as the one formulated by Ahlrichs and Taylor[13]) used in this thesis, Chapters 3, 5 and 6.

2.1.2.4 Plane wave basis sets[14]

As previously mentioned, when solving Kohn-Sham equations, the wavefunctions are expanded in a basis set. However, when dealing with periodic systems, each wavefunction can be written as a product of a lattice-periodic part $u(\boldsymbol{k}, \boldsymbol{r} + \boldsymbol{R}) = u(\boldsymbol{k}, \boldsymbol{r})$, with $\boldsymbol{r}$ and $\boldsymbol{R}$ lattice vectors of real space, and $\boldsymbol{k}$ - lattice vector of reciprocal space, a plane wave $e^{i\boldsymbol{kr}}$, with i - imaginary unit:

$$\phi(\boldsymbol{k}, \boldsymbol{r}) = e^{i\boldsymbol{kr}} \cdot u(\boldsymbol{k}, \boldsymbol{r}) \tag{2.33}$$

The lattice-periodic part can be expanded in plane waves whose wave vectors $\boldsymbol{G}$ are reciprocal lattice vectors:

$$u(\boldsymbol{k}, \boldsymbol{r}) = \sum_{\boldsymbol{G}} c_{\boldsymbol{k},\boldsymbol{G}} e^{i\boldsymbol{kr}} \tag{2.34}$$

leading to:

$$\phi(\boldsymbol{k}, \boldsymbol{r}) = \sum_{\boldsymbol{G}} c_{\boldsymbol{k},\boldsymbol{G}} e^{i(\boldsymbol{k}+\boldsymbol{G})\boldsymbol{r}} \tag{2.35}$$

There are strong oscillations in the wavefunctions near the nucleus, thus requiring a very large number of plane waves to describe these oscillations. In order to reduce the complexity of the plane waves, the potential inside some core radius is replaced by a series of smooth auxiliary wavefunctions, representing a pseudopotential describing the nucleus and the core electrons.

In order to do so, we apply linear transformation $\hat{\mathcal{T}}$ which takes us from an auxiliary smooth wave function $\tilde{\phi}_n$ to the true all electron Kohn-Sham single particle wave function ϕ_n:

$$|\phi_n\rangle = \hat{\mathcal{T}} |\tilde{\phi}_n\rangle \tag{2.36}$$

Since the true wave functions are already smooth at a certain minimum distance from the core, $\hat{\mathcal{T}}$ should only modify the wave function close to the nuclei. We thus define:

$$\hat{\mathcal{T}} = 1 + \sum_{a=1}^{N} \widehat{\mathcal{T}^{a}} \qquad (2.37)$$

where a is an atom index, and the atom-centred transformation, $\widehat{\mathcal{T}^{a}}$, has no effect outside a certain atom-specific augmentation region $|r - R_a| < r_a$. The cut-off radii, r_a should be chosen such that there is no overlap between the waves of other atoms.

Inside the augmentation region, the true and auxiliary wavefunctions are expanded in corresponding partial waves $\langle\varphi_i^a|$ and $\langle\tilde{\varphi}_i^a|$. Then is can be shown that the atomic centred transformation can written as

$$\widehat{\mathcal{T}^{a}} = 1 + \sum_{i} (\langle\varphi_i^a| - \langle\tilde{\varphi}_i^a|)\langle\tilde{p}_i^a| \qquad (2.38)$$

where $\langle\tilde{p}_i^a|$ are projector functions. To summarize, the full wavefunction can be written as

$$\phi_n(\boldsymbol{r}) = \tilde{\phi}_n(\boldsymbol{r}) + \sum_{a}\sum_{i} (\varphi_n^a(\boldsymbol{r}) - \tilde{\varphi}_n^2(\boldsymbol{r}))\langle\tilde{p}_i^a|\tilde{\phi}_n\rangle \qquad (2.39)$$

2.1.2.5 Periodic boundary conditions[15]

Periodic boundary conditions are employed when working with large systems in order to reduce computational cost by replicating a certain unit cell in all three dimensions, thus providing a periodic lattice.

The positions occupied by the atoms in the set unit cell described by vector r, would be converted into mirror images in the adjacent boxes defined by vector:

$$\vec{r}^{image} = \vec{r} + l\vec{a} + m\vec{b} + n\vec{c} \qquad (2.40)$$

where l, m, n are integer numbers, and $\vec{a}, \vec{b}, \vec{c}$ are the vectors corresponding to the edges of the a, b, c box.

In order to attain continuity between the computed unit cell and replicas, the minimum image convention is employed such that the particles movement is not restricted to the simulated box. This is implemented by “allowing” the molecules to interact with the nearest image particle, within a certain cut-off radius. The cut-off radius cannot be greater than half the width of the unit cell in order to ensure that the atom interacts with only one image of any given particle.

2.1.3 QM/MM[16]

The QM/MM technique combines electronic methods with molecular mechanics in order to counter the weaknesses of the individual QM, MM techniques and focus on their advantages. In order to achieve a proper chemical accuracy ensured by QM methods, at a reasonable computational cost, QM/MM simulations allow us to model the most reactive part with QM techniques and the rest of the surrounding environment, in our case a large bulk lattice, with MM (Figure 2.5).

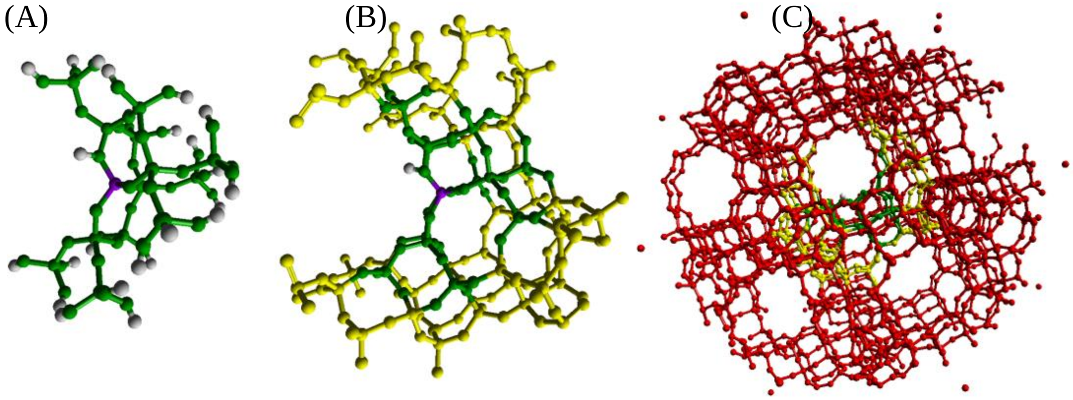

Figure 2.5. Example of the QM/MM setup in H-Y with regions highlighted being: (A) QM region (green); (B) relaxed MM region (yellow); (C) fixed MM region (red).

In our work, the QM/MM calculations are setup starting from an optimised unit cell of the zeolite lattice. A spherically shaped cluster is generated based on a cut-off radius, centred in the active site of interest. This also acts as the centre for the QM region. The spherical QM part centred on the Aluminium atom contains the Brønsted acid site and other surrounding atoms are included in order to properly describe the physico-chemical properties and achieve a proper charge distribution representation. The QM region is continued by two concentric MM regions. The first MM region has the atoms free to move in order to replicate the flexibility of the framework. The second MM region has the atoms fixed to reproduce the stability of the bulk zeolite. The construction of the embedded cluster model if finished by adding the external point charges to simulate the Madelung field of the extended system within the cluster inner core.

This approach helps us to study processes such as sorbate adsorption and catalytic conversion with electronic structure methods, avoiding the problems encountered in periodic systems such as periodic images of the defect/sorbate interacting with each other.

The QM/MM energy we have used is based on an “additive” approach, where the total QM/MM energy is the sum of the QM, MM and coupling terms:

$$E = E(Inner, \mathrm{QM}) + E(Outer, \mathrm{MM}) + E(Couple, \mathrm{QM/MM}) \qquad (2.41)$$

where, *E(Inner,* QM*)*, *E(Outer,* MM*)* represent the energies of the inner and outer regions, post optimisation, *E(Couple,* QM/MM*)* accounts for all interactions between the two regions. In this thesis, we use the electrostatic embedding method, where the QM region

$$E^{QM} = \langle \Psi | \hat{H}^{QM} + \hat{V}^{MM} | \Psi \rangle + E_{nuc}^{QM} + E_{nuc}^{QM-MM} \qquad (2.42)$$

is polarised by the electrostatic potential coming from the MM region and the external point charges, with the QM energy expressed as follows:

Here, $\hat{V}^{MM}$ is the external potential from the surrounding regions, E_{nuc}^{QM} is the Coulombic interaction between nuclei of the QM region, and E_{nuc}^{QM-MM} is the Coulombic interaction between QM and MM nuclei.

The QM atoms are represented by atomic centred basis sets as described in section 2.1.2.3. The MM atoms have the atomic charges determined by a bond increment-charge model.

The atomic charge is assigned from a sum of terms, one for each bond formed. When partitioning the QM, MM regions (Scheme 2.1), the QM region is constructed so that it has oxygen atoms instead of silicon at the edge. This is done to limit the number of charges necessary to be neutralised. The QM boundary atoms (O_{QM}) are saturated by hydrogen atoms placed along the corresponding QM/MM bonds at an appropriate O-H distance. The counterpart MM atoms (Si_{MM}) are removed from the MM model and the remaining charge transferred (δ) to the adjacent MM sites (O_{MM}). In order to correct the unrealistic electrostatic interactions coming from the additional charge distribution (δ*), a pair of point charges (·-·) are placed at the MM sites to neutralise the opposing dipole.

a) QM_{region} - O_{QM} - $[Si_{MM}]^{\delta}$ - O_{MM} - MM_{region}

b) QM_{region} - O_{QM} - H_{QM} $[O_{MM}]^{\delta*}$ ·-· MM_{region}

Scheme 2.1. QM/MM junction of zeolite a) pre-electrostatic partitioning; b) post-electrostatic partitioning. Additional neutralising bonds on Si atom were excluded for simplicity.

The boundary electrostatics at the periphery of the MM region are described by external point charges, in the form of interatomic potentials. They are commonly fitted by determining the difference between the electrostatic potential of our embedded cluster model and that of a periodic model (zero reference potential) to account for the long-range Madelung potential coming from an infinitely extending lattice.

2.1.4 Energy minimisation methods[7]

In order to generate a stable configuration of our simulated molecular system, several energy minimisation algorithms can be used to find a set of geometric coordinates equivalent to a local minimum on the potential energy surface.

The common descriptors employed are the first (gradient) and second order (∇^2) derivative of the energy with respect to position **r**, where $\frac{\partial E}{\partial r_i} = 0$ and $\frac{\partial^2 E}{\partial r_i^2} > 0$ correspond to a local minima.

One example that uses the gradient of the energy is the steepest descent method. This is an iterative method that takes the initial coordinate x_i and displaces it by a certain step length λ in a certain direction $\boldsymbol{d}_i$, chosen based on the energy gradient, as follows:

$$x_{i+1} = x_i + \lambda \boldsymbol{d}_i \qquad (2.43)$$

If the energy gradient decreases, we continue the displacement until it increases, which is when the direction of the displacement is changed orthogonally to the previous line. As the line sampling is orthogonal to the previous search, it may undo the progress made by that point.

To prevent this loss of progress, the nonlinear conjugate gradient method can by employed, which performs the search along a line which is “conjugate” to prior search directions, thus preventing the sampling to occur along the previous lines. The first step is equivalent to a steepest descent step, but subsequent searches are performed along a line formed as a mixture of the current negative gradient ($\nabla_i E$) and the previous search direction ($\boldsymbol{d}_{i-1}$).

$$\boldsymbol{d}_i = -\nabla_i E + \beta_i \boldsymbol{d}_{i-1} \qquad (2.44)$$

$\boldsymbol{d}_i$ is the search direction defined as the sum between the negative gradient (*i.e.* force) and the previous search direction and β_i represented by the Polak-Ribbiere equation:

$$\beta_i^{PR} = \frac{\boldsymbol{d}_i^T (\boldsymbol{d}_i - \boldsymbol{d}_{i-1})}{\boldsymbol{d}_{i-1}^T - \boldsymbol{d}_{i-1}} \qquad (2.45)$$

where $\boldsymbol{d}_i^T$ and $\boldsymbol{d}_{i-1}^T$ is the transposed matrix of the direction vector $\boldsymbol{d}$ at the set position.

In this thesis, we used the second order derivatives employed in the L-BFGS method, based on the Newton-Raphson equation of the gradient function centred in current point x_i, Taylor expanded to the second order leading to:

$$f(x_{i+1}) = f(x_i) + f'(x_i)(x_{i+1} - x_i) + \frac{1}{2}f''(x_i)(x_{i+1} - x_i)^2 \qquad (2.46)$$

$$f'(x_i) + f''(x_i)(x_{i+1} - x_i) = 0 \qquad (2.47)$$

To find a minimum we require the second order approximation to be zero

leading to

$$(x_{i+1} - x_i) = -\boldsymbol{H}^{-1}\nabla E \qquad (2.48)$$

where $\boldsymbol{H}^{-1}$ is an inverse Hessian matrix (a matrix of the second derivatives of the energy with respect to coordinates, giving the curvature of the potential energy surface) and ∇E is the gradient.

In order to find x, which is the minimum on the potential energy landscape, we need to determine the Hessian. Calculating the second order derivatives to form the Hessian matrix can be very computationally demanding, which is why an updating scheme is employed. In this case, the gradients of the current and previous step are used to calculate the Hessian. This leads to a good approximation to the exact Hessian in the direction defined by the two points at which the gradient determination was done. The use of approximate Hessians (pseudo-NR method) requires more steps to reach convergence, but the computational cost would be lower than using exact Hessians (NR method). This thesis uses the limited BFGS version[17,18,19,20] which restricts which restricts the stored history of previous steps to M steps and N atoms, giving a memory requirement of N × M values, increasing processing speed; employed in Chapters 3, 5 and 6.

2.1.5 Transition state calculations

2.1.5.1 Nudged elastic band method for finding minimum energy paths [21,22]

In addition to stable structures, determining the transition state between certain steady states is also a crucial aspect in characterising our chemical environment.

The NEB method provides a way to finding a minimum energy pathway (MEP) and saddle points connecting two local minima. This is done by creating several images (or `states', denoted by [$\boldsymbol{R}_0$, $\boldsymbol{R}_1$, …, $\boldsymbol{R}_N$]) of the system that are connected together with springs, to trace out the reaction pathway.

In the NEB method, the total force ($\boldsymbol{F}_{im}$) acting on an image (indexed by im) is the sum of the spring force along the local tangent ($\boldsymbol{F}_{im}^{S}|_{\parallel}$) and the true force perpendicular to the local tangent:

$$\boldsymbol{F}_{im} = \boldsymbol{F}_{im}^{S}|_{\parallel} - \nabla E(\boldsymbol{R}_{im})|_{\perp} \tag{2.49}$$

where the true force is given by

$$\nabla E(\boldsymbol{R}_{im})|_{\perp} = \nabla E(\boldsymbol{R}_{im}) - \nabla E(\boldsymbol{R}_{im}) \cdot \hat{\mathrm{r}}_{im} \tag{2.50}$$

Here, E is the energy of the system, a function of all the atomic coordinates, and $\hat{\mathrm{r}}_{im}$ is the normalized local tangent at image im. The spring force is:

$$\boldsymbol{F}_{im}^{S}|_{\parallel} = k(|\boldsymbol{R}_{im+1} - \boldsymbol{R}_{im}| - |\boldsymbol{R}_{im} - \boldsymbol{R}_{i-1}|)\hat{\mathrm{r}}_{i} \tag{2.51}$$

where k is the spring constant. The $N-1$ intermediate images are adjusted by an optimization algorithm according to the force in eq (2.49). The images converge on the MEP with equal spacing if the spring constant is the same for all the springs.

Typically, the resolution of the MEP near the saddle point is poor and the estimate of the activation energy obtained from the interpolation is subject to large uncertainty. In order to refine the MEP described, subsequent fine tuning can be done by employing a climbing image algorithm, such as the dimer method, as highlighted in Figure 2.6.

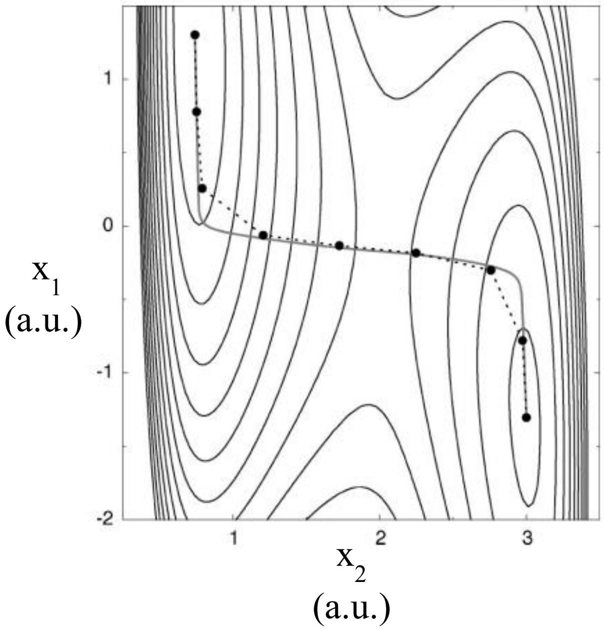

Figure 2.6. Illustration of energy path described by the NEB (dashed line) and dimer (solid line) methods on a projected energy surface of x_1, x_2 *geometric coordinates. Adapted from Henkelman et al.*[21]

2.1.5.2 Dimer method[23,24]

The dimer method is a saddle point algorithm based on the first derivatives of the energies and forces of the reaction path endpoints.

The first step involves taking the coordinates of the initial ($\boldsymbol{R}_1$) and final ($\boldsymbol{R}_2$) states and creating an image at the midpoint line described by the (dimer) axis connecting $\boldsymbol{R}_1$ and $\boldsymbol{R}_2$ on the potential energy surface as follows:

$$\boldsymbol{R}_2 = \boldsymbol{R} - \Delta R\widehat{\boldsymbol{N}} \tag{2.52}$$

$$\boldsymbol{R}_1 = \boldsymbol{R} + \Delta R\widehat{\boldsymbol{N}} \tag{2.53}$$

with ΔR representing the distance between the midpoint and endpoints and $\widehat{\boldsymbol{N}}$ a unit vector along the dimer axis. By employing the finite difference approximation, we find that the curvature (C) of the potential energy surface along the dimer axis is:

$$C = \frac{(\boldsymbol{F}_2 - \boldsymbol{F}_1)\cdot\widehat{\boldsymbol{N}}}{2\Delta R} = \frac{E - 2E_0}{(\Delta R)^2} \tag{2.54}$$

with $\boldsymbol{F}_1, \boldsymbol{F}_2$ representing the forces acting on the two endpoint images and E_0 the energy of the midpoint image, from which we have

$$E_0 = \frac{E}{2} + \frac{\Delta R}{4}(\boldsymbol{F}_2 - \boldsymbol{F}_1)\cdot\widehat{\boldsymbol{N}} \tag{2.55}$$

In order to find the minimum energy path, the dimer axis is rotated into the lowest curvature mode on the potential energy surface and translated for a certain step length towards a saddle point. In this thesis, the direction for both the rotation and translation displacements is determined based on the conjugate gradient method discussed in the Energy minimisation section.

2.2 Periodic Ab Initio Molecular Dynamics

2.2.1 Molecular dynamics[15]

In order to understand more about the evolution of a system from one state to another, we also employed Molecular Dynamics (MD) techniques. MD is a method that uses Newtonian equations of motion to simulate the changes in interaction over time of a set of molecules and sample more possible events that can occur in our environment.

The trajectory is given by the equation of motion:

$$F_i = m_i a_i = m_i \frac{dv_i}{dt} = m_i \frac{d^2 x_i}{dt^2} \qquad (2.56)$$

where F_i is the force exerted on particle i, of mass m_i, with a_i as the acceleration of particle i, v_i the velocity, and coordinate x_i. Knowing that the force can also be expressed as the negative gradient (∇_i) of the potential energy (V), expressed as $F_i = -\nabla_i V$, we can relate the derivative of the potential energy to the changes in position as a function of time:

$$-\frac{dV}{dv_i} = m_i a_i = m_i \frac{dv_i}{dt} = m_i \frac{d^2 x_i}{dt^2} \qquad (2.57)$$

Taking the simple case where the acceleration is constant, $a = \frac{dv}{dt} = \frac{d^2x}{dt^2}$, we obtain an expression for the velocity and coordinate after integration as follows:

$$v = \mathrm{a}t + v_0 \qquad (2.58)$$

$$x = vt + x_0 \qquad (2.59)$$

Since the acceleration is given as the derivative of the potential energy with respect to the position,

$$a = -\frac{1}{m}\frac{dV}{dx} \qquad (2.60)$$

Combining these equations, we obtain the following relation which gives the value of x at time t as a function of the acceleration, a, the initial position, x_0, and the initial velocity, v_0.

$$x = \frac{1}{2}\mathrm{a}t^2 + v_0 t + x_0 \qquad (2.61)$$

we can calculate a trajectory by just using the initial positions of the atoms, an initial distribution of velocities and the acceleration, which is determined by the gradient of the potential energy function.

2.2.1.1 Integration Algorithms[15]

Numerous numerical algorithms have been developed to solve the equations of motion by time integration, all of which assume that the positions, velocities and accelerations can be approximated by a Taylor series expansion:

$$r(t - \delta t) = r(t) - v(t)\delta t + \frac{1}{2}a(t)\delta t^2 \qquad (2.62)$$

$$r(t + \delta t) = r(t) + v(t)\delta t + \frac{1}{2}a(t)\delta t^2 + \cdots \qquad (2.63)$$

To derive the Verlet algorithm which helps us simplify the previous equations, we can write:

$$v(t + \delta t) = v(t) + a(t)\delta t + \frac{1}{2}b(t)\delta t^2 + \cdots \qquad (2.64)$$

$$a(t + \delta t) = a(t) + b(t)\delta t + \cdots \qquad (2.65)$$

Summing these two equations, we obtain:

$$r(t + \delta t) = 2r(t) - r(t - \delta t) + a(t)\delta t^2 \qquad (2.66)$$

$$r(t + \delta t) = r(t) + v(t)\delta t + \frac{1}{2}a(t)\delta t^2 \qquad (2.67)$$

Thus, we can calculate new positions at time $t + \delta t$ by using positions and accelerations at time t and the positions from time $t - \delta t$, without explicit velocities. The timestep (time between evaluating the potentials) should be smaller than the fastest vibration associated with the system, to avoid energy drift associated with larger time steps which can destabilise the system. The advantages of the Verlet algorithm are that it is straightforward and the storage requirements are modest.

2.2.1.2 Microcanonical ensembles

Molecular dynamics is usually performed under the microcanonical (NVE) ensemble. Here, the number of particles, volume and energy are constant. It may be desirable to maintain a constant temperature during the simulation, in which case the canonical (NVT) ensemble is used, where the number of particles, volume and temperature are kept constant or the (NPT) with the pressure kept constant instead of the volume. Several thermostats and barostats are available to ensure the proper temperature and prressure of the chemical environment such as the Berendsen thermostats and barostats. However, the chain Nose Hoover thermostat and Martyna, Tuckerman, Tobias, and Klein barostat[25,26] has been shown to ensure a comprehensive molecular dynamics sampling of the phase space due to the stochastic fluctuation of the temperature.

2.2.1.2.1 NVT ensemble[27,28]

In the case of the NVT ensemble, the temperature (T) of a system is related to the time average of the velocity (v_i) of i particles in the system with n degrees of freedom. the initial velocities given from a Maxwell-Boltzmann distribution at the desired temperature:

$$\langle\sum_{i}^{n}\frac{1}{2}m_i v_i^2\rangle = \frac{3}{2}nk_B T \qquad (2.67)$$

In order to maintain the temperature of the environment at a specific value we need to introduce a thermostat. The most common and suitable example for our simulations would be the Nose-Hoover thermostat. This allows us to sample different areas of phase space while maintaining the appropriate energy distribution of the particles. The Nose-Hoover thermostat involves coupling the real modelled system to a fictitious heat bath (described by s degrees of freedom and mass Q). The potential energy associated with s is $(3N + 1)k_B T\ ln(s)$, where $3N + 1$ is the total number of degrees of freedom and kinetic energy related to s is $Q(ds/dt)^2/2$.

This newly formed extended system (model + bath) would produce a canonical ensemble in the real modelled system due to heat exchange between the bath and real system, with the corresponding lagrangian and hamiltonian of the extended system in virtual time $t'(t \cdot s)$ being:

$$H_{NVT} = \sum_{i=1}^{N}\frac{\boldsymbol{p}_i'^2}{2M_i\, s^2} + V_{(r_i)} + \frac{p_s^2}{2Q} + gk_B T\ ln(s) \qquad (2.68)$$

with the respective equations of motion:

$$\frac{\partial \boldsymbol{r}_i}{\partial t} = s\frac{\partial \boldsymbol{r}_i}{\partial t'} = \frac{\boldsymbol{p}_i'}{M_i s} = \frac{\boldsymbol{p}_i}{M_i} \tag{2.69}$$

$$\frac{\partial \boldsymbol{p}_i}{\partial t} = s\frac{\partial}{\partial t'}\left(\frac{\boldsymbol{p}_i'}{s}\right) = \frac{\partial \boldsymbol{p}_i'}{\partial t'} - \frac{1}{s}\frac{\partial s}{\partial t'}\boldsymbol{p}_i' = -\nabla V - \frac{1}{s}\frac{\partial s}{\partial t}\boldsymbol{p}_i \tag{2.70}$$

$$\frac{\partial s}{\partial t} = s\frac{\partial s}{\partial t'} = s\frac{\boldsymbol{p}_s}{Q} \tag{2.71}$$

$$\frac{\partial \boldsymbol{p}_s}{\partial t} = s\frac{\partial \boldsymbol{p}_s}{\partial t'} = \sum_{i=1}^{N}\frac{\boldsymbol{p}_i^2}{M_i} - gk_BT \tag{2.72}$$

2.2.1.2.2 NPT ensemble[25,26]

We consider a similar system with N_f degrees of freedom, contained in a box of variable volume V characterised by a unit cell tensor $\boldsymbol{h}$ and a cell momentum tensor p_g, which is further subjected to an external stress tensor σ. The cell momentum tensor p_g is associated with the unit cell tensor h and drives the fluctuations of this unit cell tensor as follows with the barostat mass W:

$$\dot{\boldsymbol{h}} = \frac{\boldsymbol{p}_g\boldsymbol{h}}{W} \tag{2.73}$$

$$W = \left(N_f + 9\right)\frac{k_BT}{2}\left(\frac{\tau_p}{2\pi}\right)^2 \tag{2.74}$$

in which τ_p represents the barostat relaxation time.

The equations of motion of the cell momentum tensor p_g depend on both the kinetic energy E_{kin} and the difference between the stress tensor σ and the instantaneous pressure tensor P_i as follows:

$$\dot{p_g} = (P_i - \sigma)V + \frac{2E_{kin}}{N_f} - \frac{p_\xi}{Q}\boldsymbol{p}_g \tag{2.75}$$

with the last term stemming from the temperature control via a Nose - Hoover thermostat with mass Q and thermostat momentum p_ξ.

2.2.2 Metadynamics[29,30]

Although MD simulations have their set of applications, there is also a great interest in determining high energy demanding steps ("rare events"), that normally occur after a high amount of simulation time. To limit the high computational cost demanded by classical Ab Initio MD techniques, enhanced MD methods in the form of Metadynamic methods are employed to accelerate the sampling process (Figure 2.7).

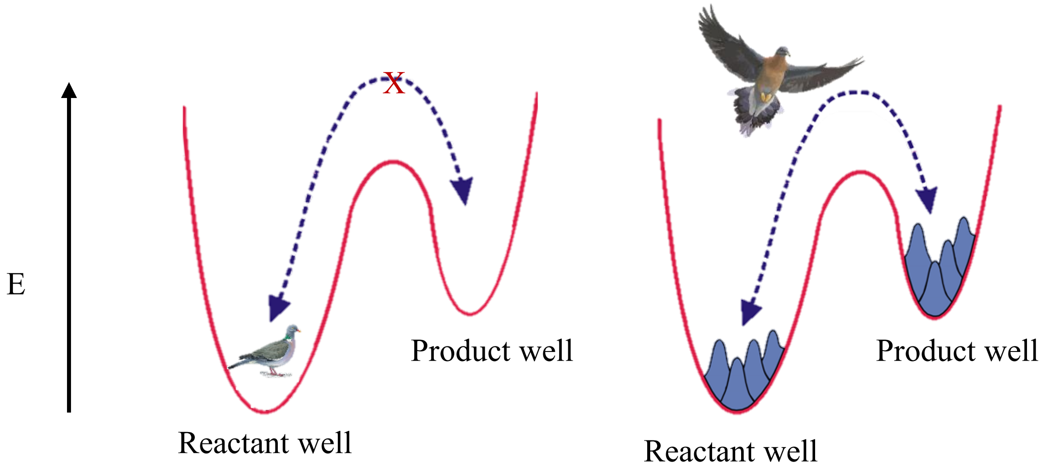

Figure 2.7. Comparison between MD (left) and MTD (right) sampling performances of reactant and product energy states.

Metadynamics uses an applied time-dependent repulsive bias potential (V) to a set of collective coordinates (s), also known as collective variable (CVs) or reaction coordinates that ensure a proper description of the reaction path we are interested in analysing, allowing us to visit different areas of configurational space and estimate the free energy surface (FES).

$$V(\vec{s}, t \rightarrow \infty) = -F(\vec{s}) + C \tag{2.76}$$

The collective coordinates (*i.e.* descriptors) employed can be bond distances, dihedral angles, coordination numbers, or any other geometric parameter depending on the reaction process that we want to analyse and on the condition that they allow us to discriminate between reactant and product state. The trajectory along the phase space is described by the following Lagrangian:

$$\mathcal{L} = \mathcal{L}_0 + \sum_{\alpha} \frac{1}{2} M_{\alpha} \dot{s}_{\alpha}^2 - \sum_{\alpha} \frac{1}{2} k_{\alpha} [S_{\alpha}(R) - s_{\alpha}]^2 + V(t, \boldsymbol{s}) \tag{2.77}$$

where $\mathcal{L}_0$ is the casual Lagrangian that drives the electronic and ionic dynamics, which, the second term is the (fictitious) kinetic energy of s_{α}, the third term is a sum of harmonic potentials that restrain the value of $S_{\alpha}(R)$ (instantaneous values of the collective variables) close to the corresponding dynamic collective variable s_{α}, and $V(t, \boldsymbol{s})$ is a history-dependent potential. The mass M_{α} and the coupling constant k_{α} determine how fast s_{α} evolves in time with respect to the degrees of freedom.

The dynamics of the s_{α} is driven by these forces $f_{\alpha} = k_{\alpha}[S_{\alpha}(R) - s_{\alpha}]$ plus the forces coming from the history-dependent term. The potential is built as a sum of Gaussian hills deposited along the trajectory in the CVs space:

$$V(\vec{s}, t) = \sum_{k\Gamma < t} W(k\Gamma) exp\left(-\sum_{i=1}^{d} \frac{(s_i - s_i(q(k\Gamma)))^2}{2\sigma_i^2} \right) \tag{2.78}$$

where Γ is the Gaussian deposition stride, σ_i the width of the Gaussian for the ith CV, and $W(k\Gamma)$ the height of the Gaussian.

This method was successfully applied to determine different physical(diffusion coefficient) and chemical parameters (activation barriers) and was also employed in Chapter 4.

2.2.3 Equilibration and production run

The first stage of a molecular dynamics simulation is the equilibration phase, the purpose of which is to bring the system to equilibrium from the starting equilibrium at the target temperature.

The system is considered to be equilibrated once a set of properties either remain stable or fluctuate around the set mean value. Specifically, the temperature, pressure, kinetic and potential energies fluctuate due to the type of thermostat and barostat we employed, whereas the total energy and volume reach a certain constant value.

The system is then permitted to evolve, in the NVT canonical ensemble, for both MD and Metadynamics simulation in which the adsorption energy and FES are determined, respectively, alongside different geometrical parameters.

2.3 Resources

The static QM/MM simulations were done with the Chemshell software[31], used as interface for the QM softwares GAMESS-UK[32] or NWChem[33] and MM software DL-POLY[34] for the studies in Chapters 3, 5 and 6. The *Ab Initio* Molecular Dynamics and Metadynamics calculations were done with the CP2K software[35] for the study in Chapter 4.

References

1 J. D. Gale, C. R. a. Catlow and J. R. Carruthers, *Chem Phys Let*, 1993, **216**, 155–161.
2 C. R. A. Catlow, B. Smit and R. A. van Santen, *Computer modelling of microporous materials*, 2004.
3 Lujien Piela, *Ideas of Quantum Chemistry - 2nd Edition*, 2nd edn., 2013.
4 S. Riniker, *J. Chem. Inf. Model.*, 2018, **58**, 565–578.
5 R. Notman and J. Anwar, *Adv Dr Del Revs*, 2013, **65**, 237–250.
6 R. F. Peter Atkins, *Molecular Quantum Mechanics*, Oxford University Press, 5th edn., 2010.
7 F. Jensen, *Introduction to computational chemistry*, John Wiley & Sons, Chichester, England ; Hoboken, NJ, 2nd ed., 2007.
8 K. Yang, J. Zheng, Y. Zhao and D. G. Truhlar, *J Chem Phys*, 2010, **132**, 164117.
9 T. W. Keal and D. J. Tozer, *J Chem Phys*, 2005, **123**, 121103.
10 S. Grimme, J. Antony, S. Ehrlich and H. Krieg, *J Chem Phys*, 2010, **132**, 154104–154104.
11 A. H. C. Horn, *J. Chem. Inf. Comput. Sci.*, 2003, **43**, 1720–1720.
12 S. Goedecker and M. Teter, *Phys Rev B - Cond Mat Mat Phys*, 1996, **54**, 1703–1710.
13 P. R. T. Reinhart Ahlrichs, 1981, 315–324.
14 G. K. H. Madsen, P. Blaha, K. Schwarz, E. Sjöstedt and L. Nordström, *Phys. Rev. B*, 2001, **64**, 195134.
15 D. Frenkel and B. Smit, *Understanding Molecular Simulation: From Algorithms to Applications*, 2002.
16 P. Sherwood, A. H. De Vries, S. J. Collins, S. P. Greatbanks, N. A. Burton, M. A. Vincent and I. H. Hillier, *Faraday Discuss*, 1997, **106**, 79–92.
17 C. G. Broyden, *Math Comp*, 1970, **24**, 365–365.
18 R. Fletcher, *Comp J*, 1970, **13**, 317–322.
19 D. Goldfarb, *Math Comp*, 1970, **24**, 23–23.
20 D. F. Shanno, *Math Comp*, 1970, **24**, 647–647.
21 G. Henkelman and H. Jónsson, *J Chem Phys*, 2000, **113**, 9978–9985.
22 G. Henkelman, B. P. Uberuaga and H. Jónsson, *J Chem Phys*, 2000, **113**, 9901–9904.
23 A. Heyden, A. T. Bell and F. J. Keil, *J Chem Phys*, 2005, **123**, 224101.
24 G. Henkelman and H. Jónsson, *J Chem Phys*, 1999, **111**, 7010–7022.
25 S. M. J. Rogge, L. Vanduyfhuys, A. Ghysels, M. Waroquier, T. Verstraelen, G. Maurin and V. Van Speybroeck, *J. Chem. Theory Comput.*, 2015, **11**, 5583–5597.
26 G. J. Martyna, D. J. Tobias and M. L. Klein, *J. Chem. Phys.*, 1994, **101**, 4177–4189.
27 S. Nosé, *J. Chem. Phys.*, 1984, **81**, 511–519.
28 W. G. Hoover, *Phys. Rev. A*, 1985, **31**, 1695–1697.
29 A. Barducci, M. Bonomi and M. Parrinello, *Wiley Inter Rev: Comp Molec Sci*, 2011, **1**, 826–843.
30 M. Iannuzzi, A. Laio and M. Parrinello, *Phys. Rev. Lett.*, 2003, **90**, 238302.
31 S. Metz, J. Kästner, A. A. Sokol, T. W. Keal and P. Sherwood, *Wiley Inter Rev: Comp Molec Sci*, 2014, **4**, 101–110.

32 M. F. Guest, I. J. Bush, H. J. Van Dam, P. Sherwood, J. M. H. Thomas, J. H. Van Lenthe, R. W. Havenith and J. Kendrick, *Molec Phys*, 2005, **103**, 719–747.
33 M. Valiev, E. J. Bylaska, N. Govind, K. Kowalski, T. P. Straatsma, H. J. J. Van Dam, D. Wang, J. Nieplocha, E. Apra, T. L. Windus and W. A. De Jong, *Comp Phys Com*, 2010, **181**, 1477–1489.
34 W. Smith, C. W. Yong and P. M. Rodger, *Molecular Simulation*, 2002, **28**, 37–41.
35 J. VandeVondele, M. Krack, F. Mohamed, M. Parrinello, T. Chassaing and J. Hutter, *Comp Phys Com*, 2005, **167**, 103–128.

Chapter 3.

Computational QM/MM investigation of the adsorption of MTH active species in H-Y and H-ZSM-5

In this chapter, we use hybrid quantum- and molecular-mechanical (QM/MM) embedded-cluster simulations to develop our understanding of the interaction between methanol and the zeolite catalysts H-ZSM-5, and for comparison, the larger pore H-Y. Energies and structures, calculated using hybrid-level density functional theory (hybrid-DFT) and higher-level correlated methods, are compared with previous experimental and computational results. We show that hydrogen-bonds between methanol adsorbates, formed through polarizable O-H bonds, substantially influence the adsorption energetics, structural parameters and vibrational frequencies. Our observations are extended by considering polar solvent molecules in the environment, with the presence of both water or methanol around the adsorption site leading to barrier-less transfer of the zeolite proton to an adsorbed methanol, which will significantly influence the reactivity of the adsorbed methanol.

3.1. Introduction

As noted in Chapter 1, due to its applications in petrochemical industry and catalytic value the study on the methanol activation in zeolite is of great importance.[1,2] The nature of the catalytic active site, and the surrounding topology, as detailed in Section 1.2.2.2, has been shown to influence significantly the overall reaction, with zeolites like H-ZSM-5 remaining the catalyst of choice in current industrial applications.[3]

Recently, O'Malley *et al.* presented strong evidence of a low barrier for formation of methoxy groups on the zeolite framework; quasi- and inelastic neutron scattering data shows that framework methoxylation occurs spontaneously in flow conditions at room temperature in H-ZSM-5 (MFI) but not H-Y (FAU), both with Si/Al ratios of 30.[4] The authors suggested that the steam pre-treatment of H-Y, necessary to dealuminate the framework so as to raise heat stability and Brønsted acidity, results in framework silanol and hydroxyl defects that diminish the methoxylation capability compared to H-ZSM-5. Computational simulations also suggest that the adsorption and methoxylation energetics could be related to the formation of stabilizing hydrogen bonds between the sorbate and framework.[5] However, several IR spectroscopy studies indicate apparently contradictory results that the methanol is either protonated to form the methyloxonium ion,[6] reducing the energy barrier towards methoxylation,[7] or that the methanol is simply physisorbed. [8,9] Indeed a recent IR study of Matam *et al*[10] suggests that both methoxylated and H-bonded species may be present.

To progress understanding of the methanol/zeolite interaction, we present here a computational investigation that aims to clarify the first stages of the MTH process involving adsorption of methanol at the Brønsted acid sites. We highlight the significant role of solvation on CH_3OH adsorption energetics by investigating the co-adsorption of a range of molecules present from either the reaction feed or as reaction by-products.

3.2. Methodology

3.2.1 Models

To perform the QM/MM calculations, we first create spherical embedded-cluster models of H-ZSM-5 and H-Y from the experimental unit cells of siliceous MFI [11] and FAU [12], respectively, centred on a Si tetrahedral (T-)site of interest. Whilst FAU has only one symmetry inequivalent T-site, MFI has 12 symmetry inequivalent T-sites. Thus, in order to sample different reaction environments in H-ZSM-5, we have considered 3 different T-sites as focal points for models of this material: the straight channel [T1 (M7)], the sinusoidal channel [T4 (Z6)] and the more open channel intersections [T12 (I2)], as displayed in Figure 1. After creating our embedded-cluster model as discussed in Section 2.1.3, we replaced the central Si atom in each model with an Al atom, and have added a charge compensating H on a neighbouring oxygen atom in a manner that facilitates reaction modelling, specifically where the H atom is most accessible, noting that the energy differences between H locations are typically small[5,13,14].

The QM region, which is the chemically active part of our model, includes atoms up to the fifth nearest neighbour (the third oxygen atom) from the central T-site. In their entirety, the total number of atoms in each cluster model is: 1653 for H-Y, with 62 QM atoms and 130 inner MM atoms; 2165 for H-ZSM-5 [T12 (I2)], with 74 QM atoms and 197 inner MM atoms; 2180 for H-ZSM-5 [T1 (M7)], with 67 QM atoms and 207 inner MM atoms; and 2155 for H-ZSM-5 [T4 (Z6)], with 72 QM atoms and 184 inner MM atoms.

Throughout, the QM energy has been calculated using hybrid-DFT with the Becke97-3 exchange-correlation (XC) functional[15], explained in Section 2.1.2.1.1, as provided in the GAMESS-UK code.[16] Additional energy calculations, where highlighted, were performed post-geometry optimisation using the dispersion corrected B97-D functional[17], detailed in Section 2.1.2.1.2, and higher-level Møller-Plesset perturbation theory (MP2), functionality of NWChem[18], explained in Section 2.1.2.2. This approach was chosen as this work is the foundation for a more extensive investigation of the thermochemical process of methoxylation, for which B97-3 is an appropriate exchange-correlation functional; comparison of B97-3 and B97-D geometry optimised models showed negligible geometric differences between structures (~0.01 Å) and minimal changes to derived energetic results (5 kJ/mol), as presented in Table 3.1.

Table 3.1. Comparison of energies between the single point (SP) and optimised (Opt) models with B97-D and geometric parameters between the B97-3 optimised models used for the SP calculation and the B97-D optimised models, as defined in the main manuscript. d(Hzeo-OMeOH) is the distance between the zeolite acid site and the oxygen of the methanol (Å).

	E_{ads}		$d(H_{zeo}\text{-}O_{MeOH})$	
Method	SP	Opt	SP	Opt
H-Y	-100	-96	1.50	1.39
H-ZSM-5 [I2]	-120	-122	1.50	1.41
H-ZSM-5 [Z6]	-115	-114	1.44	1.37
H-ZSM-5 [M7]	-114	-113	1.51	1.38

Throughout, the atomic orbitals are represented using the Ahlrichs and Taylor TZVP Gaussian basis sets[19], explained in Section 2.1.2.3. The self-consistent field (SCF) convergence criteria was set to an energy change of less than 2.72 x 10^{-6} eV (1 x 10^{-7} Hartrees) between SCF iterations.[20,21] The MM energy was calculated using DL_POLY,[22] employing the forcefield of Hill and Sauer[23,24], with the coordination dependent charges in the original forcefield replaced with fixed 1.2 and -0.6 e point charges for silicon and oxygen respectively, as parameterised in the work of Sherwood *et al.*[25] Because we have a neutrally charged system, we employed Restricted Hartree-Fock (RHF) conditions to simulate our models, corresponding to all spins being paired and singlet spin multiplicity.

Geometry optimizations were performed by ChemShell[26] in a Cartesian coordinate space using the Limited-Memory Broyden-Fletcher-Goldfarb-Shanno (L-BFGS) algorithm (detailed in Section 2.1.4), with a convergence threshold of 0.015 eV/Å, gradients of root-mean-square (rms) of 0.002 Ha/a_0, rms of 0.008 a_0, maximum gradient of 0.003 Ha/a_0, maximum displacement of 0.012 a_0.[27,28,29,30] Vibrational frequencies were also calculated using ChemShell, with a task-farmed finite-difference approach[16], allowing us to compute thermal corrections (i.e. free energies) as well as confirm that geometries correspond to local minima.[31,32] For the vibrational calculations, only the active site, first neighbour framework atoms, and the adsorbate atoms were displaced; comparison of this approximation against displacement of all atoms in the QM region shows negligible differences (Table 3.2).

Table 3.2. Results obtained from vibrational frequency calculations of the bi-dentate H-Y model with differing numbers nearest neighbours (NN) included in the finite-difference displacements. Ecorr ZPE, Evib, Sads, representing the correction to the electronic energy in order to obtain the thermodynamic enthalpy, the zero-point energy, the vibrational energy (as calculated using partition function) and the adsorption entropy. All values are presented in kJ/mol except Sads, which is in units of kJ/mol/K. The vibrational frequency, v(Ozeo-Hzeo), is given of the O-H group of the model (cm^{-1}).

	E_{corr}	ZPE	E_{vib}	S_{ads}	v(O_{zeo}-H_{zeo})
2NN	-17	8	16	0.140	3789
3NN	-17	8	16	0.138	3789
4NN	-18	8	16	0.138	3789
5NN	-19	7	16	0.141	3789

No scaling factor has been used to scale our vibrational frequencies, whilst previous work has used a scaling factor to align vibrational frequencies with experiment, with values between 0.9 – 0.9614.[33,34,35,36] In this work no such scaling was pursued due to the absence of necessary benchmarking and derivation in the literature.

3.2.2 Energetic analysis

The adsorption energy (E_{ads}) of an adsorbate is calculated as:

$$E_{\mathrm{ads}} = E[\mathrm{ZeOH+Sorbate}] - E[\mathrm{ZeOH}] - E[\mathrm{Sorbate}] \tag{3.1}$$

where, E[ZeOH], E[Sorbate] and E[ZeOH+Sorbate] are the total energy of the zeolite sorbent, the gas-phase sorbate and the combined guest-host system, respectively, each in their optimised geometry. Due to our use of an atom-centred basis set, it is necessary to include a basis-set-superposition-error (BSSE) [37]for the combined system, which is calculated thus:

$$E_{\mathrm{BSSE}} = \left(E[\mathrm{ZeOH_{ads}} + \mathrm{Basis(Sorbate_{ads})}] - E[\mathrm{ZeOH_{ads}}]\right)$$

$$+ \left(E[\mathrm{Sorbate_{ads}} + \mathrm{Basis(ZeOH_{ads})}] - E[\mathrm{Sorbate_{ads}}]\right) \tag{3.2}$$

where the first term gives the BSSE (E_{BSSE}) for the framework when including the sorbate orbitals, and the second term gives the E_{BSSE} for the sorbate in the presence of the zeolite orbitals. Thus, in both parts the BSSE is calculated as the difference in energy of the system components (ZeOH and Sorbate) in an adsorbed geometry (denoted with $_{\mathrm{ads}}$), with and without the basis functions (denoted as "Basis") for the second component of the complete system. e.g. E(ZeOH) is calculated with and without the basis functions of the sorbate present.[5] All values of E_{BSSE} are given in the Table 3.3, and E_{BSSE} is included in all energies reported; generally, the error is ≤ 5 kJ/mol for a single adsorbed CH_3OH.

*Table 3.3. Total basis set superposition error (BSSE) for all the systems (kJ/mol). * labels represent a bi-molecular systems, with the second molecule around the adsorbed methanol given.*

	H-Y	H-ZSM-5 [I2]	H-ZSM-5 [Z6]	H-ZSM-5 [M7]
Methanol (end-on)	-3	-5	-5	-3
Methanol (side-on)	-3	-4	-3	-2
Methoxy – Water	-2	-2	-1	-2
* Methanol (mono-dentate)	-1	-5	-3	-3
* Methanol (bi-dentate)	-8	-9	-6	-5
* Methanol (tri-dentate)	-7	-6	-7	-5
* Water (bi-dentate)	-6	-6	-4	-3
* Water (mono-dentate)	-4	-6	-5	-5
* Methane (mono-dentate)	-3	-5	-5	-5

Additionally, we determined the distortion energy for each adsorbed system, which characterizes the energetic penalty of structural change for the frameworks and sorbates *post-adsorption.* We also calculated the interaction energy between the zeolite and the sorbed molecules *post-adsorption,* which characterizes the strength of the chemical interaction when the sorbate is bound to the framework. These values allow clarification as to the extent to which the system is strained in order to strengthen E_{ads}. The distortion energy, E_{dist}, is determined for the zeolite as:

$$E_{\text{dist}} = E[\text{ZeOH}_{\text{ads}}] - E[\text{ZeOH}] \qquad (3.3)$$

where $E[\text{ZeOH}_{\text{ads}}]$ is the SCF energy of the zeolite geometry *after* CH_3OH absorption, i.e. with the CH_3OH removed, and $E[\text{ZeOH}]$ is as defined for Equation (3.1). A similar approach to Equation (3.3) exists in the case of CH_3OH, using adsorbed and gas-phase molecular geometries. Subsequently, the interaction energy, E_{int}, is defined as:

$$\text{E}_{\text{int}} = \text{E}_{\text{ads}} - \sum \text{E}_{\text{dist}}, \qquad (3.4)$$

with the sum running over E_{dist} for both the zeolite and CH_3OH components.

3.2.3. Electronic Parameters Analysis

We calculated the chemical hardness (η), chemical potential (μ), band gaps (δ) and electronegativity (χ) of the empty clusters, using the following equations[38]:

$$\eta = -\frac{(\mathrm{IP} - \mathrm{EA})}{2} \quad ; \quad \mu = -\frac{(\mathrm{IP} + \mathrm{EA})}{2} \quad ; \quad \delta = (\mathrm{IP} - \mathrm{EA}) \quad ; \quad \chi = -\mu \qquad (3.5)$$

Where IP (ionisation potential) and EA (electron affinity), are approximated as follows[39,40]:

IP = $-E_{HOMO}$ and EA = $-E_{LUMO}$, where E_{HOMO} and E_{LUMO} are the HOMO and LUMO energies of the corresponding empty clusters.

3.3. Results and Discussion

3.3.1 Adsorption of methanol

To test our approach initially, E_{ads} was calculated for CH_3OH in End-on and an Side-on orientations to the zeolite framework (Figure 3.1). The CH_3OH oxygen is directed towards the acidic site in both cases, but for the Side-on orientation the reactant is positioned parallel to the pore walls, and for the End-on case positioned perpendicular to the walls. Thus, the framework oxygen is coordinated either with the $-CH_3$, or -OH group of CH_3OH, respectively.

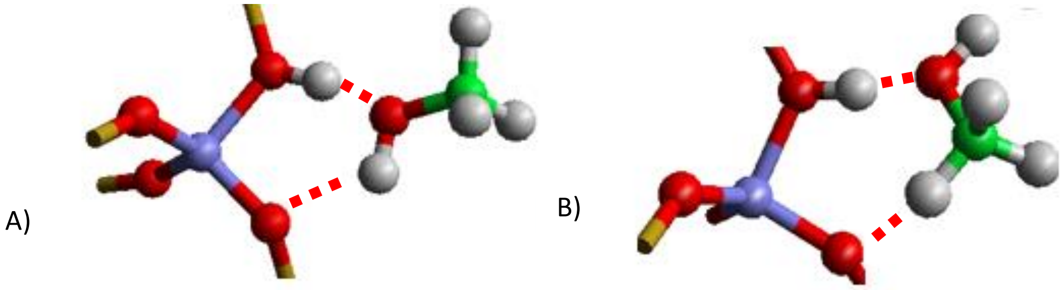

Figure 3.1. Representation of Single CH_3OH *adsorption configurations: A) End-on B) Side-on. Hydrogen-bonds are identified with dotted red lines. Aluminium, hydrogen, carbon and oxygen as shown as purple, white, green and red atoms, respectively.*

E_{ads} is exothermic for all systems (Table 3.4), in the range of -70 to -82 kJ/mol for the End-on configuration and -65 to -85 kJ/mol for the Side-on equivalents for calculations employing the B97-3 functional, with adsorption generally stronger in H-ZSM-5. The results match previous PBC simulations with the PBE exchange-correlation functional[41], which report E_{ads} = -89 kJ/mol for the H-ZSM-5 [I2] site. The results also match embedded-cluster calculations by O'Malley et al.[5], who obtained (corrected) adsorption energies of -62 to -69 kJ/mol in H-Y, using PW91, B3LYP and B97-2 exchange-correlation functionals, which are similar to our results. The same authors reported adsorption energies in H-ZSM-5, with the same functionals, giving results for H-ZSM-5 [I2], [Z6] and [M7] as -50 to -69, -18 to -30, and -84 to -98 kJ/mol respectively. Whilst our I2 and M7 outcomes match this previous work, the difference observed for H-ZSM-5 [Z6] follows from a more comprehensive search in the present work of the energy surface for the adsorbed structure, thus highlighting the general complexity of the potential energy landscape for methanol adsorption. Experimental studies also report E_{ads} as (-90; -110) kJ/mol at 300 K[42] (with the interval based on the type of Td site the Al occupies), -110 kJ/mol at 323 K[43] and -115 kJ/mol at 400 K[44] for H-ZSM-5. It is important to note that differences between experimental and theoretical obtained values, may come from reactant coverage, acid site strength, acid site density[3,45] and a detailed comparison with experiment would need to include thermal effects and the energies of sorbate-sorbate interactions at higher coverage.

Table 3.4. Adsorption energy for CH_3OH, *presented in kJ/mol.*

XC functional:	B97-3		B97-D		MP2	
Site	End on	Side on	End on	Side on	End on	Side on
H-Y	-70	-65	-106	-100	-102	-96
H-ZSM-5 [I2]	-81	-78	-124	-120	-117	-113
H-ZSM-5 [Z6]	-82	-80	-126	-115	-121	-112
H-ZSM-5 [M7]	-81	-85	-115	-114	-107	-113

We note, however, that the B97-3 calculations do not include the effects of dispersion and in order to consider further these effects, we performed additional single point energetic calculations using the B97-3 optimised geometries. E_{ads} was recalculated with the dispersion-corrected version of the B97-3 hybrid-functional, B97-D, as well as an explicitly correlated method in the form of second order Møller-Plesset (MP2) perturbation theory. The dispersion corrections increase the adsorption energies by ~50% (Table 3.4) and are quantitatively similar to the previously reported PBE-D simulations for single methanol (E_{ads} = 115 kJ/mol),[41] and are also much closer to experiment. Generally, the results from these calculations give similar trends to our B97-3 calculations: the H-ZSM-5 active sites promote a higher stability than H-Y, and the same stability hierarchy is observed for the end-on and side-on configurations. However, we also note small discrepancies between functionals in the adsorption energies of the H-ZSM-5 side-on models, which highlights subtle differences in the energy landscape for each separate approach.

Overall, our results confirm that the End-on configuration is marginally more stable for CH_3OH adsorption, matching previous reports [46,47], though there is an exception for the H-ZSM-5 [M7] Side-on model; in this case, geometric analysis shows that the CH_3OH has rotated during optimisation to the End-on geometry (Figure 3.2). Analysis of E_{int} and E_{dist} (Table 3.5) suggests that the overarching reason for the End-on stability is that it distorts the framework less than the Side-on geometry, as E_{dist} is lower in the former case.

Table 3.5. Comparison of energy contributions for the stability of CH_3OH adsorbed in H-Y and H-ZSM-5[I2] (kJ/mol). E_{ads}, E_{int} and E_{dist} correspond to adsorption, interaction and distortion energies, respectively, as defined the main manuscript. $d(H_{zeo}-O_{zeo})$ is the length of the O-H bond at the zeolite acid site (Å).

Site	Adsorbate(s)	Configuration	E_{dist}	E_{int}	E_{ads}	$d(H_{zeo}-O_{zeo})$
H-Y	Methanol	Side-on	33	-103	-70	1.04
		End-on	27	-104	-77	1.05
	Bi-methanol	Bi-dentate	443	-605	-162	1.82
		Tri-dentate	373	-525	-152	1.65
	Methanol/H_2O	Mono-dentate	37	-139	-102	1.06
		Bi-dentate	411	-553	-142	1.73
	Methanol/CH_4	Bi-dentate	34	-111	-77	1.05
H-ZSM-5 [I2]	Methanol	Side-on	18	-104	-86	1.05
		End-on	19	-110	-91	1.05
	Bi-methanol	Bi-dentate	375	-535	-160	1.67
		Tri-dentate	303	-456	-153	1.53
	Methanol/H_2O	Mono-dentate	220	-318	-98	1.39
		Bi-dentate	351	-497	-146	1.64
	Methanol/CH_4	Bi-dentate	18	-98	-70	1.05

Again, this difference can be observed structurally in Figure 3.2, with the $-CH_3$ groups only loosely coordinated with the framework for Side-on orientations. Furthermore, the methyl group ($-CH_3$) is positioned towards the centre of the zeolite pore for all End-on geometries; thus, direct bonding interactions with the framework are fewer in this model, with only direct interactions occurring through the -OH group. Overall, E_{ads} is similar for all sites considered in H-ZSM-5. Comparing adsorption geometries in H-Y and H-ZSM-5, the distance between framework Brønsted sites and -OH groups are consistent throughout, despite notably different adsorption energies for the frameworks, which indicates that additional interactions play a role in the stabilisation of CH_3OH. For further insight about single methanol adsorption on zeolites, we refer the reader to previous work on this field. [7,48,49,50,51]

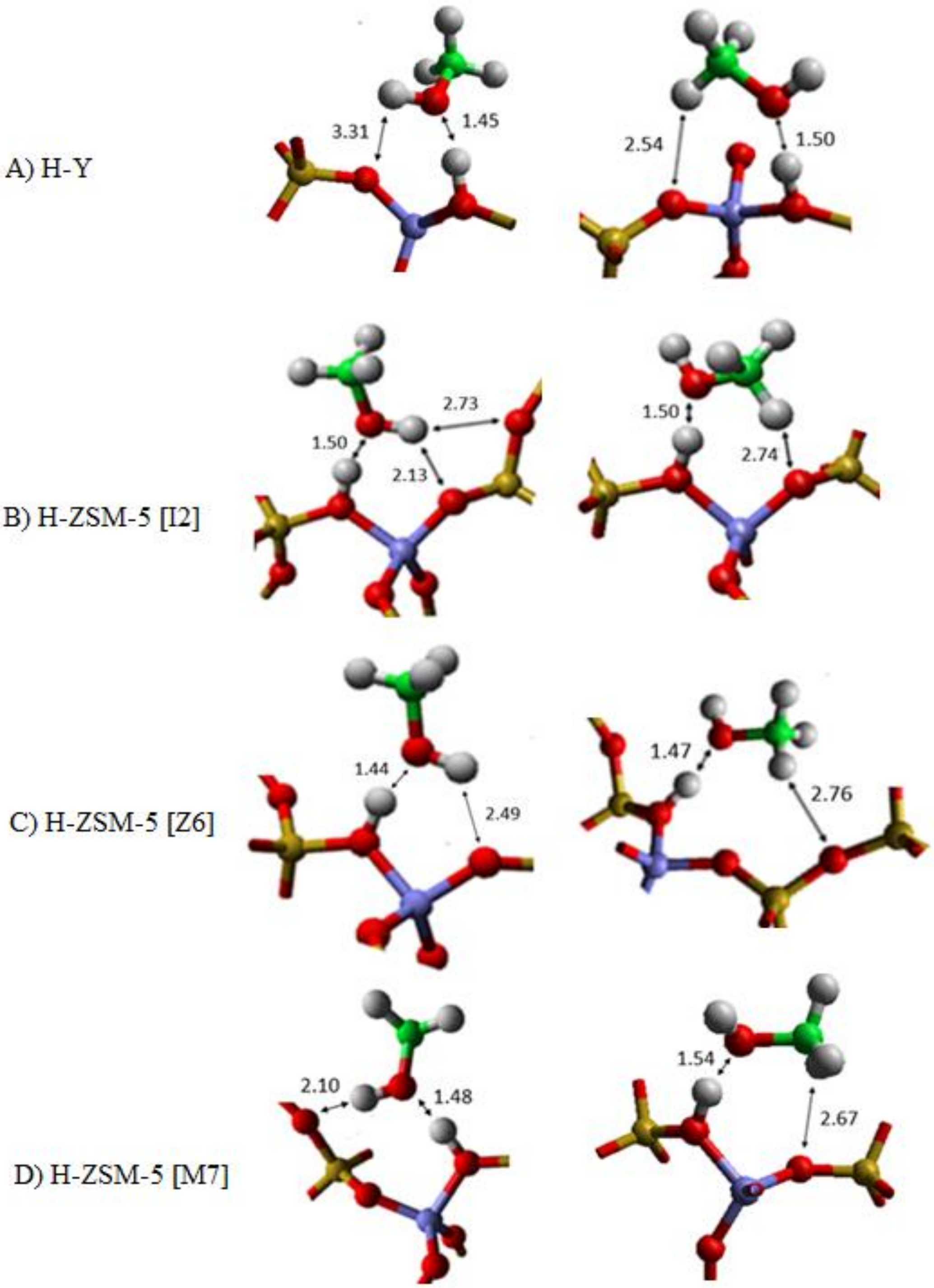

Figure 3.2 Focused view of zeolite pores showing the B97-3 optimised geometries of CH_3OH *adsorbed End-on (left) and Side-on (right) at the zeolite active sites. Hydrogen-oxygen interaction distances are indicated by double-headed arrows (Å). Atoms are coloured as in Figure 3.1.*

Table 3.6 gives the geometric interactions for the adsorbed methanol with the zeolite framework.

Table 3.6. Details of the primary hydrogen bond length between the methanol oxygen and zeolite H, denoted d(O_{MeOH}*-*H_{zeo}*), and number of secondary hydrogen-type bonding interactions between the -OH and -*CH_3 *molecular fragments of the* CH_3OH *and the zeolite framework. The length of the primary hydrogen bond is given in Å.*

	Side-on			End-on		
		H-bonds			*H-bonds*	
	d(O_{MeOH}-H_{zeo})	-OH	-CH_3	d(O_{MeOH}-H_{zeo})	-OH	-CH_3
H-Y	1.50	-	2	1.45	2	-
H-ZSM-5 [I2]	1.50	-	1	1.50	2	1
H-ZSM-5 [Z6]	1.44	2	3	1.47	2	-
H-ZSM-5 [M7]	1.48	-	1	1.57	2	-

Beyond the primary hydrogen bond between the methanol -OH and framework Brønsted site, we have tabulated all additional hydrogen bonds with an interatomic distance below 3 Å. Here, we focus on hydrogen bonds between a framework oxygen and a hydrogen of either the -OH or -CH_3 groups on CH_3OH, irrespective of directionality; greater detail is presented in Table 3.7.

Table 3.7. Long-range molecular interaction distances for methanol adsorbed in the zeolite framework (Å). Molecular configurations and definitions of "short" and "long" are given in the main text; no directionality is considered in the interactions

	Side-on				End-on		
Site	short		Long		short	long	
	-OH	$-CH_3$	-OH	$-CH_3$	-OH	-OH	$-CH_3$
H-Y	-	2.45; 2.94	3.57; 3.68	3.27; 3.62; 3.74	2.50; 2.93	3.01; 3.31; 3.35; 4.00	3.54; 3.80; 3.80
H-ZSM-5 [I2]	-	2.74	3.20; 3.42; 3.94	3.35; 3.61; 3.87; 3.97; 3.67; 3.87; 3.99	2.13; 2.73	3.66	3.63; 3.68; 3.89; 3.72; 3.98
H-ZSM-5 [Z6]	2.58; 2.88	2.72; 2.76; 2.79	3.86; 3.87; 3.96	3.19; 3.35; 3.58; 3.61; 3.89; 3.99; 3.14; 3.37; 3.56; 3.81; 3.83	2.49; 2.67	3.15; 3.87	3.08; 3.33; 3.24; 3.46; 3.47; 3.05; 3.52; 3.58; 3.86
H-ZSM-5 [M7]	-	2.73	3.15; 3.20	3.24; 3.83; 3.16; 3.49; 3.68; 3.84; 3.96	2.10; 2.60	3.16; 3.41; 3.55	3.42; 3.73; 3.30; 3.20; 3.44; 3.65; 3.66; 3.52; 3.54; 3.49; 3.69; 3.48

The most significant stabilising effect is expected from the $\text{-OH}_{\text{MeOH}}\cdots\text{O}_{\text{Zeo}}$ interaction, due to the stronger dipole in the -OH moiety (higher acceptor character); however, we also include the $\text{-CH}_{\text{MeOH}}\cdots\text{O}_{\text{zeo}}$ interaction in light of theoretical[52] and experimental[53] studies.

Table 3.6 suggests that the secondary hydrogen bonds, additional to the primary interaction between O_{MeOH} and H_{zeo}, can influence E_{ads}. In particular, E_{ads} is marginally stronger for End-on models where the quantity of shorter secondary interactions is high. For Side-on, the tight pore active sites of H-ZSM-5 [Z6] and H-ZSM-5 [M7] have caused the methanol to rotate so that the -OH group of the methanol is in fact closer to the framework than the $-CH_3$ group (Figure 3.2), which indicates that directionality in the -OH bond is important.

3.3.2 Bi-methanol systems

Previous work studying the FER framework, has shown that including additional CH_3OH at the adsorption site may result in spontaneous methanol protonation, subsequently lowering the energy barrier for methoxylation.[7] Following this observation, we now consider the role of additional neighbouring molecules in our H-Y and H-ZSM-5 models. Firstly, we have considered a second CH_3OH, and have constructed three different bi-methanol configurations (Figure 3.3).

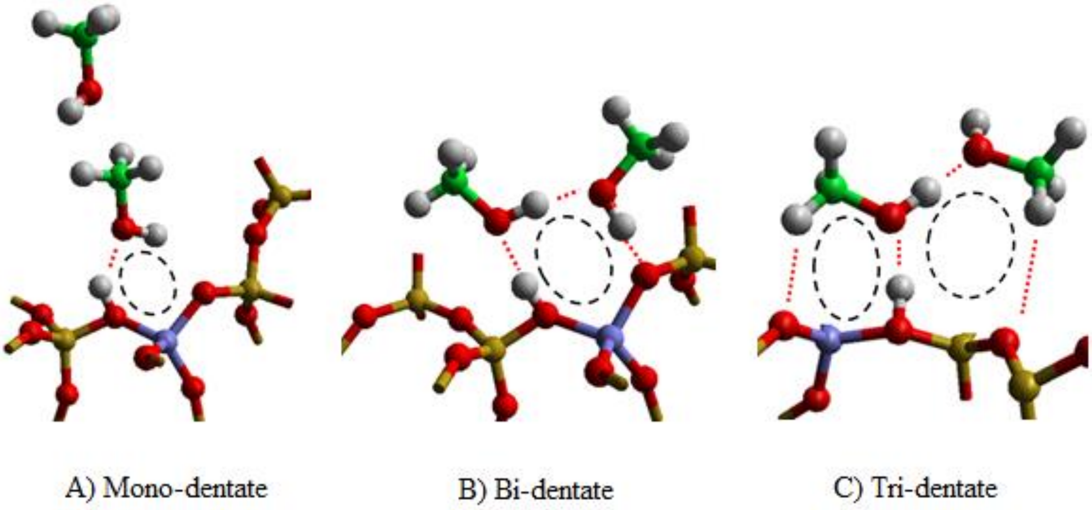
A) Mono-dentate B) Bi-dentate C) Tri-dentate

Figure 3.3. Models of bi-methanol configurations considered in this work: A) mono-dentate, B) bi-dentate, C) tri-dentate. As for Figure 3.1, hydrogen bonds are marked with dotted red lines and coordination-rings are represented by dashed circles. Atom colours are as for Figure 3.1.

Fig. 3.3A) shows the "mono-dentate" configuration, which is considered the most direct pathway to the formation of DME [54]. In this model, the End-on structure interacts with a second methanol molecule through its $-CH_3$ group; thus, the CH_3OH

coordination with the framework can be directly compared to the adsorption of the single End-on molecule (Section 3.3.1). Two further bi-methanol configurations were considered: an extended 8-membered coordination ring, denoted as "bi-dentate" (Fig. 3.3B), or two coordination rings formed by the Side-on methanol molecules and the zeolite framework, which we term "tri-dentate" (Fig. 3.3C). As for the single methanol adsorption, we first performed geometry optimisations using the hybrid B97-3 exchange-correlation functional before also performing single point calculations using B97-D and MP2 approaches, with the results presented in Table 3.8. The dispersion-corrected approaches gave E_{ads} as ~50% more negative; however, though there are some subtle variations in the energetic ordering for adsorption sites, the overall trends of the B97-3, B97-D and MP2 results are similar, detailed discussion of which is presented in the following sub-sections.

Table 3.8. Calculated adsorption energies when using density functional theory with B97-3, B97-D exchange-correlation functionals, or higher-level MP2 simulations (kJ/mol). The adsorption energy of the secondary CH_3OH, i.e. energy change relative to the single, end-on adsorbed CH_3OH, is given in parentheses.

	B97-3			
	H-Y	H-ZSM-5		
		[I2]	[Z6]	[M7]
Mono-dentate	-90 (-20)	-98 (-17)	-94 (-12)	-82 (-1)
Bi-dentate	-146 (-76)	-142 (-61)	-126 (-44)	-125 (-44)
Tri-dentate	-128 (-58)	-141 (-60)	-126 (-44)	-129 (-48)
	B97-D			
Mono-dentate	-139 (-33)	-160 (-36)	-144 (-18)	-119 (-4)
Bi-dentate	-219 (-113)	-218 (-94)	-196 (-70)	-197 (-82)
Tri-dentate	-199 (-93)	-223 (-99)	-185 (-59)	-189 (-74)
	MP2			
Mono-dentate	-133 (-31)	-180 (-63)	-141 (-20)	-113 (-6)
Bi-dentate	-211 (-109)	-206 (-89)	-191 (-70)	-190 (-83)
Tri-dentate	-192 (-90)	-216 (-99)	-180 (-59)	-180 (-73)

3.3.2.1. Mono-dentate methanol adsorption

E_{ads} for the mono-dentate models are given in Table 3.9. Structural analysis (with geometries given in Figure 3.4) shows that the methanol molecule undergoes spontaneous protonation in the two more “open” models (H-Y and H-ZSM-5 [I2]), where the framework Brønsted acid has transferred to the primary CH_3OH. Experimental studies detected the presence of the H-O-H^+ signal, not only when having a dimer[6] or trimer[55,56] adsorbed on the active site, but also when a single methanol[55,57,58] is adsorbed.

We propose that the proton transfer occurs because the additional CH_3OH interacts with the -CH_3 group of the framework adsorbed CH_3OH, which then diminishes induction effects on the oxygen of this framework bound CH_3OH.

Table 3.9. Summary of adsorption energies (E_{ads}) and geometric parameters (distances, d) for the most stable bi-methanol adsorption in zeolites H-Y an H-ZSM-5. For the geometric characterisation, "short" hydrogen-bonds of the adsorbed bi-methanol structures are given: 'H1' and 'H2' are the quantity of hydrogen-bonds formed by the -OH groups on the primary and second CH_3OH, respectively, whilst 'HC1' and 'HC2' represent the hydrogen bonds formed from the $-CH_3$ groups of each respective molecule to the zeolite framework. Where appropriate, the parent structure of the atoms, either zeolite (zeo) or methanol (MeOH) is given in subscript after the atomic label. Geometric observables are presented in Å, and E_{ads} in kJ/mol, with the results displayed in bold corresponding to the cases where spontaneous proton transfer occurred.

Site	E_{ads} (B97-3)	$d(H_{zeo}-O_{zeo})$	$d(H_{MeOH1}-O_{MeOH2})$	H1	H2	HC1	HC2
Mono-dentate							
H-Y	**-90**	1.42	2.57	1	-	-	-
H-ZSM-5 [I2]	**-98**	1.69	2.78	2	1	-	2
H-ZSM-5 [Z6]	-94	1.05	2.34	1	2	1	1
H-ZSM-5 [M7]	-82	1.04	2.22	1	-	2	2
Bi-dentate							
H-Y	**-146**	1.82	1.33	1	2	-	2
H-ZSM-5 [I2]	**-142**	1.67	1.45	1	2	1	3
H-ZSM-5 [Z6]	**-126**	1.52	1.55	-	2	1	7
H-ZSM-5 [M7]	**-125**	1.67	1.40	-	2	2	2
Tri-dentate							
H-Y	**-128**	1.73	1.51	-	-	2	1
H-ZSM-5 [I2]	**-141**	1.53	1.50	-	3	2	4
H-ZSM-5 [Z6]	**-126**	1.60	1.49	-	2	3	-
H-ZSM-5 [M7]	**-129**	1.49	1.52	-	2	2	4

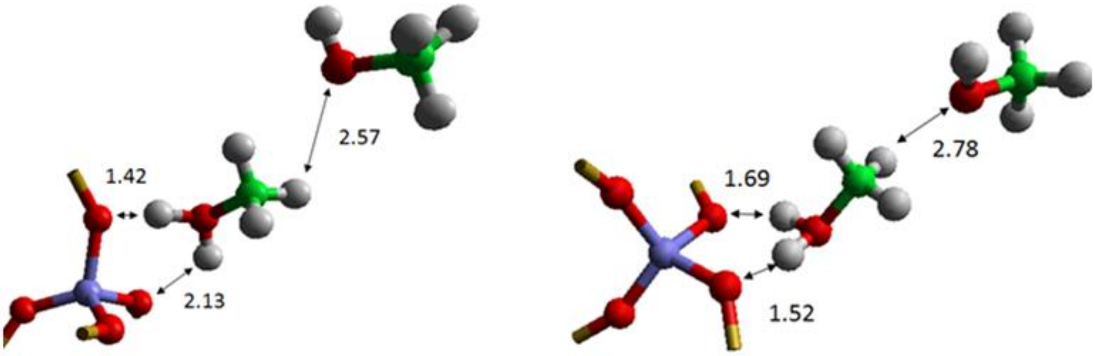

A) H-Y

B) H-ZSM-5 [I2]

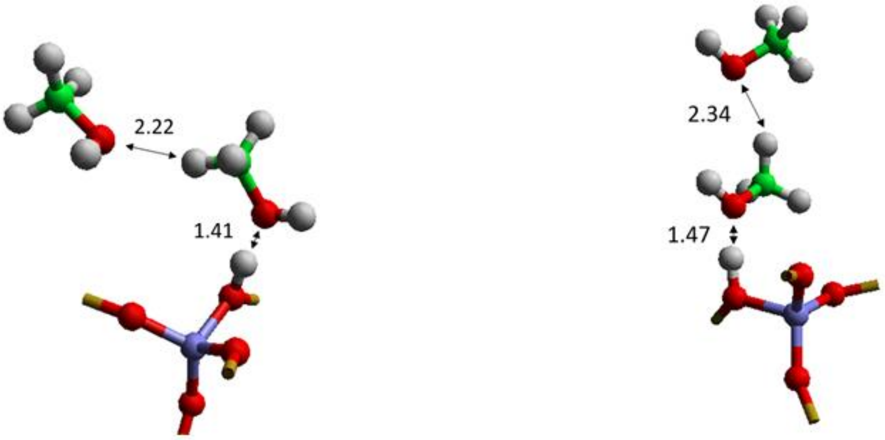

C) H-ZSM-5 [Z6]

D) H-ZSM-5 [M7]

Figure 3.4. Adsorbed B97-3 optimised geometries of mono-dentate bi-methanol in H-Y and H-ZSM-5. Hydrogen-bond distances are marked by arrows, with values given in Å. The atom colours are as in Figure 3.1.

Figure 3.4 shows the geometries for the mono-dentate systems, with E_{ads} and -OH···O interaction distances documented in Table 3.9. For H-Y, E_{ads} is -90 kJ/mol, which is stronger than the -70 kJ/mol observed for the single CH_3OH. Despite a higher number of $-OH_{MeOH}\cdots O_{zeo}$ interactions in H-ZSM-5 (with detailed geometric values given in Table 3.10 and 11), E_{ads} is similar both when a methyloxonium ion is formed and when the proton remains bound to the framework, from which we conclude that the electrostatic interactions between the zeolite proton (H_{zeo}) and the hydroxyl group of the methanol (-OH_{MeOH}) are important in stabilizing the bi-methanol structure (Partial charges on each atom are presented in Table 3.12)

Table 3.10. Summary of the distances between atoms for the bimethanol configuration with all values presented in Å. Labels are as given in Figure 3.5.

Site	d(H0-O0)	d(H0-O1)	d(O2-H1)	d(O1-C2)
	Mono-dentate			
H-Y	1.42	1.06	2.57	1.47
H-ZSM-5 [I2]	1.69	0.97	2.78	1.47
H-ZSM-5 [Z6]	1.41	0.96	2.22	1.45
H-ZSM-5 [M7]	1.47	0.96	2.34	1.45
	Bi-dentate			
H-Y	1.82	0.99	1.33	1.46
H-ZSM-5 [I2]	1.67	1.00	1.45	1.46
H-ZSM-5 [Z6]	1.52	1.03	1.55	1.46
H-ZSM-5 [M7]	1.67	1.00	1.40	1.46
	Tri-dentate			
H-Y	1.73	1.00	1.51	1.47
H-ZSM-5 [I2]	1.53	1.02	1.5	1.46
H-ZSM-5 [Z6]	1.6	1.02	1.49	1.45
H-ZSM-5 [M7]	1.49	1.03	1.52	1.46

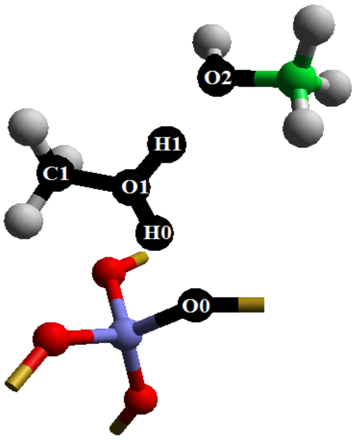

Figure 3.5. Schematic representation of atomic labels when computing bond distances: H0-O0 represents the distance between the Brønsted proton to the zeolite framework, H0-O1 represents the distance between the Brønsted proton to the oxygen of the first methanol, H1-O2 represents the distance between the hydrogen of the first methanol and the oxygen of the second methanol.

Table 3.11. Distances in the bi-methanol configurations between methanol and the zeolite framework. 'H1' and 'H2' represent hydrogen bonds of the -OH groups and 'HC1' and 'HC2' representing the hydrogen bonds of the -CH_3 groups, respectively, from the first and second methanol molecule (Å).

Site	H1	H2	HC1	HC2
	Mono-dentate			
H-Y	2.13	-	-	-
H-ZSM-5 [I2]	1.52; 2.56	2.75	-	2.45; 2.52
H-ZSM-5 [Z6]	-	2.20; 2.89	2.68	2.93
H-ZSM-5 [M7]	-	-	2.78; 2.80	2.70; 2.88
	Bi-dentate			
H-Y	2.77	2.07; 2.79	-	2.90; 2.66
H-ZSM-5 [I2]	2.65	2.19; 2.92	2.87	2.34; 2.71; 2.93
H-ZSM-5 [Z6]	-	2.33; 2.58	2.79	2.01; 2.20; 2.60; 2.13; 2.26; 2.60; 2.89
H-ZSM-5 [M7]	-	1.95; 2.78	2.63; 2.91	2.46; 2.48
	Tri-dentate			
H-Y	-	-	2.38; 2.81	3.00
H-ZSM-5 [I2]	-	2.20, 2.75, 3.02	2.55; 2.65	2.82; 2.06, 2.47, 2.78
H-ZSM-5 [Z6]	-	2.65, 3.00	2.63, 2.95; 3.00	-
H-ZSM-5 [M7]	-	2.81, 3.00	2.55, 2.94	2.24, 2.43; 2.43, 2.67

Table 3.12. Comparison of the relative Mulliken partial charges to gas phase methanol located on each atom presented the in first column, of bi-methanol system in H-Y, provided in atomic units, with the hydrogen atoms of the OH group of the methanol highlighted by the '' sign, with labels as per Figure 3.5.*

	Mono-dentate	Tri-dentate	Bi-dentate
Al	0.03	0.04	0.06
O0	0.10	0.07	0.08
O	0.02	0.04	0.04
O	-0.01	-0.01	-0.01
O	0.08	0.01	0.09
H0	-0.12	-0.07	-0.10
C1	0.00	0.03	-0.01
H1	-0.03	-0.08	-0.05
H1	0.01	-0.08	-0.01
H1	-0.02	-0.08	-0.06
O1	0.04	-0.08	0.04
H1*	-0.02	-0.09	-0.11
C2	0.01	0.01	0.04
H2	-0.08	-0.05	-0.08
H2	-0.04	-0.03	-0.03
H2	-0.10	-0.07	-0.09
O2	-0.08	0.09	-0.06
H2*	0.00	-0.02	-0.02

3.3.2.2 Bi-dentate methanol adsorption

As shown in Tables 3.8 and 3.9, the ordering of E_{ads} for the bi-dentate adsorption (from strongest to weakest) is H-Y > H-ZSM-5 [I2] > H-ZSM-5 [M7] > H-ZSM-5 [Z6]. A correlation is observed between E_{ads} and the size of the local space around the zeolite active site: H-ZSM-5 channel sites (M7 and Z6) are smaller, and so bonding of the two methanol molecules is weaker, whereas the larger open cages of H-Y and H-ZSM-5 [I2] do not have similar steric limitations. The bi-dentate configurations with highest stability also have a more pronounced proton transfer, shown by the longer d(H_{zeo}-O_{zeo}) in Table 3.9 and Figures 3.6 and 3.7. In general, proton transfer occurs more readily when the two methanol molecules are closer together, as is shown by the correlation evident in Figure 3.7. This trend is further highlighted by the charge transfer on to the hydrogen atoms of the methyloxonium H-O-H^+, which is higher in the bi-dentate configuration compared to the mono- and tri-dentate cases (Table 3.12), which may be an indication as to why the MTH process occurs faster at higher reactant loading[59,60] and also suggest a possible first step of this reaction, as we will discuss later in our analysis. Furthermore, the most stable adsorbed structures (H-ZSM-5 [I2], H-Y, E_{ads} ~145 kJ/mol) have more additional hydrogen bonds than the least stable (H-ZSM-5 [M7], H-ZSM-5 [Z6]), with the OH···O interactions between molecules and framework clearly influential.

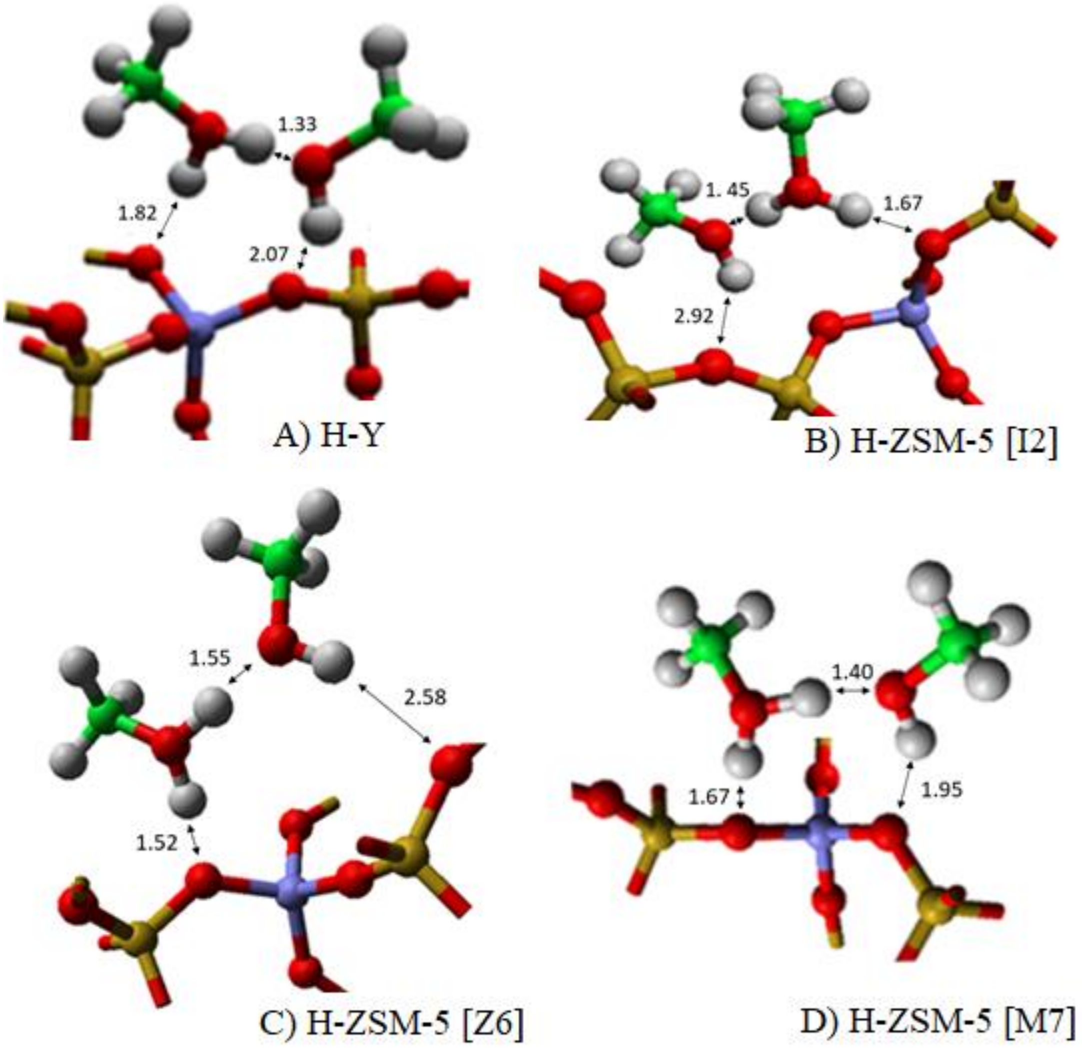

Figure 3.6. Adsorbed B97-3 optimised bi-dentate geometries in zeolite H-Y and H-ZSM-5. Colour scheme is as for Figure 3.1. All distances are marked with arrows and given in Å.

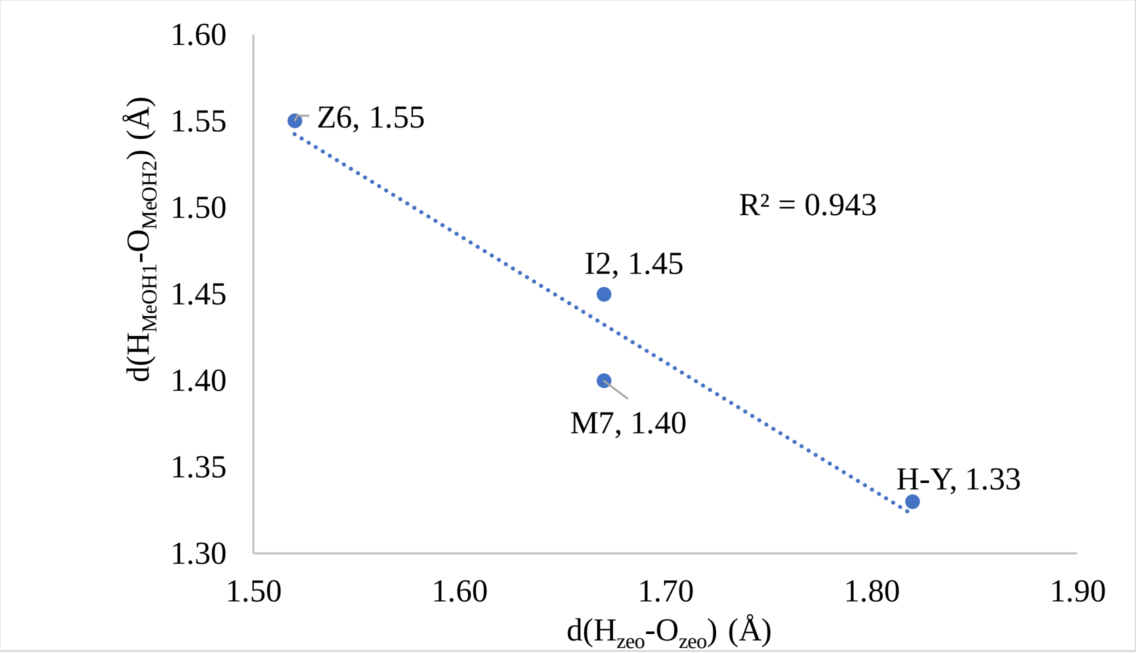

Figure 3.7. Distance, d, between framework oxygen and protons (H_{zeo}-O_{zeo}) plotted against distance between the two methanol molecules (H_{MeOH1}-O_{MeOH2}) in the bi-dentate configuration (Å). The dotted line is given to guide the eye, with an R^2 given to quantify error in the fit.

3.3.2.3. Tri-dentate methanol adsorption

The adsorption energies for the tri-dentate arrangements are comparable to those of the bi-dentate (Tables 3.8 and 3.9), with the most stable tri-dentate configuration (displayed in Figure 3.8) observed in the H-ZSM-5 [I2] structure (-141 kJ/mol). All other frameworks give E_{ads} of -126 to -129 kJ/mol. As with the bi-dentate adsorption, spontaneous proton transfer is observed for the tri-dentate adsorption, resulting in the formation of a methyloxonium ion; however, the hydrogen bonds are slightly different with d(O_{zeo}-H_{zeo}) ~0.1 Å shorter than in the bi-dentate structures. More hydrogen bonds are formed in H-ZSM-5 zeolites than H-Y, due to the smaller size of the H-ZSM-5 channel sites.

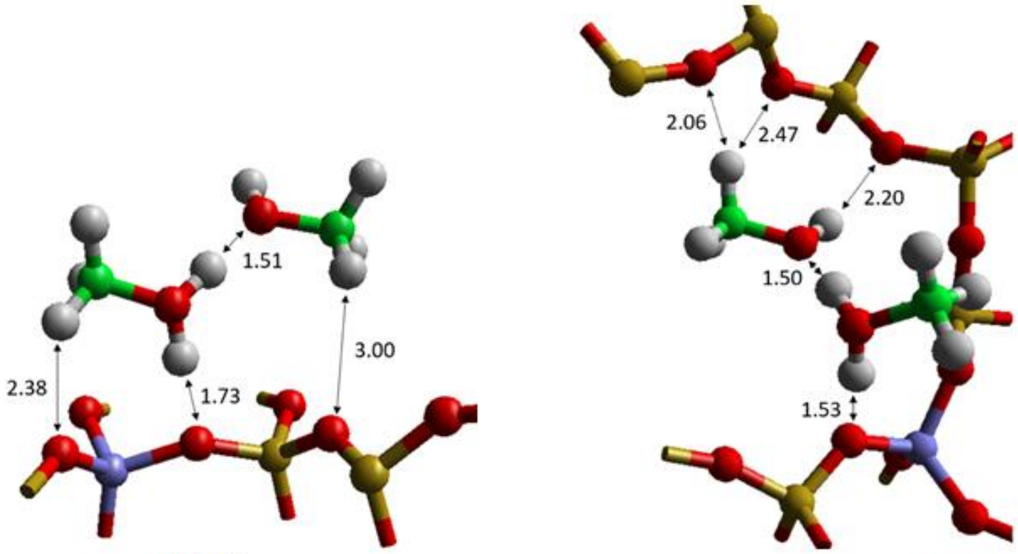

A) H-Y

B) H-ZSM-5 [I2]

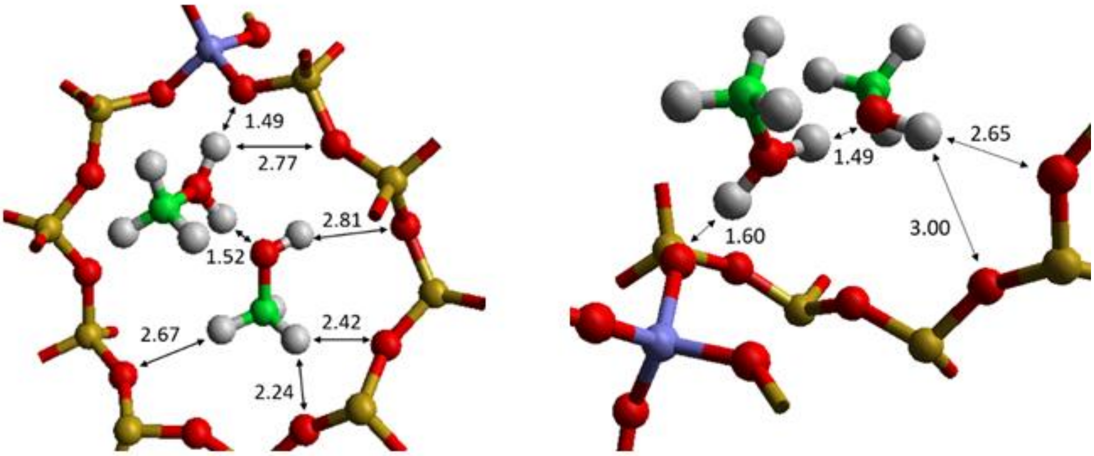

C) H-ZSM-5 [Z6]

D) H-ZSM-5 [M7]

Figure 3.8. The adsorbed B97-3 optimised geometries of the tri-dentate bi-methanol. Hydrogen bonds distances are illustrated with double-headed arrows (Å). The atom colours are as in Figure 3.1 of the main manuscript.

3.3.3 Adsorption of methanol in presence of alternative molecular species

Thus far, we have focussed primarily on how the geometry and interactions between CH_3OH molecules around the active site affects E_{ads}. However, other reactants and/or products may be in the reaction stream, and E_{ads} can be affected by their presence. For instance, H_2O, which is a product of framework methoxylation, can form hydrogen bonds with the -OH groups of CH_3OH, which will not be possible with CH_4, a possible feed impurity. We therefore test both H_2O and CH_4 as secondary environmental molecules, which allows us further to compare and contrast the hydrogen-bonding effects on adsorption energies. Building on our models of a single CH_3OH adsorbed at the Brønsted site, various configurations were considered for H_2O (mono and bi-dentate; displayed in Figures 3.9 and 3.10) and CH_4 (bi-dentate; Figure 3.11), with all new structures geometry optimised with the B97-3 functional. As before, outcomes were compared to dispersion-corrected B97-D exchange-correlation functional and MP2 approaches to obtain perspective on how long-distance interactions affect the energetics reported.

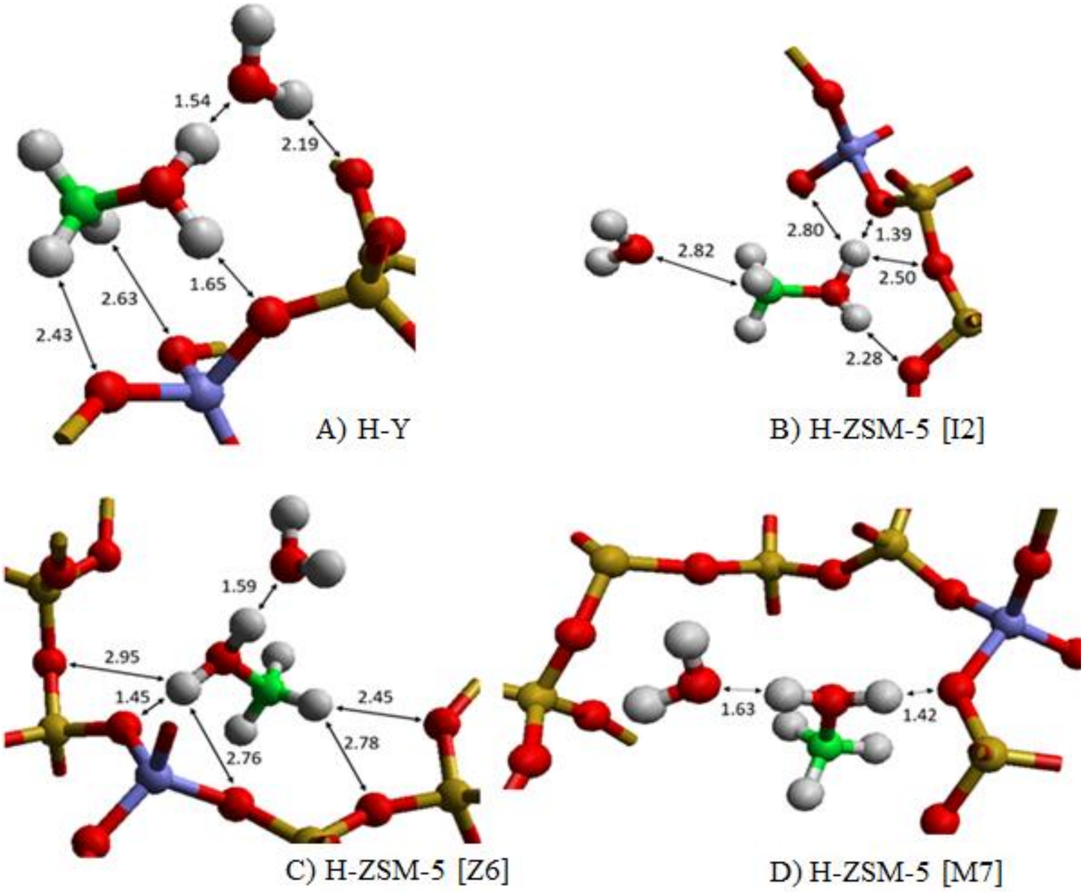

A) H-Y

B) H-ZSM-5 [I2]

C) H-ZSM-5 [Z6]

D) H-ZSM-5 [M7]

Figure 3.9. The B97-3 optimised geometries of the CH_3OH/H_2O models in a mono-dentate configuration, with zeolite pores as labelled and hydrogen bonds distances given with double-headed arrows (Å). The atom colours are as in Figure 3.1 of the main manuscript.

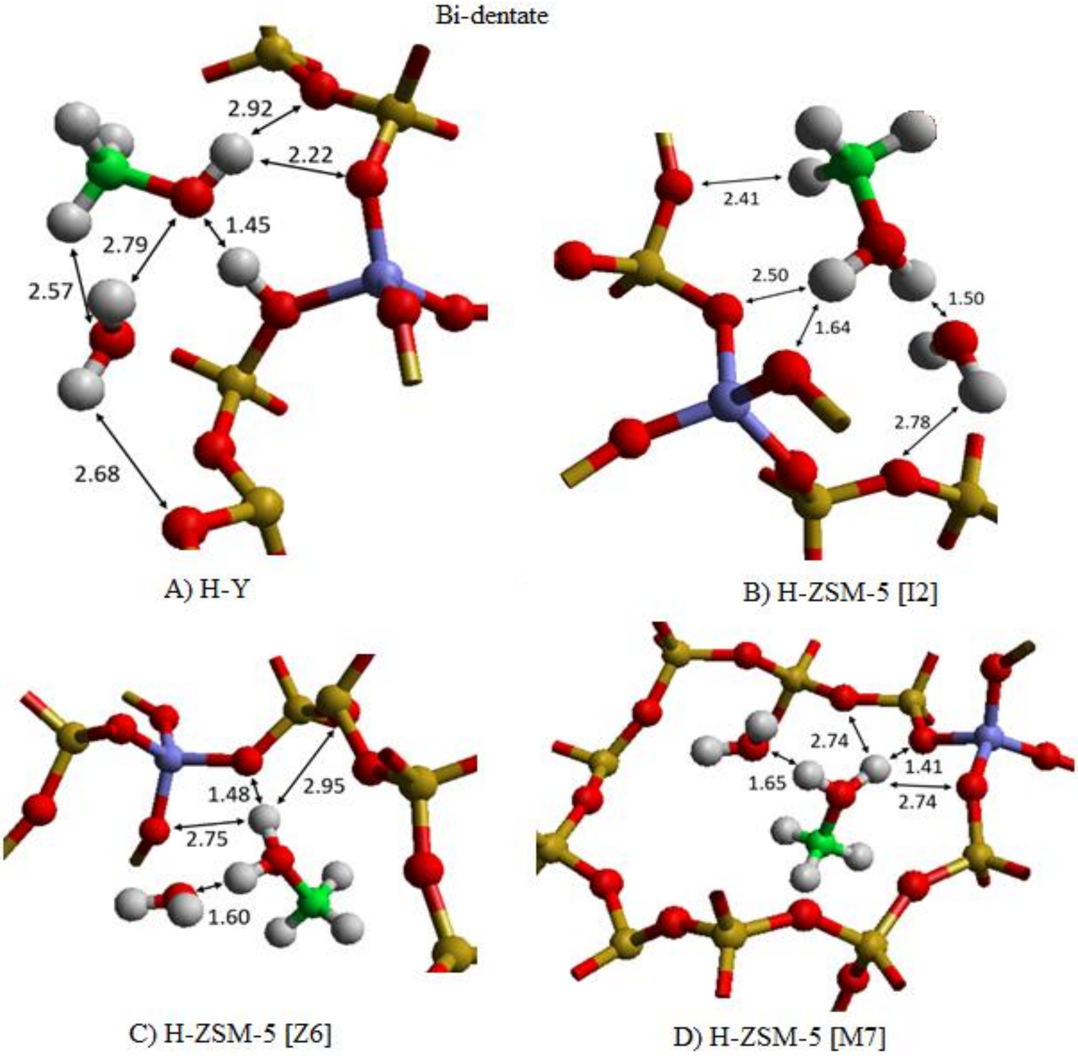

A) H-Y

B) H-ZSM-5 [I2]

C) H-ZSM-5 [Z6]

D) H-ZSM-5 [M7]

Figure 3.10. The B97-3 optimised geometries of the CH_3OH/H_2O models in a bi-dentate configuration, with zeolite pores as labelled and hydrogen bonds distances given with double-headed arrows (Å). The atom colours are as in Figure 3.1 of the main manuscript.

E_{ads} for CH_3OH/H_2O and CH_3OH/CH_4 co-adsorption in the 4 different systems is presented in Table 3.13; as the dispersion-corrected approaches give similar trends to the B97-3 calculated adsorption energies, only the latter is discussed in detail. For H_2O, the strongest adsorption in the mono-dentate configuration is for the more confined H-ZSM-5 [Z6] and H-ZSM-5 [M7] sites; for the bi-dentate, H-ZSM-5 [Z6] is also the most stable adsorption site. This is contrary to CH_3OH co-adsorption, where the more open H-Y and H-ZSM-5 [I2] sites are more stable, and thus indicates steric and/or electronic effects differ in the pores for these different molecular species.

Table 3.13. The adsorption energies of the CH_3OH and second species, H_2O or CH_4, with the adsorption energy of just the second molecule (relative to a single, end-on adsorbed CH_3OH) given in parenthesis (kJ/mol), with the results presented in bold corresponding to the cases where spontaneous proton transfer occurs.

Model	H-Y	H-ZSM-5 [I2]	H-ZSM-5 [Z6]	H-ZSM-5 [M7]
B97-3				
H_2O Mono-dentate	**-90 (-25)**	**-84 (-3)**	**-133 (-51)**	**-123 (-42)**
H_2O Bi-dentate	**-134 (-64)**	**-134 (-53)**	**-148 (-66)**	**-126 (-45)**
CH_4 Bi-dentate	-70 (0)	-70 (11)	-72 (9)	-91 (-10)
B97-D				
H_2O Mono-dentate	**-140 (-34)**	**-139 (-15)**	**-185 (-59)**	**-175 (-60)**
H_2O Bi-dentate	**-189 (-83)**	**-206 (-82)**	**-202 (-76)**	**-181 (-66)**
CH_4 Bi-dentate	-112 (-6)	-126 (-2)	-123 (3)	-148 (-33)
MP2				
H_2O Mono-dentate	**-138 (-36)**	**-129 (-12)**	**-185 (-64)**	**-170 (-63)**
H_2O Bi-dentate	**-185 (-83)**	**-197 (-80)**	**-198 (-77)**	**-173 (-66)**
CH_4 Bi-dentate	-104 (-2)	-118 (-1)	-118 (3)	-146 (-39)

Overall adsorption energies are comparable to the bi-methanol adsorption and also, as with the bi-methanol systems, the framework proton on H-ZSM-5 transfers spontaneously to CH_3OH in the presence of H_2O. This proton transfer is also observed for the bi-dentate complex in H-Y, but not the mono-dentate structure. For CH_4 in the neighbouring environment (i.e. CH_3OH/CH_4), the change in E_{ads} relative to the single methanol is negligible. Energy differences range only from 9 to -6 kJ/mol for the B97-3 exchange-correlation functional; furthermore, no proton transfer occurs, illustrating the importance of hydrogen-bonding from a polarizable -OH group in order to facilitate proton transfer and strong adsorption.

When analysing the geometry of the adsorbed structures, proton transfer from the framework to the CH_3OH generally correlates with higher E_{ads} for CH_3OH/H_2O (detailed in Tables 3.14 and 3.15), with the exception of the mono-dentate H-Y.

Table 3.14. Summary of geometric observables for the water models, presented in Å. The notations given are described in detail in Figure 3.5, except with 'H-O2' representing the smallest hydrogen-bond formed between any hydrogen from the methanol (methyl or hydroxyl) and the oxygen of the water molecule.

Site	H0-O0	H0-O1	O1-H1	H-O2	O1-C1
	Mono-dentate				
H-Y	1.06	1.45	0.96	2.57	1.44
H-ZSM-5 [I2]	1.39	1.08	0.97	2.82	1.48
H-ZSM-5 [Z6]	1.45	1.04	1.01	1.59	1.46
H-ZSM-5 [M7]	1.41	1.06	1.00	1.65	1.45
	Bi-dentate				
H-Y	1.65	1.01	1.02	1.54	1.47
H-ZSM-5 [I2]	1.64	1.00	1.03	1.5	1.46
H-ZSM-5 [Z6]	1.48	1.04	1.00	1.6	1.46
H-ZSM-5 [M7]	1.42	1.06	1.00	1.63	1.45

Table 3.15. Summary of bond distances (Å) and the number of "short" distances for bi-molecular CH_3OH/H_2O models. -OH_{MeOH} and -CH_3 identify H-bond interactions with the H atoms of the methanol hydroxyl and methyl, respectively, and -OH_{H2O} denotes interaction by hydrogen-bonds formed to the H_2O. For the distances, d, the parent structure of the relevant atoms, either zeolite (zeo), methanol (MeOH) or water (H_2O), is given in subscript after the atomic label. The adsorption energy is also given, presented in kJ/mol.

	d(H_{zeo}-O_{zeo})	d(H_{MeOH}-O_{H2O})	-OH_{MeOH}	-CH_3	-OH_{H2O}	E_{ads}
	Mono-dentate					
H-Y	1.06	2.57	2	3	2	-90 (-20)
H-ZSM-5 [I2]	1.39	2.82	2	1	4	-84 (-3)
H-ZSM-5 [Z6]	1.45	1.59	-	3	1	-133 (-51)
H-ZSM-5 [M7]	1.41	1.65	-	1	-	-123 (-42)
	Bi-dentate					
H-Y	1.65	1.54	-	2	2	-134 (-65)
H-ZSM-5 [I2]	1.64	1.5	-	3	5	-134 (-53)
H-ZSM-5 [Z6]	1.48	1.6	-	2	2	-148 (-54)
H-ZSM-5 [M7]	1.42	1.63	-	-	2	-126 (-45)

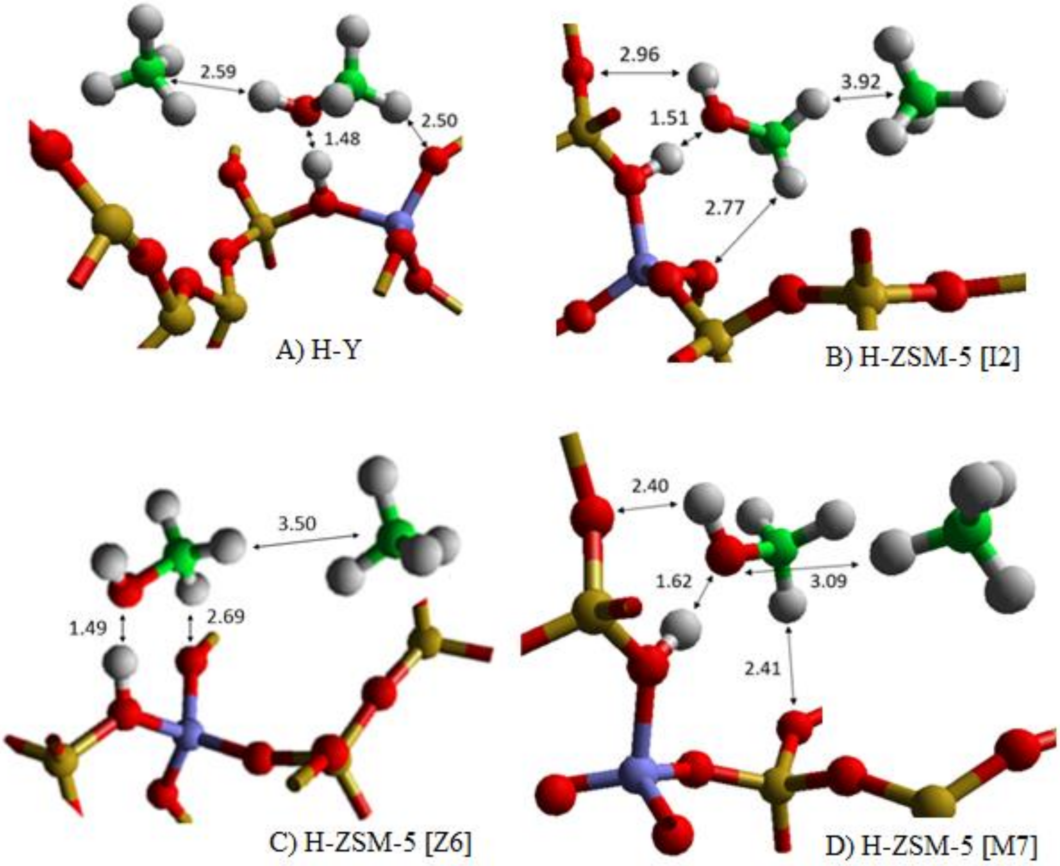

Figure 3.11. The B97-3 optimised geometries of the CH_3OH and CH_4 models in zeolite pores, with interatomic distances given in Ångstroms. The atom colours are as in Figure 3.1.

For the mono- and bi-dentate CH_3OH/H_2O H-ZSM-5 models, proton transfer from the framework to methanol again correlates with the proximity of the two reactants (Figure 3.12). From this observation, we suggest that the pore curvature influences the H_2O positioning close to the CH_3OH or the active site, with the former resulting in proton transfer to the CH_3OH.

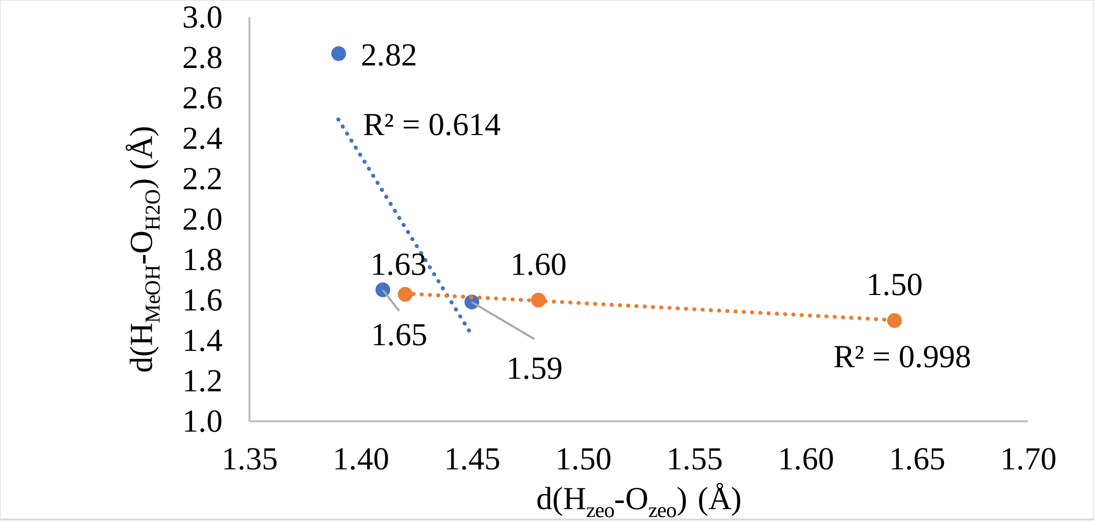

Figure 3.12. Distance between framework proton and oxygen, d(H_{zeo}-O_{zeo}), plotted against distance between the two molecular species in the pore, d(H_{MeOH}-O_{H2O}). Blue data points identify mono-dentate arrangements whereas orange denotes bidentate.

3.3.4. Electronic Parameters Analysis

We calculated the chemical hardness (η), chemical potential (μ), band gaps (δ) and electronegativity (χ) of the empty clusters, given in Table 3.16, with IP (ionisation potential) and EA (electron affinity), presented in Table 3.17.

Table 3.16. Summary of chemical hardness (η), chemical potential (μ), band gaps (δ) and electronegativity (χ) of the empty clusters. All values given in kJ/mol.

	H-Y	H-ZSM-5 [I2]	H-ZSM-5 [Z6]	H-ZSM-5 [M7]
η	-313	-330	-323	-338
μ	-654	-622	-619	-620
δ	627	660	645	676
χ	654	622	619	620

Table 3.17. Summary of HOMO-LUMO energies, ionization potential (IP) and electron affinity (EA) of empty zeolite clusters. All values given in kJ/mol.

H-Y		H-ZSM-5 [I2]		H-ZSM-5 [Z6]		H-ZSM-5 [M7]	
HOMO	LUMO	HOMO	LUMO	HOMO	LUMO	HOMO	LUMO
-967	-340	-951	-292	-941	-296	-958	-282
IP	EA	IP	EA	IP	EA	IP	EA
967	340	951	292	941	296	958	282

Based on Figures 3.13-3.16 plotted below, where we analysed the relationship between chemical hardness or chemical potential and the adsorption energies or distance between the zeolite framework or the Brønsted proton of the single and bi-methanol models, we conclude that there is no correlation between these parameters, which highlights the complexity of the interactions involved and factors taking part in them, further validating the necessity to use state-of-the-art techniques to model them. We limited our analysis to using just the chemical hardness and potential, as the other two parameters (band gap and electronegativity) were proportional to the initially mentioned electronic factors, as can be understood from the methodology.

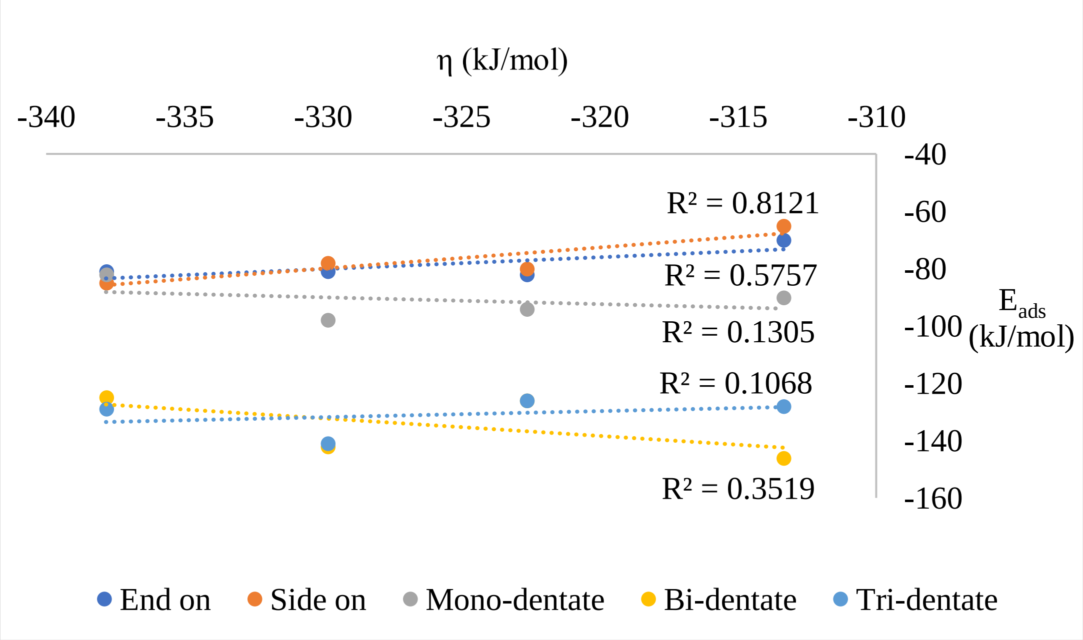

Figure 3.13. Plot between chemical hardness (η) (kJ/mol) of empty cluster and adsorption energy (E_{ads}) (kJ/mol) of single and bi-methanol models.

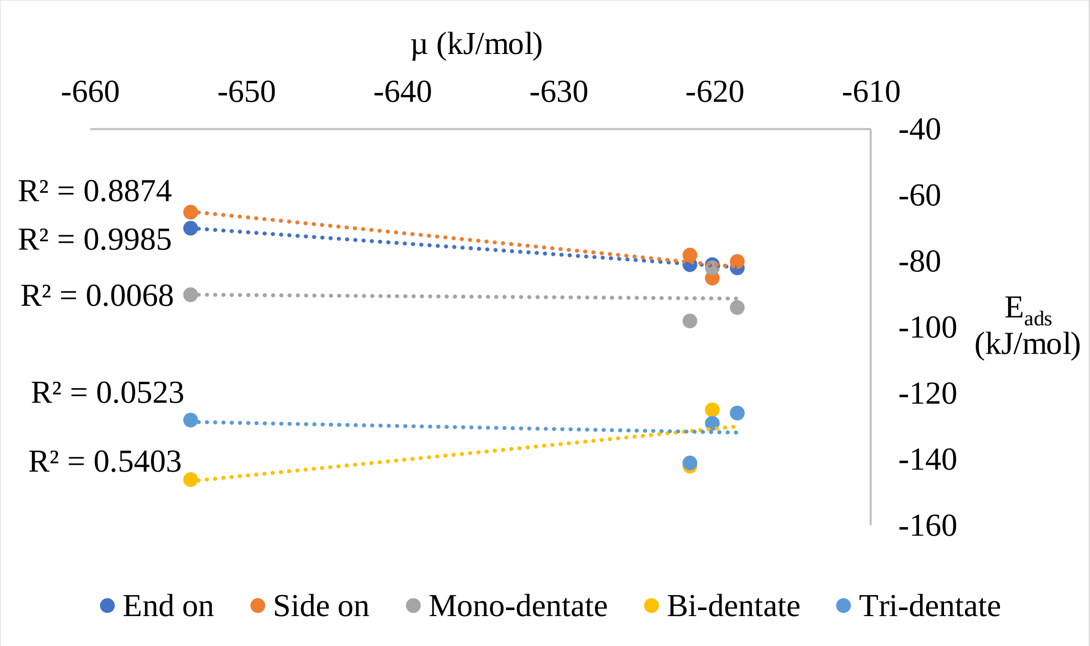

Figure 3.14. Plot between chemical potential (μ) (kJ/mol) of empty cluster and adsorption energy (E_{ads}) (kJ/mol) of single and bi-methanol models.

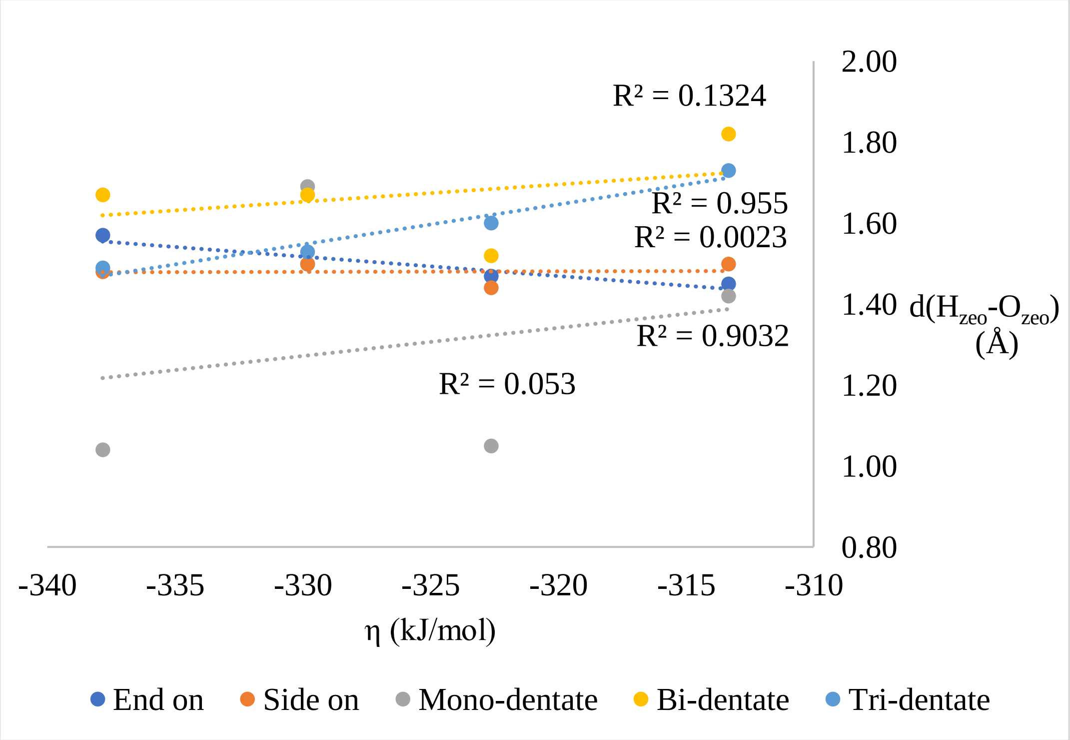

Figure 3.15. Plot between chemical hardness (η) (kJ/mol) of empty cluster and the distance between the zeolite framework and the main adsorbent d(H_{zeo}-O_{zeo}) (Å) of the single and bi-methanol models.

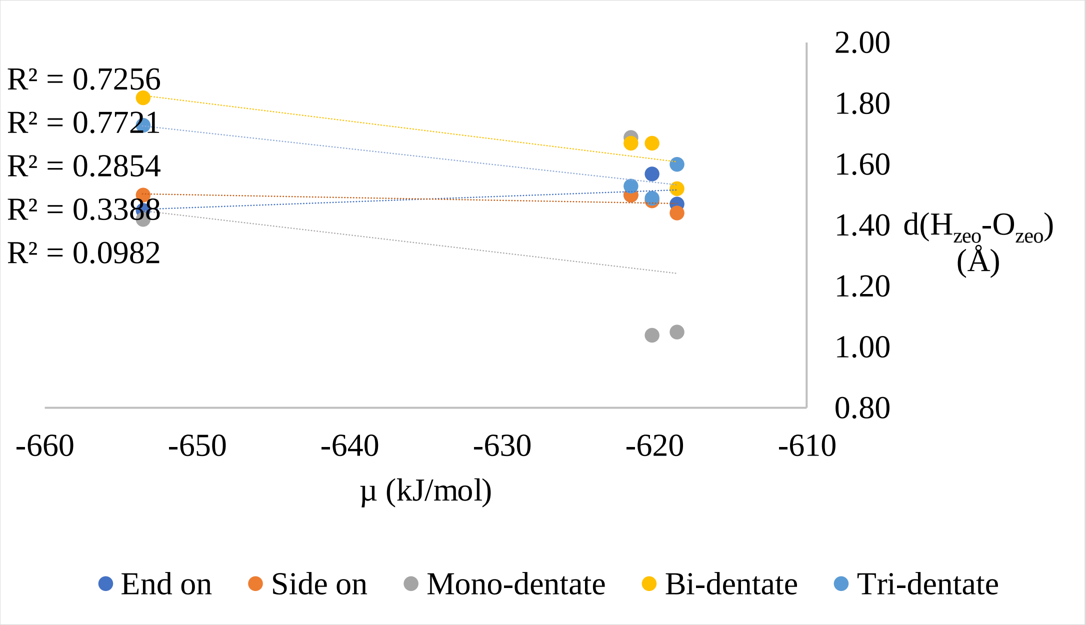

Figure 3.16. Plot between chemical potential (µ) (kJ/mol) of empty cluster and the distance between the zeolite framework and the main adsorbent $d(H_{zeo}\text{-}O_{zeo})$ (Å) of the single and bi-methanol models.

3.3.5. Vibrational analysis of adsorbed methanol

In order to understand further the interactions between sorbates and the zeolite framework, and to allow comparison with experiment, vibrational frequency calculations were performed using the geometries obtained with the B97-3 exchange-correlation functional and a finite-difference harmonic approximation approach. The results, presented in Table 3.17, show that the vibrational frequency of the O_{zeo}-H_{zeo} stretch mode decreases from 3706 cm^{-1} for the empty framework to 2244 (2498) cm^{-1} when the CH_3OH is adsorbed End-on (side-on) in the H-Y framework. This redshift is indicative of weaker bonding of the O-H Brønsted site, i.e. the framework proton is not bound as strongly, and even less so upon adsorbing methanol in the End-on configuration. Comparing the vibrational frequencies for the End-on and Side-on models, there is a difference of ~ 150 cm^{-1} for H-Y, which relates to stronger framework-methanol interactions in the former. This difference between End-on and

Side-on is also observed for H-ZSM-5 with the exception of H-ZSM-5 [M7], where the End-on vibrational frequencies are higher than Side-on; which has been highlighted and discussed in Section 3.3.1, with the Side on methanol noted as rotating to End on. Throughout, the vibrational frequency of the OH bond of the CH_3OH remains constant at ~ 3900 cm^{-1}.

Table 3.17. Vibrational frequencies of O-H bonds in H-Y, H-ZSM-5 and CH_3OH (cm^{-1}) when considering adsorption of one and two methanol species at the active site. The parent structure of the identified atoms is given in subscript after the atomic label as either zeolite (zeo) or methanol (MeOH).

	H-Y	H-ZSM-5		
		[I2]	[Z6]	[M7]
	O_{zeo}-H_{zeo}			
Empty zeolite	3789	3836	3805	3873
Experiment[6] *(in presence of CH_3OH)*	*2440*			
Simulations[61,33] *(in presence of CH_3OH)*	*2548-3235*			
Side-on	2498	2581	2504	2725
End-on	2244	2504	2331	2803
	H_{zeo}-O_{MeOH}-H_{MeOH} bending			
Experiment[62,63,57]	*1600-1800*			
Simulations[33,64,50]	*1635-1687*			
Mono-dentate	1778	1734	*	*
Bi-dentate	1736	1799	1803	1847
Tri-dentate	1786	1764	1721	1802
	Asymmetric H_{zeo}-O_{MeOH}-H_{MeOH} stretch			
Experiment[62,63,57]	*2400-2600*			
Simulations[33,64,50]	*2023-2548*			
Mono-dentate	2143	2718	*	*
Bi-dentate	1848	2376	2624	2183
Tri-dentate	2635	2685	2632	2509
	Symmetric H_{zeo}-O_{MeOH}-H_{MeOH} stretch			
Experiment[62,63,57]	*2700-3100*			
Simulations[33,64,50]	*2549-2900*			
Mono-dentate	3039	3037	*	*
Bi-dentate	3098	3082	2786	3078
Tri-dentate	2822	2841	2829	3086

* Values not reported as methyloxonium ion is not formed in these models

Agreement with previous experimental and computational work is established not only in the case of a single CH_3OH adsorption[6,51] but also for the bi-methanol models; additional vibrational motions appear when adding the second CH_3OH, which is attributed to a protonated CH_3OH. Specifically, the resulting H-O-H bending (or scissoring) and the symmetric and asymmetric O-H stretches of the H-O-H^+ group vibrational modes, with the movements displayed in Figure 3.17.

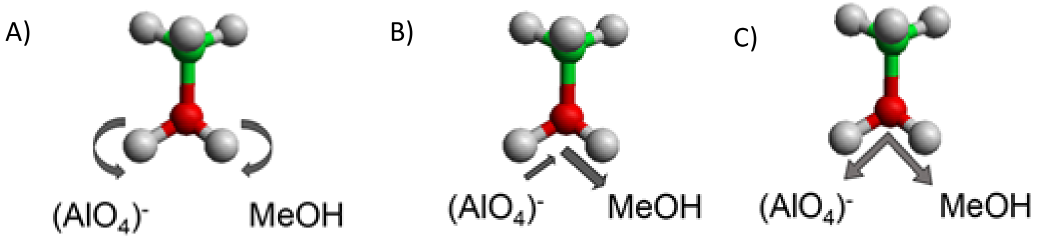

Figure 3.17. Vibrational modes of the H-O-H group of the methyloxonium molecule, specifically A) H-O-H bending, B) O-H asymmetric stretch, C) O-H symmetric stretch. Atom movements are indicated with grey arrows.

The H-O-H^+ bending motion depends simultaneously on the interaction between the zeolite framework and the co-adsorbed methanol molecule, both mono- and bi-dentate CH_3OH configurations give vibrational frequencies that decrease with increasing adsorption strength (Figure 3.18).

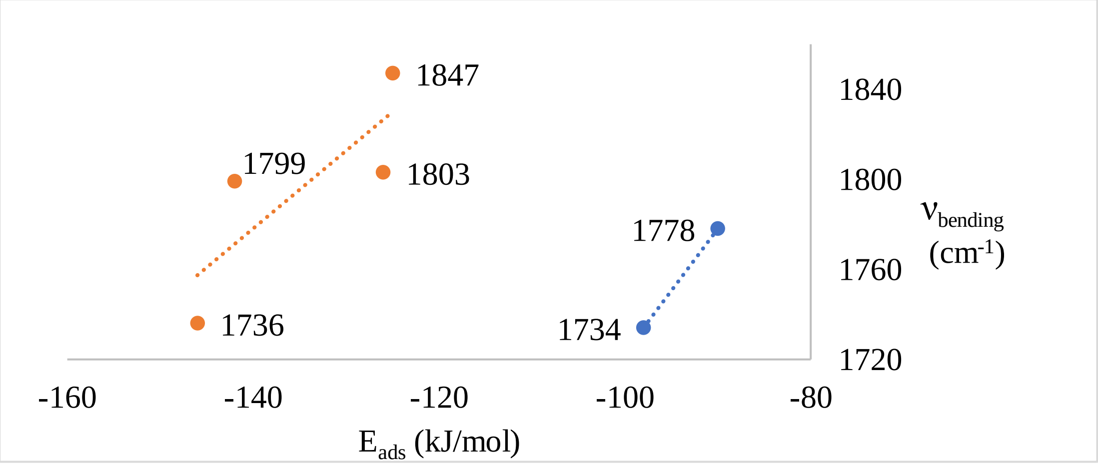

Figure 3.18. Plot between the adsorption energy of the two methanol molecules E_{ads} (kJ/mol) of bi-methanol system and H-O-H^+ bending vibrational frequency ($\nu_{bending}$, cm^{-1}).

The proximity to the zeolite framework and second methanol molecule also is seen to influence shifts in the asymmetric and symmetric O-H stretches. In particular, the O-H asymmetric stretch depends inversely on how close the methyloxonium is to the second CH_3OH; and the O-H symmetric stretch depends on the distance between the zeolite framework and the -OH^+ moiety of the $CH_3OH_2^+$, with greater distance leading to lower frequencies (Figure 3.19 and 3.20).

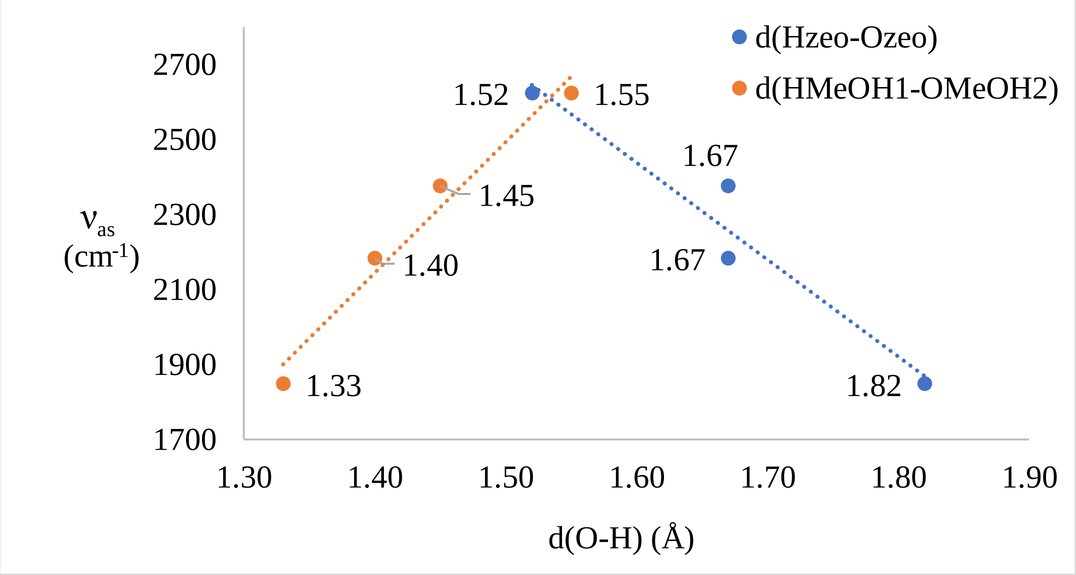

Figure 19. Distance d(O-H), representing the distance between the two methanol molecules (d(H_{MeOH1}-O_{MeOH2}), orange line) and the distance between the zeolite framework and the main adsorbent (d(H_{zeo}-O_{zeo}), blue line), plotted against the asymmetric O-H stretch vibrational frequency (ν_{as}, cm^{-1}).

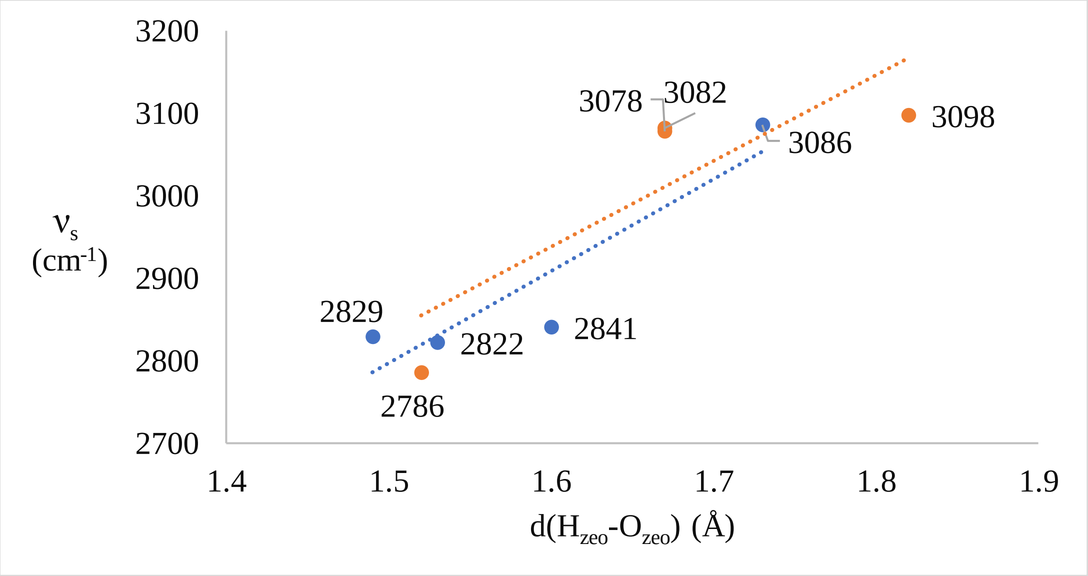

Figure 3.20. Plot between distance between the zeolite framework and the main adsorbent d(H_{zeo}-O_{zeo}) (Å) and O-H symmetric stretch vibrational frequency (ν_s, cm^{-1}).

The behaviour outlined for the vibrational frequencies of the asymmetric and symmetric O-H stretch were also observed experimentally[57], with an increase in methanol feed leading to an increase and decrease in their respective signature frequencies. These shifts, we suggest, correspond to the methyloxonium being part of a bigger and more stable methanol cluster, which would need to be positioned either in larger pores, or outside of the zeolite framework, due to the requirement of a greater number of methanol-methanol interactions. As highlighted by our results, the changes in the stretching vibrational frequencies can be attributed to the bi-dentate models, which we postulate indicates that the bi-dentate configuration is observed in the previously mentioned experimental study. Furthermore, in the case of the CH_3 vibrational frequencies, no significant difference is observed between the single and bi-methanol models or between each of the mono, bi or tri-dentate calculations that we have performed. Values range from 3076-3276 cm^{-1} in the single methanol adsorbed models and 3066-3349 cm^{-1} in the bi-methanol cases, which is in agreement with other experimental[57] and theoretical studies[65]. This result indicates that the CH_3 moiety is unperturbed during framework interactions, though more work is necessary to correlate further any outcomes from framework methoxylation with changes in vibrational frequencies.

3.4. Summary and Conclusions

Species relevant to the methanol to hydrocarbons (MTH) process, as represented by methanol, water and methane, have been studied interacting with zeolite catalysts H-Y and H-ZSM-5 using a hybrid QM/MM approach. The H-ZSM-5 framework stabilizes a single methanol in either a Side-on or End-on geometry, with channels (M7, Z6) preferable over the open intersection sites (I2) and the alternative H-Y framework. For bi-methanol models, the more open H-Y and H-ZSM-5 intersection (I2) have a local-environment that facilitates the stabilization of multiple molecules, when compared to channels. Bi-methanol adsorption was considered in mono-, bi- and tri-dentate arrangements, with the hydroxyl ring formed by a "bi-dentate" configuration being most stable. Polarising hydrogen bonds formed between the -OH groups of the molecules, have a more significant influence on the adsorption energetics than the less polarising hydrogen bonds formed through -CH_3 moieties. The orientation and polarity of molecules at the active site are suggested as being a driving force for spontaneous proton transfer from the framework onto an adsorbed methanol, as justified by spontaneous proton transfer occurring in our calculations with multiple methanol molecules and when water is introduced, but not when methane is introduced. Vibrational frequency calculations allow us to clarify further that the methyloxonium ($CH_3OH_2^+$), as formed via a bi-dentate adsorption complex, is also present in previous experiment and thus forms a key component of the initiation of the MTH process.

The work presented in this chapter has been published in the following paper:

S. A. F. Nastase; A. J. O'Malley; C. R. A. Catlow; A. J. Logsdail; *Phys. Chem. Chem. Phys.*, **2019**, *21*, 2639-2650.

References:

1 J. Finn, P. E. H. Nielsen and P. M. D. Sørensen, *Biom Conv Bioref*, 2011, **1**, 85–90.
2 I. Dahl and S. Kolboe, *J Catal*, 1994, **149**, 458–464.
3 S. Etemadi and U. Olsbye, in *Master's Thesis - Catalytic investigations of zeolite based methanol to hydrocarbons catalysts*, 2015, pp. 75–122.
4 A. J. O'Malley, S. F. Parker, A. Chutia, M. R. Farrow, I. P. Silverwood, V. García-Sakai and C. R. A. Catlow, *Chem. Commun.*, 2016, **52**, 2897–2900.
5 A. J. O'Malley, A. J. Logsdail, A. A. Sokol and C. R. A. Catlow, *Faraday Discuss.*, 2016, **188**, 235–255.
6 G. Mirth, J. A. Lercher, M. W. Anderson and J. Klinowski, *J Chem Soc Faraday Trans*, 1990, **86**, 3039.
7 N. Govind, J. Andzelm, K. Reindel and G. Fitzgerald, 2002, 423–434.
8 S. Suwardiyanto, R. F. Howe, E. K. Gibson, C. R. A. Catlow, A. Hameed, J. McGregor, P. Collier, S. F. Parker and D. Lennon, *Faraday Discuss.*, 2017, **197**, 447–471.
9 S. M. Campbell, X. Z. Jiang and R. F. Howe, *Micro Meso Mat*, 1999, **29**, 91–108.
10 S. K. Matam, R. F. Howe, A. Thetford and R. C. A. Catlow, *Chem. Commun.*, 2018, **54**, 12875-12878.
11 G. Artioli, C. Lamberti and G. L. Marra, *Acta Crystallographica Section B Structural Science*, 2000, **56**, 2–10.
12 A. K. C. J.A. Hriljac, M. M. Eddy, J. A. Donohue, G. J. Ray, *Journal of Solid State Chemistry*, 1993, **106**, 66–72.
13 G. Sastre, V. Fornes and A. Corma, *J Phys Chem B*, 2002, **106**, 701–708.
14 A. Ghorbanpour, J. D. Rimer and L. C. Grabow, *Catal Comm*, 2014, **52**, 98–102.
15 T. W. Keal and D. J. Tozer, *J Chem Phys*, 2005, **123**, 121103.
16 M. F. Guest, I. J. Bush, H. J. Van Dam, P. Sherwood, J. M. H. Thomas, J. H. Van Lenthe, R. W. Havenith and J. Kendrick, *Molec Phys*, 2005, **103**, 719–747.
17 S. Grimme, *Journal of Computational Chemistry*, 2006, **27**, 1787–1799.
18 M. Valiev, E. J. Bylaska, N. Govind, K. Kowalski, T. P. Straatsma, H. J. J. Van Dam, D. Wang, J. Nieplocha, E. Apra, T. L. Windus and W. A. De Jong, *Comp Phys Com*, 2010, **181**, 1477–1489.
19 R. Ahlrichs and P. R. Taylor, *J. Chim. Phys*, 1981, **78**, 315–324.
20 D. R. Hartree, *Mathematical Proceedings of the Cambridge Philosophical Society*, 1928, **24**, 426.
21 V. Fock, *Zeitschrift fur Physik*, 1930, **61**, 126–148.
22 W. Smith, C. W. Yong and P. M. Rodger, *Molecular Simulation*, 2002, **28**, 37–41.
23 J. R. Hill and J. Sauer, *The J Phys Chem*, 1994, **98**, 1238–1244.
24 J.-R. Hill and J. Sauer, *The J Phys Chem*, 1995, **99**, 9536–9550.
25 P. Sherwood, A. H. . De Vries, S. J. Collins, S. P. Greatbanks, N. A. Burton, M. A. Vincent and I. H. Hillier, *Faraday Discuss*, 1997, **106**, 79–92.
26 S. Metz, J. Kästner, A. A. Sokol, T. W. Keal and P. Sherwood, *Wiley Inter Rev: Comp Molec Sci*, 2014, **4**, 101–110.
27 C. G. Broyden, *Math Comp*, 1970, **24**, 365–365.
28 R. Fletcher, *Comp J*, 1970, **13**, 317–322.
29 D. Goldfarb, *Math Comp*, 1970, **24**, 23–23.
30 D. F. Shanno, *Math Comp*, 1970, **24**, 647–647.

31 W. C. Swope, H. C. Andersen, P. H. Berens and K. R. Wilson, *J Chem Phys*, 1982, **76**, 637–649.

32 J. Kästner, J. M. Carr, T. W. Keal, W. Thiel, A. Wander and P. Sherwood, *J Phys Chem A*, 2009, **113**, 11856–11865.

33 F. Haase and J. Sauer, *JACS*, 1995, **117**, 3780–3789.

34 J. Kotrla, D. Nachtigallova, L. Kubelková, L. Heeribout, C. Doremieux-Morin and J. Fraissard, *J Phys Chem B*, 1998, **102**, 2454–2463.

35 A. Goodrow and A. T. Bell, *J Phys Chem C*, 2008, **112**, 13204–13214.

36 K. Hemelsoet, A. Ghysels, D. Mores, K. De Wispelaere, V. Van Speybroeck, B. M. Weckhuysen and M. Waroquier, *Cat Tod*, 2011, **177**, 12–24.

37 F. B. van Duijneveldt, J. G. C. M. van D. van de Rijdt and J. H. van Lenthe, *Chem Rev*, 1994, **94**, 1873–1885.

38 J.-P. Julien, J. Maruani, D. Mayou and G. Delgado-Barrio, *Rec Adv Th Chem Phys Sys*, 2006, **9**, 159–177.

39 S. Hamel, P. Duffy, M. E. Casida and D. R. Salahub, *J Elec Spec Rel Phen*, 2002, **123**, 345–363.

40 P. Politzer and F. Abu-Awwad, *Theor Chem Acc*, 1998, **99**, 83–87.

41 S. Svelle, C. Tuma, X. Rozanska, T. Kerber and J. Sauer, *JACS*, 2009, **131**, 816–825.

42 T. Omojola, N. Cherkasov, A. I. McNab, D. B. Lukyanov, J. A. Anderson, E. V. Rebrov and A. C. van Veen, *Catal Let*, 2018, **148**, 474–488.

43 C. G. Pope, *J Chem Soc Faraday Trans*, 1993, **89**, 1139–1141.

44 C.-C. Lee, R. J. Gorte and W. E. Farneth, *The J Phys Chem B*, 1997, **101**, 3811–3817.

45 U. Olsbye, S. Svelle, M. Bjrgen, P. Beato, T. V. W. Janssens, F. Joensen, S. Bordiga and K. P. Lillerud, *Angew Chem - Int Ed*, 2012, **51**, 5810–5831.

46 S. R. Blaszkowski and R. A. van Santen, *J Phys Chem*, 1995, **99**, 11728–11738.

47 S. R. Blaszkowski and R. A. Van Santen, *JACS*, 1996, **118**, 5152–5153.

48 J. D. Gale, C. R. a. Catlow and J. R. Carruthers, *Chem Phys Let*, 1993, **216**, 155–161.

49 S. R. Blaszkowski and R. A. van Santen, *The J Phys Chem*, 1995, **99**, 11728–11738.

50 I. Štich, J. D. Gale, K. Terakura and M. C. Payne, *JACS*, 1999, **121**, 3292–3302.

51 D. F. Plant, A. Simperler and R. G. Bell, *J Phys Chem B*, 2006, **110**, 6170–6178.

52 Y. Gu, T. Kar and S. Scheiner, *JACS*, 1999, **121**, 9411–9422.

53 K. C. Kumara Swamy, S. Kumaraswamy and P. Kommana, *JACS*, 2001, **123**, 12642–12649.

54 J. D. Gale, R. Shah, M. C. Payne, I. Stich and K. Terakura, *Cat Tod*, 1999, **50**, 525–532.

55 H. Koller, G. Engelhardt and R. A. van Santen, *Top Catal*, 1999, **9**, 163–180.

56 M. Hunger and T. Horvath, *JACS*, 1996, **118**, 12302–12308.

57 A. Zecchina, S. Bordiga, G. Spoto, D. Scarano, G. Spanò and F. Geobaldo, *J Chem Soc - Faraday Trans*, 1996, **92**, 4863–4875.

58 M. W. Anderson, P. J. Barrie and J. Klinowski, *J. Phys. Chem*, 1991, **95**, 235–239.

59 K. De Wispelaere, C. S. Wondergem, B. Ensing, K. Hemelsoet, E. J. Meijer, B. M. Weckhuysen, V. Van Speybroeck and J. Ruiz-Martínez, *ACS Catal*, 2016, **6**, 1991–2002.

60 A. Hwang, M. Kumar, J. D. Rimer and A. Bhan, *J Catal*, 2017, **346**, 154–160.

61 R. Shah, J. D. Gale and M. C. Payne, *J Phys Chem*, 1996, **100**, 11688–11697.

62 S. G. Izmailova, I. V. Karetina, S. S. Khvoshchev and M. A. Shubaeva, *J Col Inter Sci*, 1994, **165**, 318–324.
63 R. von Ballmons, J. B. Higgins and M. M. J. Treacy, *Proc Ninth Int Zeo Conf*, 1993, **2**, 255.
64 C. M. Nguyen, M. F. Reyniers and G. B. Marin, *Phys ChemChem Phys*, 2010, **12**, 9481–9493.
65 E. Nusterer, P. E. Blöchl and K. Schwarz, *Angew Chem Int Ed*, 1996, **35**, 175–177.

Chapter 4. Acid site configuration analysis within the MTH process using AIMD simulations

In this chapter, we provide by means of first principle molecular dynamics simulations mechanistic insight into framework methylation under these theoretical conditions. The molecular dynamics simulations show that stable methanol clusters form in the zeolite pores, and these clusters commonly deprotonate the active site. Enhanced sampling molecular dynamics simulations give evidence that the barrier for framework methylation is significantly affected by the neighbourhood of an additional acid site, suggesting that cooperative effects influence reactivity. The insights obtained here are important to optimally design the catalyst and the conditions in order to tune the induction period.

4.1. Introduction

First principle simulation techniques are a valuable tool to obtain mechanistic insight into elementary reaction steps. Such an approach allows us to obtain a better understanding of experimental data. Early studies of the MTH process modelled methylation with static methods on small cluster (i.e. molecular) models of the zeolitic frameworks, which neglected the role of the broader structure on the stability of the transition state[1,2]. Later reports suggested that confinement effects of the zeolite lowered the methylation barrier by 40 kJ/mol[3]. Furthermore, it is crucial to explore the free energy surface at the temperature of interest. Recently enhanced sampling molecular dynamics methods have been successfully used within the context of zeolite catalyzed reactions.[4,5] For example, the metadynamics enhanced sampling approach has been used to analyse the role of methanol loading on the methylation of H-ZSM-5 at high temperatures (623 K), and the energy barrier was observed as being lower (139 ±2 kJ/mol) than in previous static simulations (154 kJ/mol)[4].

Th work reported in this chapter aims to give more mechanistic insight into the effects of both higher methanol loadings and a higher acid site density on the methylation reaction at room temperature within ZSM-5. To this end, we use *ab initio* molecular dynamics at conditions which mimic as far as possible the experiment under which the low-temperature methylation was observed within H-ZSM-5. The metadynamics method is used to investigate how far the clustering of methanol molecules around the active site leads to activation and formation of a methoxylated framework at room temperature. Our methodology is outlined below, after which, in the results, we consider specifically the dynamics of the methanol molecules and their interaction with the Brønsted acid sites in the zeolite catalyst. The enhanced sampling molecular dynamics simulations are used to study explicitly the methylation step with different methanol loadings and acid site densities.

4.2. Methodology

4.2.1 Catalyst model

Our models for the H-ZSM-5 catalyst are, as previously, constructed by replacing a tetrahedrally coordinated Si atom (T-site) in the MFI parent crystal structure with an Al atom. In order to isolate and quantify properly the interactions that occur between active sites and reactants, we modelled zeolite unit cells having one or two acid sites each, corresponding to a Si/Al ratio of 95 and 47, respectively. This model does not match exactly the experimental conditions (Si/Al =30, corresponding to ~3 acid sites per unit cell) but allows us to characterize accurately the effects of acid site isolation and interaction. MFI has 12 symmetry inequivalent tetrahedra (T-) sites: for the single acid site model, the Al substituents are considered in the T12 so as to be at the intersection site of the sinusoidal and straight channels in MFI; and, for the two acid sites model, Al is positioned in the T12 and T8 positions, thus being three T-sites apart[3]. In principle, their positions are arbitrary, but it is commonly assumed that some positions are more favourable than others[6]. The choice of those particular sites satisfies Loewenstein's rule[7] and allows testing of the viability for the "pairing" of sites, as is proposed in previous experimental studies[8]. For all Al substitutions, charge-compensating hydrogen atoms are added on adjacent oxygens, with the Brønsted proton facing towards the centre of the supercage, i.e. representing a configuration we propose to be involved in catalyzed reactions.

To incorporate the methanol molecules into our models, we evenly distributed one, three or five methanol molecules in the main pore of the zeolite unit cell. To ensure that the choice of methanol loading is realistic, we employed a thermodynamic mean field model[9,10] to estimate the loading based on the pore volume, guest and interaction strength, and it was found that a maximum of 14 methanol molecules per acid site are able to adsorb, with details available in Section 4.2.2. The maximum loading considered (5 methanol per unit cell) is slightly less than experimental conditions (7 methanol molecules per acid site), but proves sufficient in our explicit dynamics simulations in order to observe the effect of clustering on reactivity.

Ab initio molecular dynamics (MD) simulations, as presented in Section 2.2 were performed on the combined system, using 3-dimensional periodic boundary conditions, with the CP2K simulation package (version 6.1)[11]. The dynamics of the nuclei were governed by the Newtonian equations of motion, in which the potential from the Born–Oppenheimer electronic ground state is inserted. The self-consistent field (SCF) energy was evaluated with DFT using the revPBE functional[12] (discussed in Section 2.1.2.1.1) with Grimme D3 dispersion corrections[13] (Section 2.1.2.1.2) and the Gaussian Plane Waves method[14] that uses Gaussians as basis sets (DZVP–GTH[15]) (Section 2.1.2.3) and planewaves (320 Ry cut-off) (Section 2.1.2.4) as auxiliary basis. The SCF convergence criterion was set to an energy change of less than 1×10^{-5} Hartrees between SCF iterations. In both NPT and NVT simulations, presented in Sections 2.2.1.2.1 and 2.2.1.2.2, respectively, the integration time step was set to 0.5 fs. The initial geometry for the NVT simulations was taken as the final snapshot of the NPT calibration models, with methanol inserted into the zeolite pores. The cell parameters, presented in Table 4.1, were determined from a preliminary isothermal-isobaric (NPT) ensemble simulation of 50 ps on the empty zeolite cells (of both one and two acid sites per unit cell), where the number of atoms, temperature (300 K) and external pressure (1 atm) are controlled by controlled by a chain of five Nosé-Hoover thermostats[16,17] and pressure by the Martina-Tobias-Klein barostat[18].

Table 4.1. Cell parameters of NPT simulations specific to the Si/Al ratio of simulation models (top two rows), given in Å and °, compared to experimental values (bottom row).

Si/Al	a (Å)	b (Å)	c (Å)	α (°)	β (°)	γ (°)
95	20.05	19.85	13.38	90.87	90.42	90.28
95*	20.09	19.92	13.40	90.02	90.01	90.11
47	20.05	19.84	13.43	91.16	89.80	89.92
299[57]	20.02	19.90	13.38	90.00	90.00	90.00

** Parameters used for MD simulation at 670 K of 5 methanol molecules per one acid site unit cell.*

The NPT simulations were considered to be equilibrated after the variation of a series of parameters reached a steady state. Specifically, the average value of the zeolite unit cell volume plateaued and the instantaneous values of the temperature, kinetic and potential energies displayed a periodic variation, as shown in Figure 4.1.

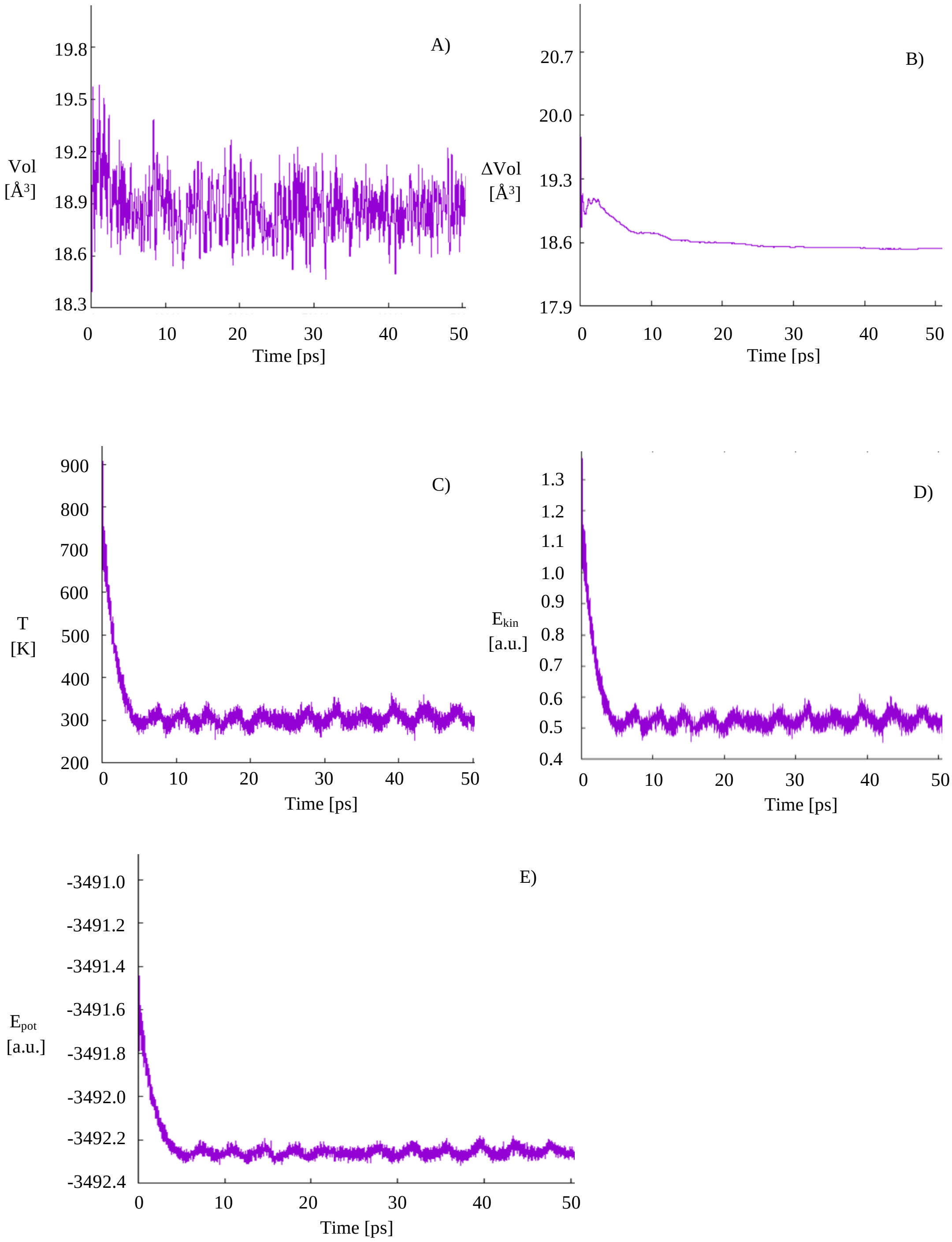

Figure 4.1. Plot of NPT simulation time with A) instantaneous volume and B) average volume of zeolite unit cell, presented in angstroms cubed [Å^3], C) instantaneous temperature, given in Kelvin [K], D) instantaneous kinetic and E) potential energies, provided in atomic units [a.u.], of one methanol per single acid site unit cell model.

To ensure a rigorous description of the adsorbed states, MD "production runs" were performed in the NVT ensemble, with the volume fixed to that from the NPT equilibration (of the corresponding empty zeolite calibrations with one or two acid sites per unit cell), for a simulated run time limited to 50 ps, leading to a total of 100 ps simulation time (50 ps NPT equilibration and 50 ps NVT for the "production run").

4.2.2 Structural analysis

Methanol loading per pore volume analysis

The Zeo++ package[19] was used to evaluate the available space within the H-ZSM-5 framework that could accommodate guest molecules (Figure 4.2). This analysis includes both channels and intersections within the zeolite framework.

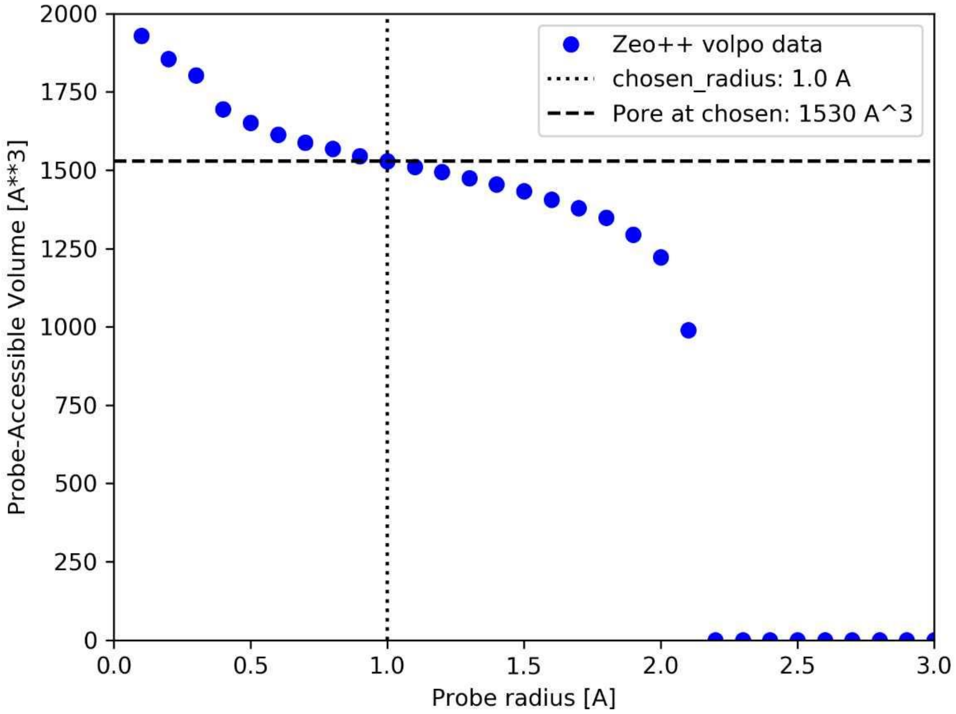

Figure 4.2. Plot of the accessible space within the entire zeolite unit cell of ZSM-5 against guest molecule radius, given in Å^3 and Å, respectively, determined with the Zeo++ package[19].

We approximate the radius of a methanol molecule as 1 Å, allowing us to estimate the number of methanol molecules that can be inserted in the zeolite model.

Considering the adsorption energy of a single methanol molecule within the zeolite, which falls between -90 and -115 kJ/mol in previous studies, one can evaluate the loading of the pore with methanol (Figure 4.3). Based on the plot in Figure 4.3, we can deduce that due to the relatively large adsorption energy of methanol to the Brønsted acid site results in a high saturation being feasible, with up to 13 methanol molecules around one active site. High quantity of methanol coordinating with one acid site is also observed experimentally[20].

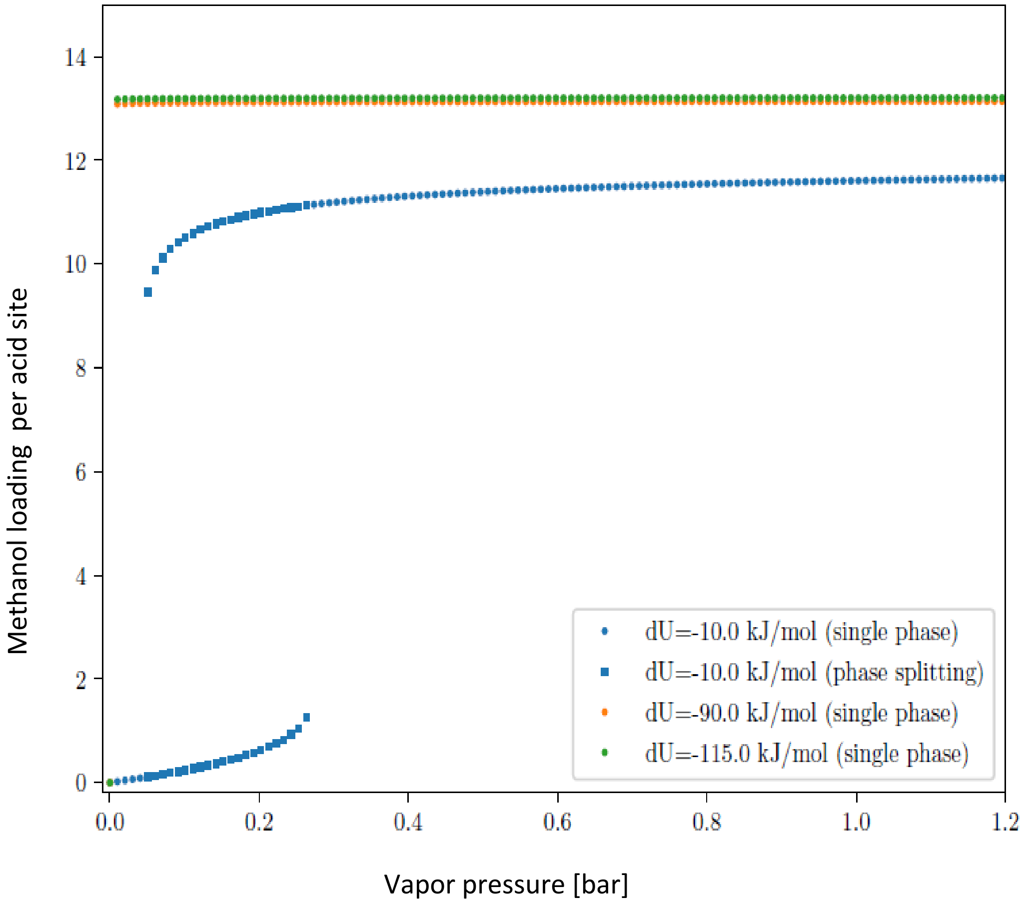

Figure 4.3. Methanol loading per acid site as a function of the methanol vapor pressure. A key is provided based on the adsorption energy per methanol molecule, presented in kJ/mol, determined with the geometry based tool implemented in Zeo++ package[19].

Geometric analysis

To understand and quantify the geometric features of our simulations, we measured a range of bond lengths in snapshots from the molecular dynamics trajectories (Figure 4.4). This analysis was conducted on trajectory snapshots taken every 1 fs of the 50 ps NVT “production runs”, from which then the average distances were determined.

Figure 4.4. Schematic representation of parameters used for Structural Analysis alongside the CVs employed in Metadynamics simulations. The analysed intra- and inter-molecular distances are between: hydrogen and nearest methanol oxygen, $d(O_{M1\text{-}5}\text{-}H_{M1\text{-}6})$*; methanol oxygen atoms,* $d(O_{M1}\text{-}O_{M5})$*; and carbon atoms,* $d(C_{M1\text{-}5})$*, where indices denote the parent methanol cluster of the atom of interest.*

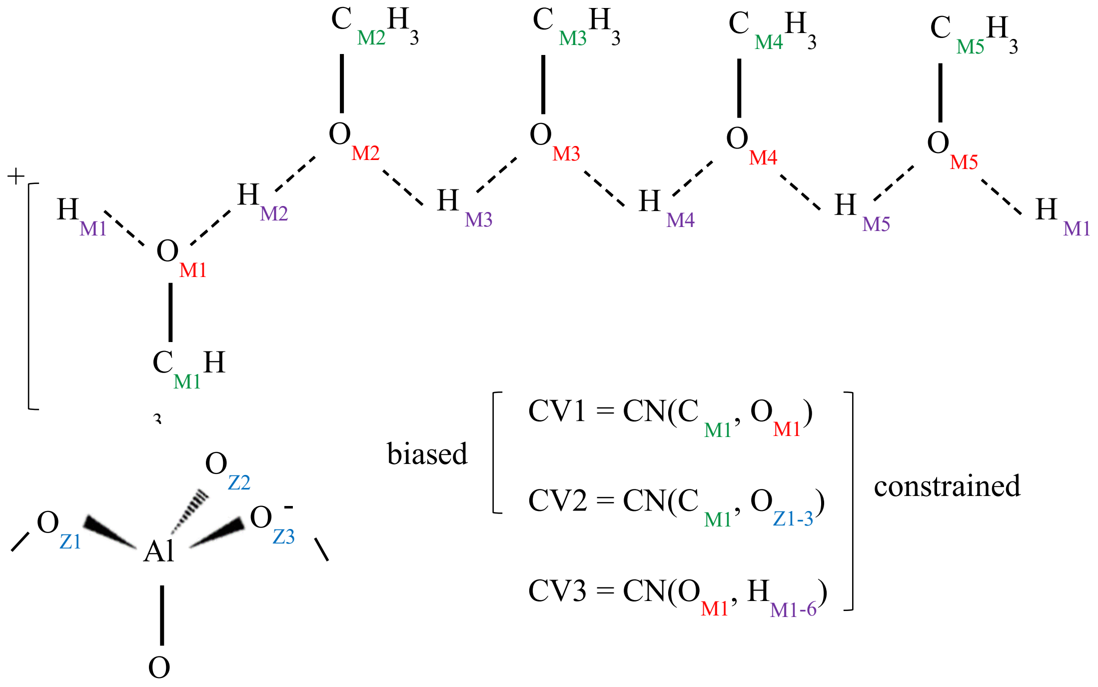

Additionally, a more in-depth approach was taken to determine the stability of the methanol cluster around the active site. As illustrated in Figure 4.5, the distance is calculated between the geometrical centre for the oxygen atoms in the clustered methanol molecules ($O_{M1\text{-}5}$) and geometric centre for the three oxygen atoms exposed to the methanol cluster at the active site (A). When a second acid site is considered, we quantify the polarization effects and overall influence of the two acid sites by determining the distance between the centre of the smallest zeolite ring that contains the two aluminium atoms (R), with the geometric circle being described by the geometric centre of the composing silicon and aluminium atoms, and the centre of the methanol cluster (Figure 4.5).

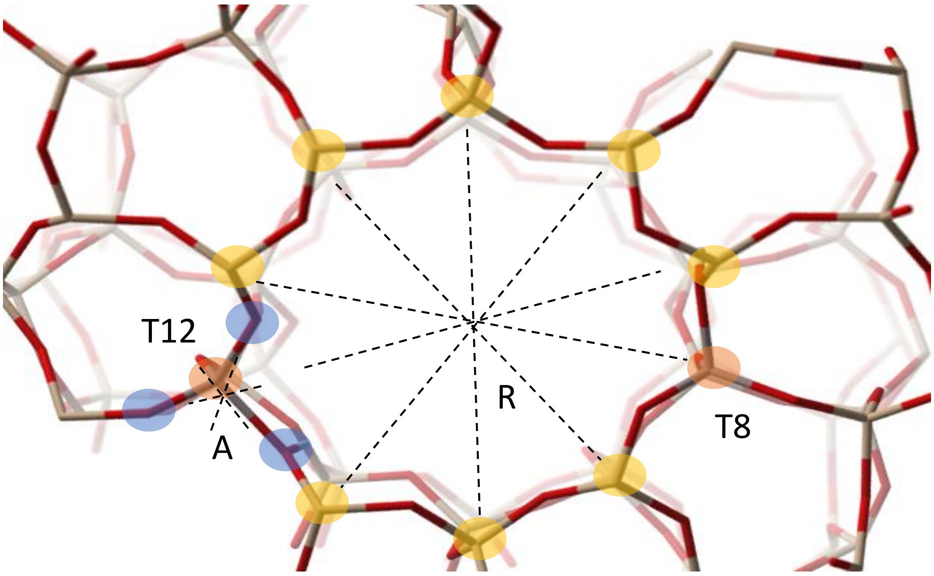

Figure 4.5. Distances are measured between the centre of the active site (A), and the centre of the aluminium ring (R), with Al - light brown, Si - yellow, O - red, H - white.

Protonation effects

We determined the distance between the Brønsted proton, co-adsorbates and zeolite sites by measuring the length of the O-H bonds in the methanol cluster, allowing us to conduct a statistical analysis of protonation effects. Specifically, the probability of the zeolite site being deprotonated, and the Brønsted proton being transferred on to a methanol, is calculated as a percentage of time in the production run where the O-H bond length between Brønsted proton and methanol oxygen is less than or equal to 1.2 Å. We also analysed the position of the Brønsted proton in the methanol cluster by determining the percentage of time in the production run where a methanol would simultaneously have two O-H bonds less or equal to 1.2 Å.

Clustering probability

The distance between the neighbouring methanol, $d(O_M\text{-}O_M)$, was used to quantify the probability of methanol clustering, by setting a distance threshold of equal to or less than 3.5 Å. This distance was decided from a review of all the data and assignments related to the H-donating and H accepting pair of methanol. We note that, based on the minimum and maximum distances tabulated in Tables 4.2 and 4.3, particularly the $d(O_M\text{-}O_M)$ lengths, we can conclude that the methanol molecules do not change position significantly in the methanol clusters, which might have otherwise hindered our analysis.

Table 4.2. Minimum, average and maximum intermolecular distances, d, between methanol molecules of interest throughout the NVT simulations. In particular, we present distances between methyl groups (C_M-C_M), oxygen atoms of methanol molecules (O_M-O_M). Schematic representation of the analysed intermolecular distances given in Figure 4.4. Distances are given in Å.

Methanol/cell		3 MeOH		5 MeOH				
Si/Al ratio		95	47	95	47			
$d(C_{M1}$-$C_{M2})$	min.	3.18	3.31	3.46	3.64	-	-	-
	ave.	4.38	4.25	4.47	4.52			
	max.	4.96	5.05	5.43	5.08	-	-	-
$d(C_{M2}$-$C_{M3})$	min.	3.25	3.24	3.32	2.81	-	-	-
	ave.	4.27	4.28	4.10	3.40			
	max.	5.17	5.48	4.87	4.06	-	-	-
$d(C_{M3}$-$C_{M4})$	min.	-	-	3.14	-	-	-	-
	ave.			4.45				
	max.	-	-	5.69	-	-	-	-
$d(C_{M4}$-$C_{M5})$	min.	-	-	2.93	-	-	-	-
	ave.			3.87				
	max.	-	-	4.96	-	-	-	-
Methanol/cell		1 MeOH			3 MeOH		5 MeOH	
Si/Al ratio		95	47	47*	95	47	95	47
$d(O_{M1}$-$O_{M2})$	min.	-	-	-	2.25	2.25	2.28	2.26
	ave.				2.45	2.51	2.60	2.47
	max.	-	-	-	2.94	3.27	3.17	2.99
$d(O_{M2}$-$O_{M3})$	min.	-	-	-	2.29	2.27	2.25	2.29
	ave.				2.59	2.53	2.47	2.59
	max.	-	-	-	3.15	3.43	2.89	3.20
$d(O_{M3}$-$O_{M4})$	min.	-	-	-	-	-	2.26	-
	ave.						2.56	
	max.	-	-	-	-	-	3.16	-
$d(O_{M4}$-$O_{M5})$	min.	-	-	-	-	-	2.34	-
	ave.						2.83	
	max.	-	-	-	-	-	3.55	-

"-" no results to present

*Results of methanol adsorbed on T8 acid site instead of T12.

Table 4.3. Minimum and maximum intermolecular hydrogen bond distances, d(O_M-H), in methanol molecules of interest (Å), taken over from our NVT simulations. Schematic representation of the analysed intermolecular distances given in Figure 4.4.

Methanol/cell		1 MeOH			3 MeOH		5 MeOH	
Si/Al ratio		95	47	47*	95	47	95	47
d(H_{M1}-O_{M1})	min.	0.95	0.90	0.90	0.90	0.90	0.88	0.90
	max.	1.91	1.77	1.75	1.35	1.28	1.21	1.36
d(O_{M1}-H_{M2})	min.	-	-	-	0.96	0.94	0.97	0.93
	max.	-	-	-	1.99	2.56	2.35	2.21
d(H_{M2}-O_{M2})	min.	-	-	-	0.94	0.93	0.92	0.91
	max.	-	-	-	1.79	1.75	1.59	1.90
d(O_{M2}-H_{M3})	min.	-	-	-	0.91	0.93	0.93	0.91
	max.	-	-	-	1.56	1.72	2.01	1.53
d(H_{M3}-O_{M3})	min.	-	-	-	1.03	0.99	0.93	1.00
	max.	-	-	-	2.23	2.66	1.83	2.33
d(H_{M3}-O_{M4})	min.	-	-	-	0.85	0.90	0.92	0.82
	max.	-	-	-	1.25	1.20	1.63	1.29
d(H_{M4}-O_{M4})	min.	-	-	-	-	-	0.94	-
	max.	-	-	-	-	-	2.51	-
d(O_{M4}-H_{M5})	min.	-	-	-	-	-	0.87	-
	max.	-	-	-	-	-	1.35	-
d(H_{M5}-O_{M5})	min.	-	-	-	-	-	1.14	-
	max.	-	-	-	-	-	3.05	-
d(O_{M5}-H_{M6})	min.	-	-	-	-	-	0.81	-
	max.	-	-	-	-	-	1.29	-

“-” no results to present
*Results of methanol adsorbed on T8 acid site instead of T12.

4.2.3 Metadynamics

To accelerate the sampling of the activated transition from methanol to methoxide, the metadynamics (MTD) approach was employed[21,22,23] using the CP2K software (version 6.1)[11], further detailed in Section 2.2.2. The MTD simulations were performed in the canonical (NVT) ensemble at 300 K. The cell parameters (Table 4) and initial geometry were again taken from NPT equilibration simulations, with appropriate methanol loading also included in the equilibration[5]. The NPT equilibrations were run multiple times to validate that the methanol molecules cluster around the Brønsted acid site. For one acid site per unit cell, the three or five methanol molecules included form either a trimer and a pentamer cluster, respectively, around the acid site. For two acid sites per unit cell, due to the cooperative effect of the active sites, the methanol molecules were observed to split between the acid sites: With three methanol molecules, monomers, dimers and trimers were observed; when five methanol molecules were included per unit cell, combinations of trimers and dimers were observed (Figure 4.6).

Table 4.4. Average unit cell parameters observed during NPT simulations with methanol loaded into the unit cell. These parameters were subsequently used for metadynamics simulations. Lattice vectors and angles are given in Å and °, respectively.

Si/Al	Methanol/cell	a (Å)	b (Å)	c (Å)	α (°)	β (°)	γ (°)
95	1 MeOH	20.05	19.79	13.41	91.24	90.63	90.24
47		20.04	19.86	13.39	90.90	90.59	90.30
95	3 MeOH	19.96	19.80	13.27	90.14	90.20	90.35
47		20.03	19.84	13.38	90.91	89.89	90.15
95	5 MeOH	20.02	19.81	13.38	91.03	90.36	90.20
47		20.05	19.82	13.38	91.13	90.14	90.15

In order to describe the Free Energy Surface (FES) of the methylation pathway, we employed parameters that previously gave accurate results[4,5,24] for similar MTD simulations of methylation in H-ZSM-5. Specifically, during the NVT MTD run, two geometric parameters selected to uniquely describe each reaction state, also named collective variables (CVs), will be biased by adding Gaussian hills every 25 fs along the two CVs, defined by coordination numbers (CN): [4]

$$\mathrm{CN}(i,j) = \sum i,j \; \frac{1-\left(r_{ij} \,/\, r_0\right)^n}{1-\left(r_{ij} \,/\, r_0\right)^m} \qquad (4.1)$$

in which r_{ij} is the distance between bonded atoms i and j. The parameters n and m were set to 6 and 12, respectively. The reference distance, r_0, was chosen to be similar to the transition state distance between atoms i and j (2.0 Å). The first CV, CV1, is defined by CN(C_{MeOH}-O_{MeOH}), which describes the breaking of the C-O bond of the methanol; CV2 is then defined by CN(C_{MeOH}-$O_{zeolite}$) to describe the subsequent formation of the C-O bond between the resulting methyl moiety and the zeolite framework. The definition of the collective variables is illustrated schematically in Figure 4.4. The width of the Gaussian hills is set to 0.02, and the height is initially 5.0 kJ/mol. Once the transition state has been identified and crossed twice, the height of the Gaussian hills is halved in order to more accurately sample the activation barrier; this process is repeated until a final hill height of 0.65 kJ/mol is used, thus ensuring a refined representation of the energy surface. To ensure we sample chemically relevant space with the metadynamics simulations, we use constraints to keep the reactant and product molecules in the vicinity of the acid site. In particular, we constrain the C-O bonds represented by CV1 and CV2 to the reaction transition state by using a series of single-sided energy “walls”, that extend from the barrier (B) towards smaller values of the collective variable (CV), represented by a quadratic potential $K(CV-B)^2$, with K - quadratic potential constant: for CV1, this barrier is at CN(C_{MeOH}-O_{MeOH}) = 0.04 (K=50 Ha), which corresponds to a bond distance of 3.4 Å; and for CV2, the barrier is at CN(C_{MeOH}-$O_{zeolite}$) = 0.03 (K=200 Ha). In addition, to keep the reactant methanol protonated, which we observe as an active part of the reaction mechanism when more than one methanol is adsorbed on the active site, we applied a quadratic wall in position 0.056 of CV3 (K=100 Ha), which corresponds to an average O-H stretch of 1.25 Å and a maximum elongation from the the methanol of 2 Å; this parameter choice is based on the average O-H bond lengths observed for the protonated methanol in our NPT simulations (Table 4.5).

Table 4.5. Average O-H distance observed for the protonated methanol in our NPT equilibration calculations. Values are given in Å.

Si/Al	Methanol/cell	d(O-H)
95	3 MeOH	1.24
47		1.13
95	5 MeOH	1.19
47		1.16

An overview of all the simulated models and figures are presented in Table 4.6 and Figure 4.7.

The metadynamics simulations were deemed complete when a change in the free energy barrier was equal or less than 5 kJ/mol between every 500 energy hills added, with the reported errors determined from the minimum and maximum barriers calculated at this point. In order to determine accurately the free energy at the reaction coordinate q, we take the difference between the bias potentials calculated for CV1 and CV2 (q_1 and q_2, respectively) as $q = q_1 - q_2$, and project them on the difference of the CVs (diagonal) to create a 1D profile for the free energy, $F(q)$:[10]

$$F(q) = -\frac{1}{\beta}.\ln\left\{C \int_{-\infty}^{+\infty} \exp[-\beta F(q_1, q_1 + q)]\, dq_1\right\} \tag{4.2}$$

with $\beta = (1/k_BT)$, where k_B is the Boltzmann constant and T is the simulation temperature. C is a factor normally introduced to ensure a normalised relationship between the dimensions of $F(q)$ and $F(q_1, q_1 + q)$, which in this work is set to unity as both variables have the same dimensions; this does not influence the energy differences between states.[10] We then determine the minimum energy path free energy barrier (ΔF), representing the difference between the transition state and the highest minimum energy of the reactant state, as:

$$\Delta F = F(q^*) + k_B T.\ln\left(\frac{k_B T \bar{Z}_R}{hA}\right) \tag{4.3}$$

Here, $F(q^*)$ represents the free energy of the transition state q^*, which is relative to the energy minimum in the reactant “valley”; $\bar{Z}_R$ is proportional to the partition function of the reactant “valley”, and hence accounts for the broadness of the energy well; h is Planck’s constant; and A is a factor related to rate of change of the collective variable in the transition state and was computed by the procedure proposed by Bučko *et al*[9]. The ΔF was then used to calculate the methylation reaction rate (k) as follows:

$$\mathrm{k} = A\left(\frac{e^{-\beta F(q*)}}{\bar{Z}\mathrm{R}}\right) \tag{4.4}$$

Further details on the methodology and case studies are provided in the Bailleul *et al* study[10].

Table 4.6. Overview of models employed for MD and MTD simulations, with methanol and Si/Al ration presented alongside simulation time given in picoseconds (ps) and meta-picoseconds (m-ps)

MD. NPT*			MD. NVT		
Si/Al	Methanol loading	time [ps]	Si/Al	Methanol loading	time [ps]
95	1	50	95	1	50
95	3	50	95	3	50
95	5	50	95	5	50
47	1	50	47	1	50
47	3	50	47*	3	50
47	5	50	47	5	50
Metadynamics					
Si/Al	Methanol loading	time [m-ps]			
95	1	277			
95	3	231			
95	5	213			
47	1	223			
47	3	184			
47	5	196			

** Two MD, NPT runs were simulated in parallel for each model, to ensure a proper sampling process occurred.*

** Two distinct configurations were simulated for the MD, NVT 3 methanol, 2 acid sites per unit cell models.*

To validate our method and parameters for the metadynamics simulations themselves, multiple simulations were conducted to obtain accurate parameters. To perform this validation, the unit cell chosen was a zeolite model containing three methanol molecules and one acid site. With respect to the refinement of the energy landscape and the Gaussian “hills” added when sampling, it was concluded that a “hill” height of 0.65 kJ/mol was adequate; subsequent refinement with energy hills of 0.30 kJ/mol and 0.10 kJ/mol, both of which were performed for 25 ps (corresponding to 500 energy hills added for each energy “layer”) did not give a statistically significant change in the MEP free energy barrier (Table 4.7).

Table 4.7. MEP free energy barriers calculated from metadynamics simulation with two collective variables biased - MTD (CN1, CN2), one collective variable biased (CN1-CN2). Values are presented in kJ/mol.

	“Hill” height:		
	0.65	0.30	0.10
MTD (CN1, CN2)	169	166	165
MTD (CN1 - CN2)	171	-	-

“-“ no results to present

In order to ensure that no different reaction path is taken when employing two CVs, the accuracy behind using two CVs was analysed by conducting a MTD simulation having as biased CV: CN1-CN2 or the difference between the (coordination number of the methyl to the oxygen of the methanol hydroxyl) - CN1 and (the coordination number of the as methyl to the oxygen atoms of the active site) - CN2, as detailed in the Methodology section, as the single collective variable we biased.

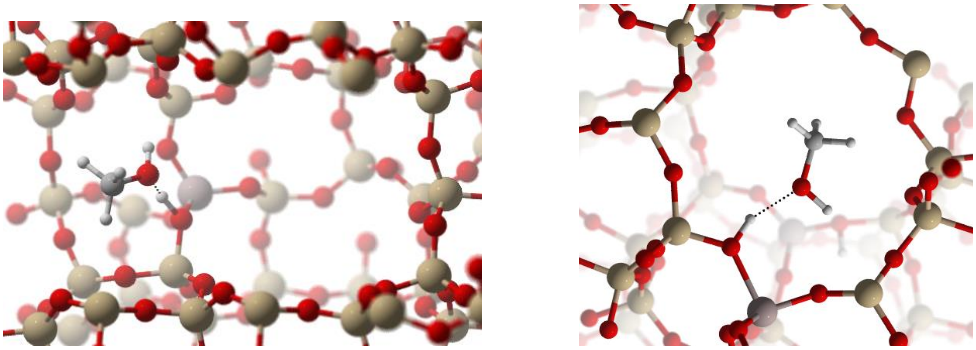

1 MeOH (Si/Al=95)

1 MeOH (Si/Al=47)

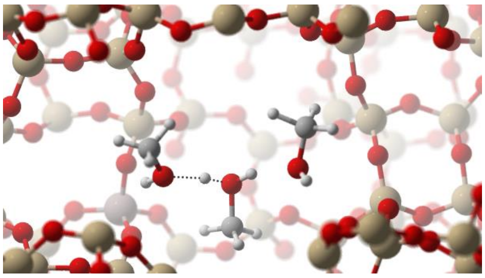

3 MeOH (Si/Al=95)

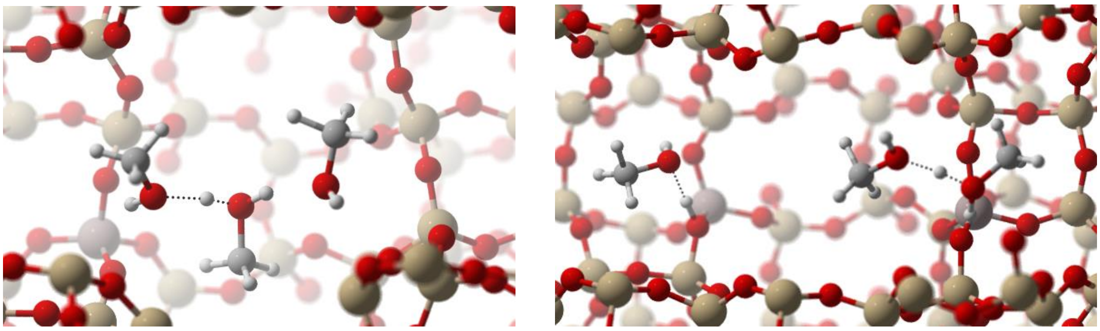

3 MeOH at T12 acid site (Si/Al=47)

3 MeOH spread over
T12 and T8 acid site (Si/Al=47)

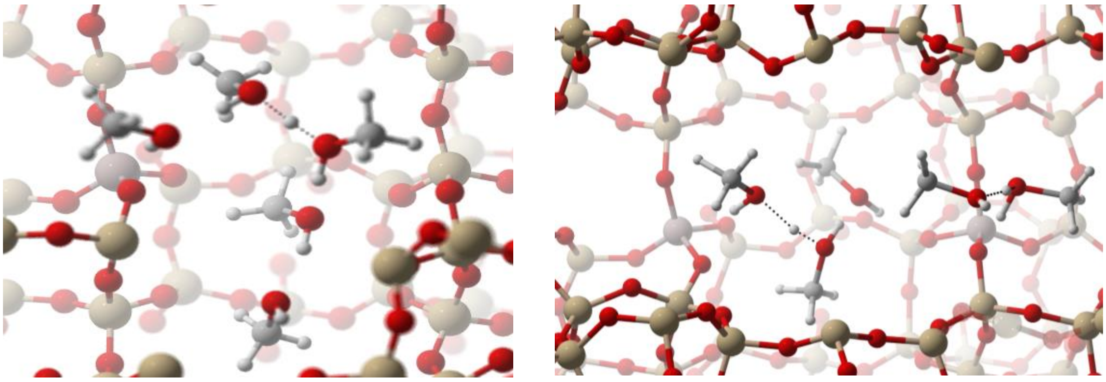

5 MeOH (Si/Al=95)

5 MeOH spread over
T12 and T8 acid site (Si/Al=47)

Figure 4.6. Equilibrated models from NPT simulations prior to applications in metadynamics, with Al - light brown, Si - yellow, O - red, C - grey, H - white.

4.3. Results and discussion

4.3.1 Methanol dynamics at room temperature

For each of the initial models, shown in Figure 4.7, we performed NVT molecular dynamics runs of 50ps, to analyze the adsorption and dynamics behavior of the various methanol loadings. We observe stable, hydrogen-bonded clusters of methanol molecules at each acid site throughout our NVT simulations. Methanol clustering of this nature has been observed previously in simulations and correlated with experimental results[25]; the methanol clusters match with previous IR and calorimetric studies, where up to 11 methanol molecules are reported to adsorb around an active site when the Si/Al ratio is 136[20] and less than 3 methanol molecules are adsorbed at the active site when the Si/Al ratio is 36 or lower, i.e. the zeolite framework has a higher acid site density[20,26].

To evaluate the effect of temperature on the methanol dynamics and to be able to compare with previous theoretical data, MD simulations were performed at two temperatures namely 300 K and 670 K. In our simulations at room temperature, we find that pentamers have the largest probability of forming, whereas in earlier simulations at higher temperatures, trimers were found to be the most stable (Figure 4.8).[5]. For clarity, we performed a separate MD simulation at 670 K with the same approach detailed in Section 2.1, with a loading of 5 methanol per single acid site unit cell, to ensure we could obtain an adequate comparison. At 300 K we see that the hydrogen bonds (Table 4.8) of the 4th (1.51 Å) and 5th methanol (1.90 Å) elongate the further they are from the Brønsted proton, which eventually break once higher thermal effects are employed. It is expected that the size of the hydrogen bonded protonated clusters is determined by a balance between enthalpic stabilization at lower temperatures and entropic factors at higher temperatures.

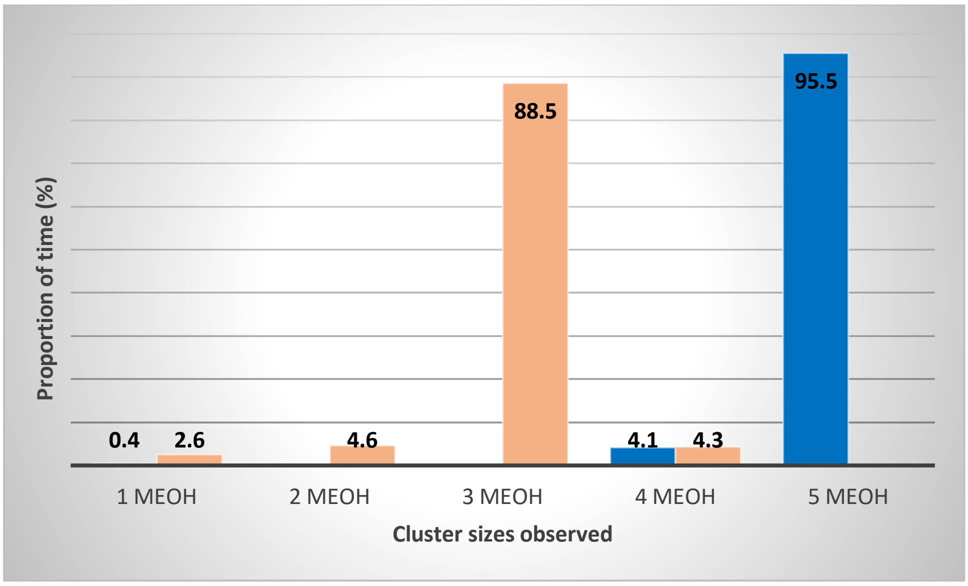

Figure 4.8. Proportion of simulation time for which five methanol molecules (MeOH) were collected in clusters of size one to five molecules. Results are presented for one acid site per unit cell, with the temperature in this work at 300 K (blue) and at 670 K (orange).

During our NVT simulations, models with one methanol adsorbed at the acid site are observed to deprotonate the zeolite framework for ~10% of the overall runtime, as calculated by comparing the distance of the Brønsted proton with the oxygen atoms in the framework and the adsorbed methanol; however, increasing the methanol loading to 3 or 5 molecules per acid site results in deprotonation occurring for ~90% of the overall calculation time, i.e. deprotonation is greatly increased. At these higher methanol loadings, the proton appears to be stabilised (solvated) in the centre of the methanol chain, away from the active site, as concluded by assessing the distance between neighbouring oxygen and hydrogen nuclei in the simulation trajectory, as shown by the data in Tables 4.8 and 4.9. The low probability of deprotonating the zeolite framework with just one methanol molecule may explain the experimental difficulties when evaluating the conditions for activating methanol; specifically, 1 methanol per acid site coverage at ~400 K (Si/Al =30)[27,28,29].

Table 4.8. Average intra- and intermolecular distances between oxygen and hydrogen atoms in the methanol (MeOH) molecules over the entire trajectory run times, presented in Å. All results are from methanol adsorbed on the T12 site with one exception(*), where methanol localised on the alternative T8 acid site. Values that are underlined highlight strongly bound hydrogen nuclei, where the interatomic distance is less than 1.1 Å, and pairs of values highlighted in each row in bold show molecule pairs that form a Zundel configuration, $CH_3OH – H^+ - CH_3OH$. For clarity, the correspondent bonds are represented in Figure 4.7.

MeOH	Si/Al ratio	d(H_{M1}-O_{M1})	d(O_{M1}-H_{M2})	d(H_{M2}-O_{M2})	d(O_{M2}-H_{M3})	d(H_{M3}-O_{M3})
1 MeOH	95	1.36	-	-	-	-
	47	1.34	-	-	-	-
	47*	1.37	-	-	-	-
3 MeOH	95	$\underline{1.01}$	**1.28**	**1.19**	$\underline{1.04}$	1.59
	47	$\underline{1.00}$	**1.40**	**1.13**	$\underline{1.09}$	1.46
5 MeOH	95**	$\underline{1.00}$	1.58	$\underline{1.05}$	**1.27**	**1.21**
	47	$\underline{1.03}$	**1.28**	**1.20**	$\underline{1.04}$	1.58

"-" no results to present, as only one methanol molecule in simulation.
*Results of methanol adsorbed on T8 acid site instead of T12.
**The d(O_{M4}-H_{M4}) and d(O_{M5}-H_{M5}) corresponding to 1,51 Å and 1.90 Å; d(O_{M3}-H_{M4}), d(O_{M4}-H_{M5}) and d(O_{M5}-H_{M6}) lengths of the 5 MeOH model, which are ~ 1Å, have been excluded to limit the length of the table.

Analysing Table 4.8 in detail, we can see that the average distance between the methanol oxygen and framework proton for one methanol per acid site is > 1.3 Å throughout, confirming that the framework tends to not deprotonate; however, for three and five methanol molecules, the same distance, d(H_{M1}-O_{M1}), is reduced below 1.1 Å as the framework proton shifts onto the methanol, forming a methoxonium ($CH_3OH_2^+$) ion stabilised by neighbouring methanol co-adsorbates. Considering the three methanol systems, one can see that a Zundel configuration ($CH_3OH – H_{M2}^+$ -

CH_3OH) occurs,[30] with the hydrogen nuclei H_{M2} not localised to the oxygen in either the first or second methanol, O_{M1} or O_{M2} respectively, but instead on average stabilised equidistant between the two. A similar observation is made for the simulations containing five methanol molecules, though the position of the Zundel configuration in the methanol chain varies depending on the number of acid sites in the simulation.

To validate further these observations, we calculated the proportion of time for which each methanol molecule is protonated into a methoxonium ion, based on analysis of distances between oxygen and hydrogen atoms for the entire simulation trajectory, and the results are presented in Table 4.9.

Table 4.9. Proportion of time (%) that each methanol molecule in the cluster spends as a methoxonium ion during the simulation

		Proportion of time in position in methanol cluster (%)				
Si/Al	Methanol/cell	1	2	3	4	5
95	3 MeOH	31.6	59.3	0.3	-	-
47		15.3	68.5	7.8	-	-
95	5 MeOH	1.6	36.5	48.0	5.2	-
47		34.5	55.6	0.9	-	-

“-” no results to present

The migration of cations from the framework, as we have observed here for a proton in the methanol chain, is a general effect; for methanol in a NaY system, theoretical investigations show that the methanol facilitates migration of the Na^+ from the vicinity of the active site to the centre of the pore, which influences the stability of the methanol cluster.[31] The stability of the solvated cation in the centre of the pore, surrounded by methanol molecules, may be due to a favourable electrostatic environment, as well as the distance of the methanol cluster from the active site hindering the re-transfer of the Brønsted proton from the methanol. Mulliken analysis, which would indicate local electrostatic environment, was inconclusive (Table 4.10) and so further investigation is necessary to validate this hypothesis.

Table 4.10. Mulliken charge analysis calculated for the starting configuration of five MeOH distributed with a H-ZSM-5 model with Si/Al ratio of 95. Calculations were performed with CP2K, using the same settings as described in the methodology section for the NVT production runs. Net electronic charges (e) given for atoms of active site (Al, O) and methanol molecules as detailed in Figure 4.4, with positive values indicating charge depletion.

Atom	Net charge (q)
Al	0.45
O	-0.59
H_{M1}	0.41
O_{M1}	-0.48
H_{M2}	0.35
O_{M2}	-0.41
H_{M3}	0.36
O_{M3}	-0.29
H_{M4}	0.29
O_{M4}	-0.41
H_{M5}	0.29
O_{M5}	-0.48
H_{M6}	0.30

As previously mentioned, we found that a high methanol loading can lead to the formation of methanol clusters that deprotonate the acid site; to further analyse the stability of the methanol molecules at the active site, we determined the distances between the geometric centre of the methanol cluster and framework active site, as described in Section 4.2.2 of the Methodology. Interestingly, the distance frequency analysis (Figure 4.9) shows that the trimer clusters stabilise further from the active site than the pentamer and monomer; we suggest that this effect could be due to the higher methanol loadings of five molecules per active site leading to compression of the methanol molecules in the pore. However, we also note that the same behaviour is not observed for two acid sites per unit cell; instead, the protonated trimer appear repelled by the second (positively charged) Brønsted site, leading to the trimer configuration being closer towards the active site. Similar behaviour is also observed for the pentamer methanol cluster, which is closer towards an active site when there are two acid sites in the zeolite model, though the effects are less pronounced.

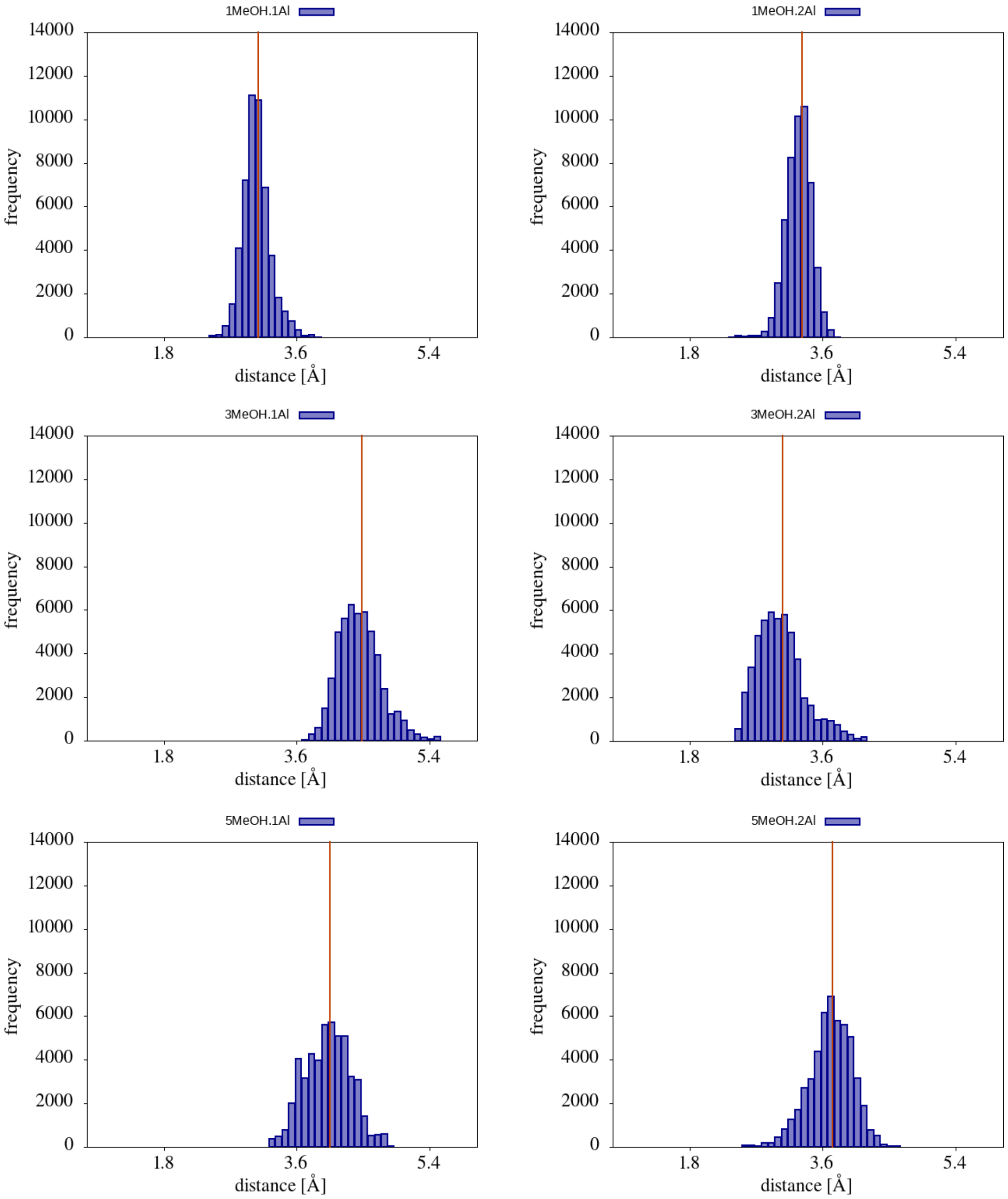

Figure 4.9. Frequency analysis during a 50 ps NVT run of the distance between centre of methanol cluster (M) and the centre of the exposed acid site (A), presented in Å. Models are considered having one (left column) and two (right column) acid sites, with one (top row), three (middle row) and five (bottom row) methanol molecules per unit cell. An orange vertical line highlights the average distance.

The effect of the second acid site on the methanol cluster was further analysed by determining the distance between the methanol cluster and the centre of the zeolite ring that contained the two acid sites, positioned at T12 and T8 in the zeolite, as described in the Methodology Section 4.2.2. When there is only one acid site in the unit cell, the distance between methanol molecules and the centre of the zeolite ring decreases with increasing quantity of methanol molecules (Figure 4.9).

This behaviour is expected, as it becomes more difficult for the methanol to cluster around the single acid site with increased loading, and so the geometric centre shifts towards the centre of the pore. The position of the methanol cluster is less clearly defined when there are two acid sites in the unit cell. For a methanol monomer, the distance between methanol molecules and the centre of the pore increases; considered alongside the behaviour in Figure 4.9, where it is observed that the distance between methanol monomer and the acid site also increases. The increase in distance implies that the molecule interacts with both acid sites. For a methanol trimer, the mean distance between the centre of the methanol cluster and the centre of the zeolite ring remains constant, though with a great variance especially towards high distances, which is in keeping with the observations in Figure 4.9. Finally, for pentamers in a system with two acid sites, a bimodal distribution is observed with distances of ~2.4 Å and ~3.8 Å prominent, which are significantly greater than the average of 1.8 Å observed for the simulations with five methanol in a system with a single acid site. In addition to the above, the time dependent variation of the distance between the methanol cluster and the centre of the zeolite ring, provided in Figure 4.10 and 4.11, also highlights a sudden change in the position of the methanol cluster with respect to the centre of the ring when an additional acid site is present, which contributes to the bimodal appearance observed in Figure 4.12 for five methanol molecules.

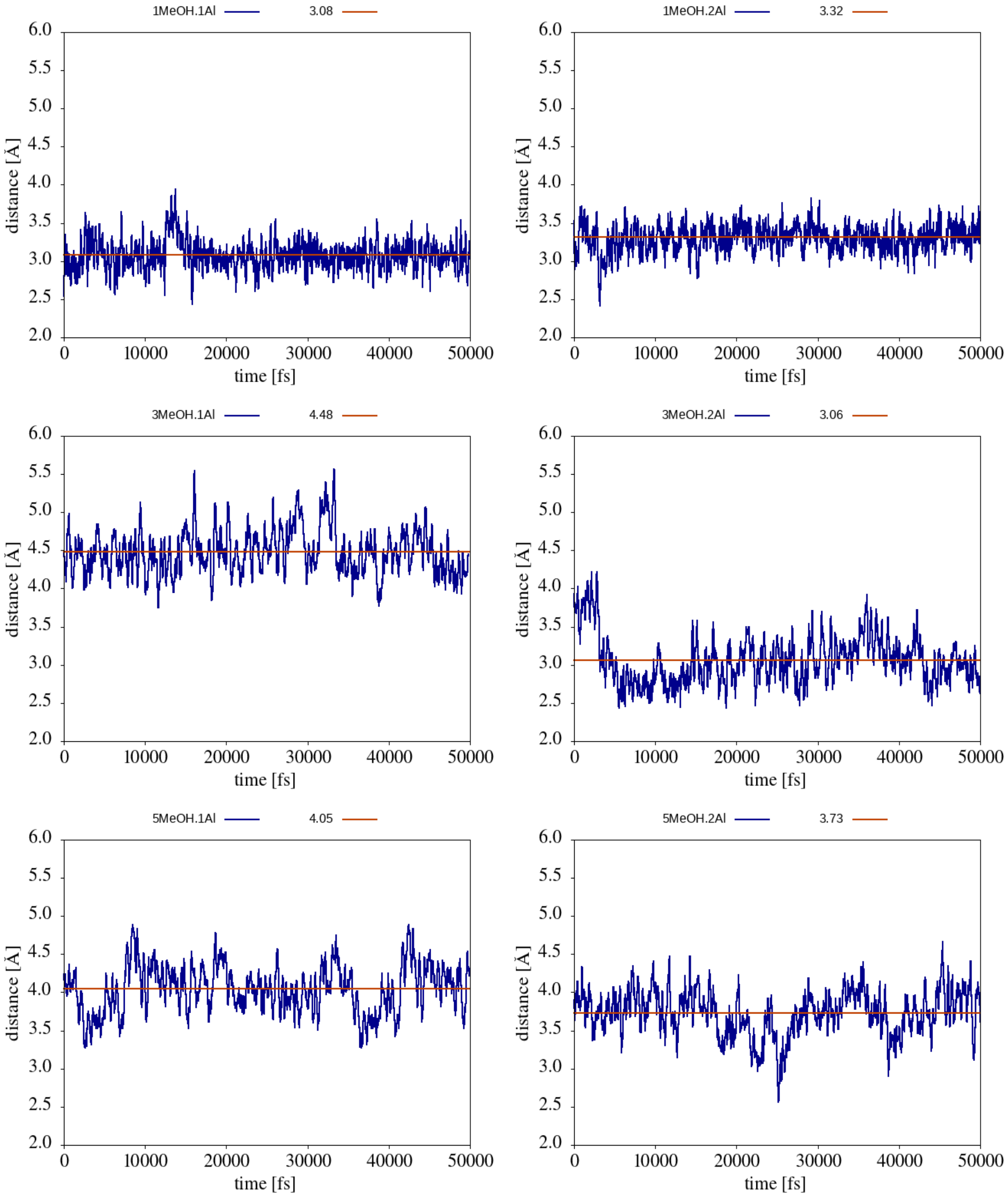

Figure 4.10. Variation of M-A distance (Å) as a function of simulation time (fs) for a 50 ps NVT simulation. Data is presented for one (top row) and two (bottom row) acid sites, with one (left column), three (middle column) and five (right column) methanol molecules per unit. The orange horizontal line highlights the average distance.

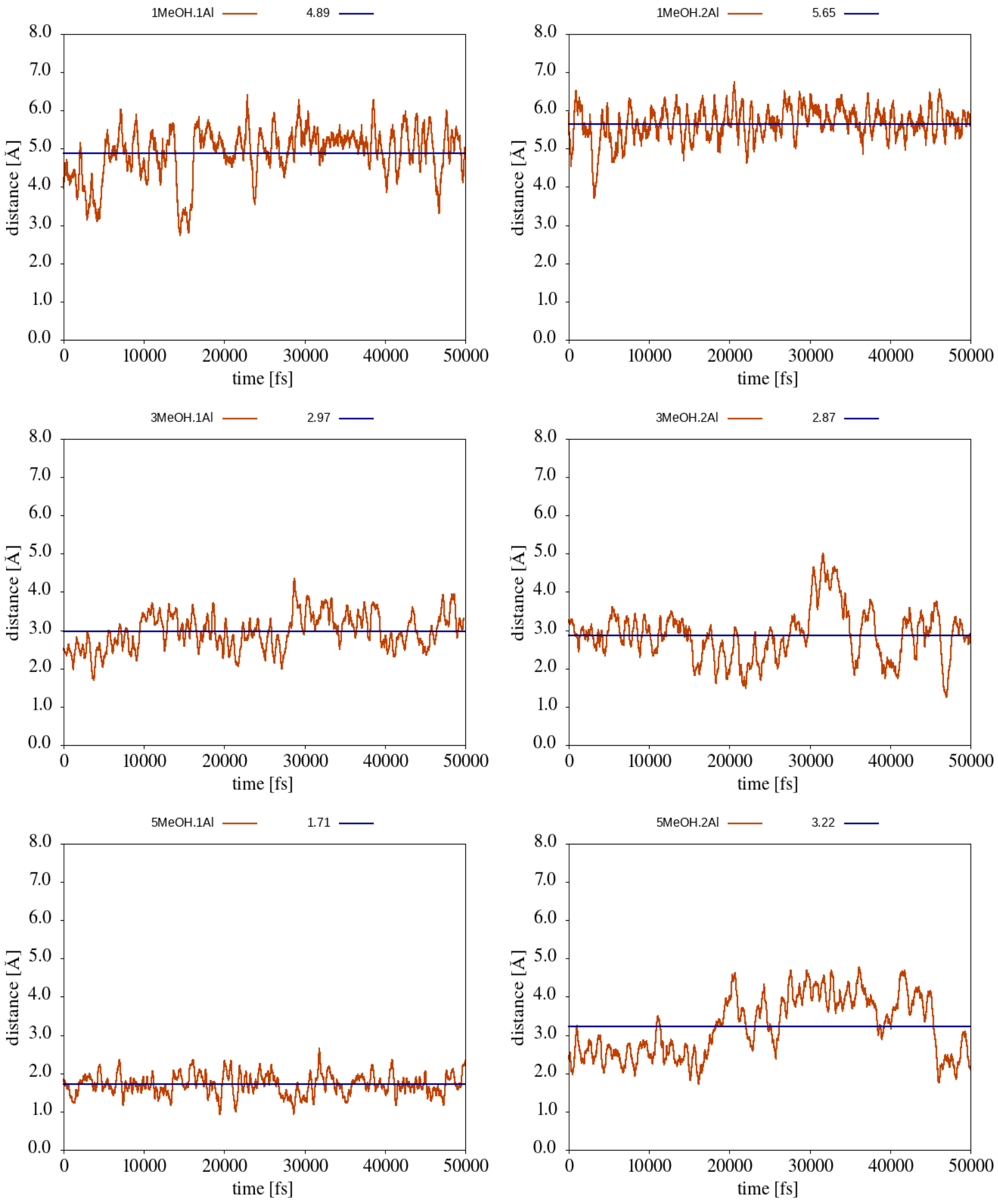

Figure 4.11. Variation of M-R distance (Å) as a function of simulation time (fs) in a 50 ps NVT simulation. Data is presented for one (top row) and two (bottom row) acid sites, with one (left column), three (middle column) and five (right column) methanol molecules per unit cell. A blue horizontal line highlights the average distance.

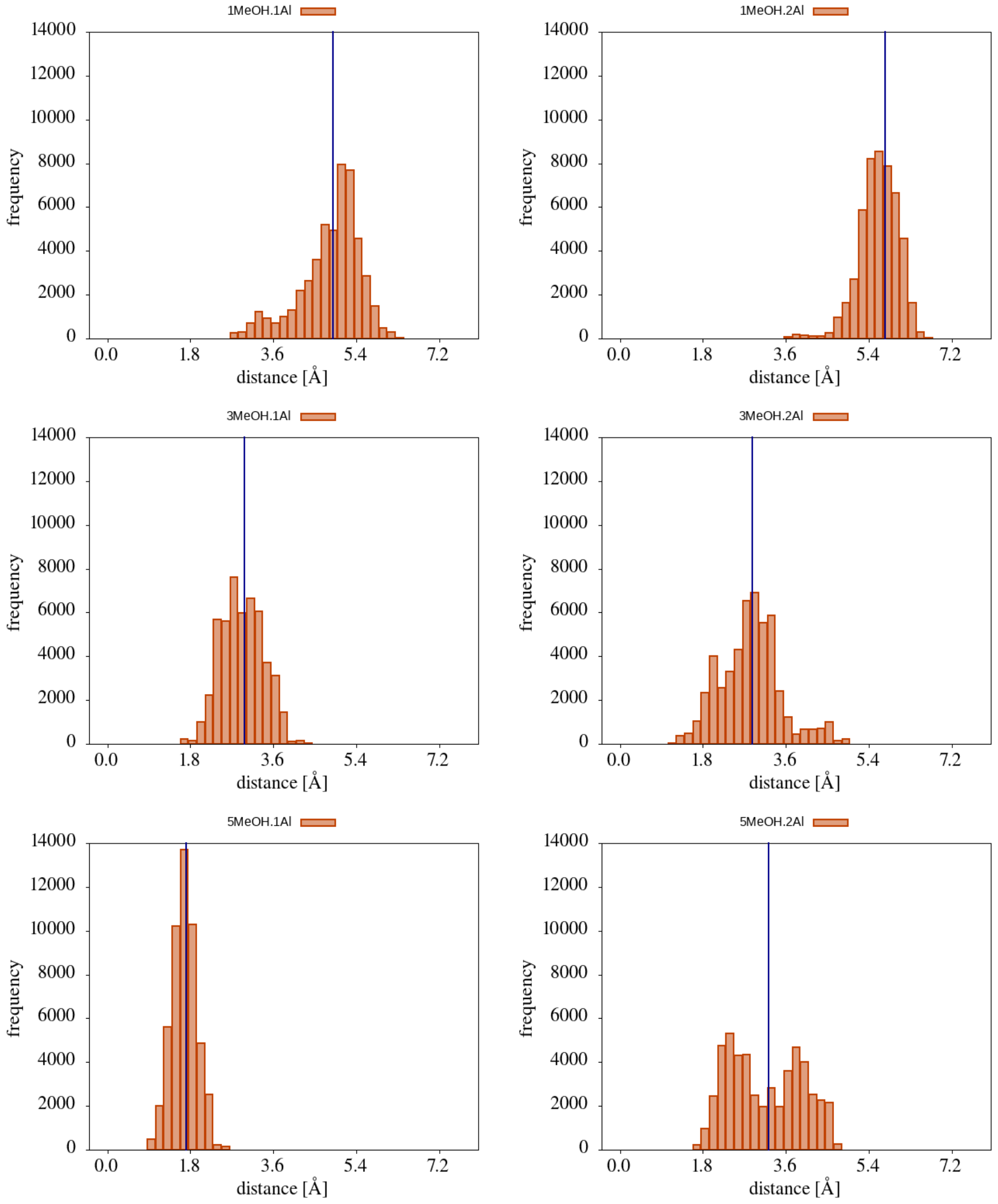

Figure 4.12. Frequency analysis during 50 ps NVT run of the distance between the geometric centre for the methanol cluster (M) and the centre of the zeolite pore (R), presented in Å. Models are considered having one (left column) and two (right column) acid sites, with one (top row), three (middle row) and five (bottom row) methanol molecules per unit cell. A dark-blue vertical line highlights the average distance.

4.3.2 Framework methylation

Spontaneous conversion of methanol to framework methoxy- groups was not observed in our molecular dynamics simulations, which is expected as methylation is generally considered to be an activated process. To sample methylation events with higher probability, we employed enhanced sampling molecular dynamics simulations, as explained in the methodology section. The calculated free energies of methylation are given in Table 4.11, alongside with the values obtained in the work of Van Der Mynsbrugge et al.[4]

Table 4.11. Free energies for zeolite methylation (ΔF), presented in kJ/mol.

	This study (300 K)		Other study (623 K)[4]
	Si/Al ratio		
Methanol/u.c.	47	95	95
1 MeOH	155 ± 3	160 ± 2	160 ± 5
3 MeOH	152 ± 3	171 ± 5	-
5 MeOH	119 ± 2	156 ± 2	139 ± 2*

"-" no results to present

*Results from the conversion of methanol co-adsorbed with three methanol molecules and one water molecule

As with previous static calculation, we find that the activation energy decreases with methanol loading, although not as significantly as proposed in the earlier studies. This discrepancy may be due to a different initial state found in the metadynamics sampling as opposed to that employed in static calculations. Specifically, static simulations of methanol in H-ZSM-5 commonly have the single methanol adsorbed in a non-protonated state, and only as protonated when co-adsorbing polar molecules around the main reactant. In contrast, in our MD simulations, 10% of the production run for a single methanol corresponds to the ground state protonated methoxonium, which eliminates the protonation step necessary in static calculations and leads to a limited difference between an unassisted (i.e. single) and assisted methylation.

When analysing the unassisted methanol conversion, our results show that acid site loading has limited effect on reaction barriers of ~160 kJ/mol; furthermore, comparison with previous literature shows that temperature has limited effect on the reaction barrier (160 ± 2 kJ/mol). For three methanol per unit cell we see an increase in the free energy barrier with increasing acid site density. Here, the large space in the zeolite channel probably gives a high degree of freedom for the methanol molecules, which then allows the methanol cluster to stabilise further from the active site (Figure 4.8), in turn hindering the methyl transfer to the zeolite framework ($\Delta F = 171 \pm 5$ kJ/mol). When considering framework methylation for systems with five methanol molecules, the barrier observed in our simulations drops significantly with doubling of the acid site density, from 156 ± 2 kJ/mol to 119 ± 2 kJ/mol; it is also noted that, for Si/Al ratios of 95, comparison to previous work implies a reduction in the free energy barrier occurs with elevated temperature (139 ± 2 kJ/mol at 623 K).[4] In the latter case, the high temperatures are thought to have a destabilising effect that facilitates a smooth breaking and rearrangement of the hydrogen bonds within the methanol cluster or on the active site[4]; the same behavior is unlikely at low temperatures, as the methanol cluster is very stable, and hence our results are slightly higher in energy.

In order to understand further the lowering of the activation barrier for the simulation containing 5 methanol molecules, we rigorously analysed the trajectory geometries. During the MTD simulation, it is observed that three methanol molecules coordinate on the T12 acid site and two on the other T8 site, in the vicinity of the second deprotonated active site. The clustering of the methanol molecules leads to framework deprotonation and then, as the simulation proceeds, the trimer of methanol molecules forms a linear chain across the zeolite ring therefore interacting with both T12 and T8 sites simultaneously (Figure 4.13). The formation of this structure leads to a concerted polarization effect along the O-H bonds of the methanol trimer, which contributes to the abstraction of electron density off the H-O-H$^+$ group and, in turn, lengthening of the C-O bond (Figure 4.8), leading to a lower activation barrier (119 ± 2 kJ/mol) than observed previously for less acidic zeolites[4]. Experimental studies, as expected find that methylation occurs faster at higher temperatures,[32] which, apart from thermal factors thermal effects, may arise partly from the need for a second acid site to be present in the vicinity of the reactant methanol cluster; this proposal is corroborated by our simulations with one acid site per unit cell, where a lower temperature (300 K, ΔF = 156 ± 2 kJ/mol) results in a higher activation energy than previous work at 623 K (ΔF = 139 ± 2 kJ/mol).

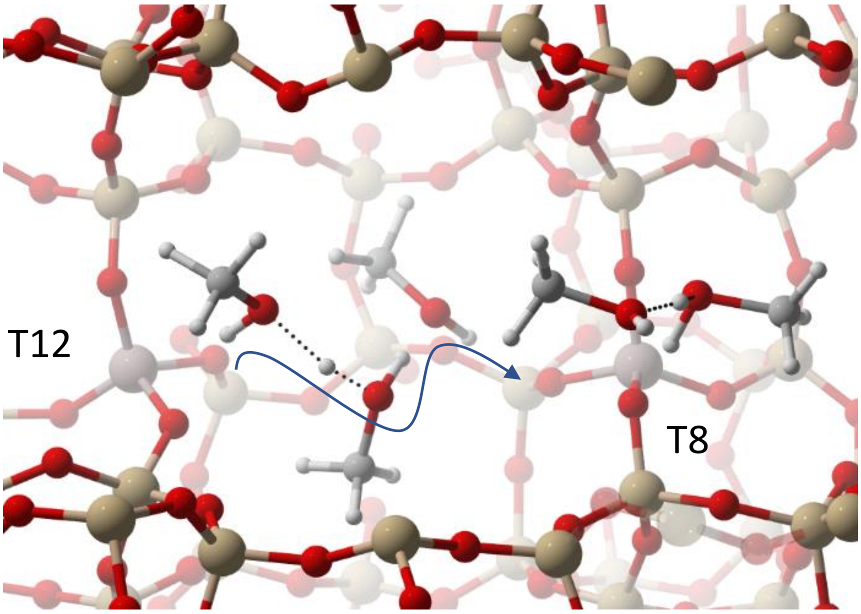

Figure 4.13. MTD simulation snapshot of 5 MeOH per unit cell (Si/Al=47), with blue arrow highlighting the polarization effect of the T8 site, along the hydroxyl groups. The key is as per Figure 4.7.

At low temperatures, the dominant methanol conversion pathway is reported to be direct formation of dimethyl ether[33] (DME) rather than framework methylation, which is active at high temperatures; however, experimental reports suggest that surface methoxy groups are formed initially when synthesising a zeolite with "paired" acid sites[8]. Methanol also homo-associates at high concentrations[34], which increases the acidity of the environment (Scheme 4.1.A), and may facilitate room temperature methylation that only occurs at a high methanol loading. The large methanol clusters, present at lower temperatures, not only would stabilise the charge distribution correspondent to homo-association (Scheme 4.1.B), but would also facilitate the existence of basic Lewis sites, which would aid the methyl transfer in the "paired" active site environment. However, at low loadings, the methyl transfer is more likely to occur on an additional methanol due to a more favourable molecular orientation, (Scheme 4.1.C). We will analyse these concepts further in a future study.

A) Homo and hetero-association:

$2CH_3OH \leftrightarrow CH_3OH_2^+ + CH_3O^-$

$2CH_3OH + ZeOH \leftrightarrow 2CH_3OH \cdots H^+ \cdots ZeO^-$

B) Methylation path:

$CH_3OH_2^+ + CH_3O^- + ZeOH \leftrightarrow CH_3OH_2^+ + CH_3O^- \cdots H^+ \cdots ZeO^-$

$ZeO^- + CH_3OH_2^+ + CH_3O^- \cdots H^+ \cdots ZeO^- \leftrightarrow ZeOCH_3 + H_2O + CH_3O^- \cdots H^+ \cdots ZeO^-$

C) Direct DME formation path:

$ZeOH + CH_3OH_2^+ + CH_3O^- \cdots H^+ \cdots ZeO^- \leftrightarrow ZeOH + CH_3OCH_3 + ZeOH + H_2O$

Scheme 4.1. Proposed methylation and DME formation reaction paths at low temperatures and high pressure, in a "paired" active site environment.

In our analysis of the assisted methanol conversion into a methylated zeolite framework, we find that the backwards reaction (from product to reactant) becomes increasingly favourable as additional methanol molecules are included in the simulation (Table 4.12).

Table 4.12. Kinetic properties and MEP barriers derived from the FES analysis, specifically, free energy barriers of the forward reaction - reactant to product (ΔF_F), backward reaction - product to reactant, (ΔF_B) presented in kJ/mol, reaction rates of the forward (k_F) and backward reactions (k_B) (given in s^{-1}).

		Phenomenological barriers		Kinetic rates	
Si/Al ratio	Methanol/u.c.	ΔF_F	ΔF_B	k_F	k_B
95	1 MeOH	148.72	104.75	$7.99 \cdot 10^{-14}$	$3.61 \cdot 10^{-6}$
47		143.18	84.48	$7.37 \cdot 10^{-13}$	$1.22 \cdot 10^{-2}$
95	3 MeOH	169.47	54.99	$1.94 \cdot 10^{-17}$	$1.66 \cdot 10^{3}$
47		141.60	78.93	$1.38 \cdot 10^{-12}$	$1.13 \cdot 10^{-1}$
95	5 MeOH	149.33	44.28	$6.24 \cdot 10^{-14}$	$1.22 \cdot 10^{5}$
47		112.34	66.38	$1.73 \cdot 10^{-7}$	$1.73 \cdot 10$

The kinetic rates calculated with the free energy barrier are many orders of magnitude higher for the backward reaction, implying that this would be a significant limitation for the stability of the methoxy- group. The ease of the backwards conversion, from a water molecule (product state) into methanol, with increasing quantities of methanol, is promoted by the methanol molecules (cluster) polarizing the water molecule when close to the methyl fragment (similar to the lower barrier for framework deprotonation); the same effect is not observed in the single methanol methylation because no polarization can occur.

4.4. Summary and Conclusions

Using *ab initio* molecular dynamics, the dynamics of methanol has been studied in the zeolite H-ZSM-5 in order to elucidate the initial stages of the MTH process at room temperature. The interaction of methanol with different Brønsted acid sites has been studied in detail, to understand the role of environment on framework methylation. Our simulations suggest that the methanol molecules form clusters around the active site, which then facilitate acid site deprotonation. The subsequent charged methanol clusters stabilise around the active site, at a distance that is dependent on the number of methanol molecules in the cluster. Inclusion of a second acid site in close proximity affects the stability of the methanol cluster and alters the energy barrier for subsequent methylation of the framework.

To understand further the reaction pathway for framework methylation, enhanced sampling molecular dynamics simulations were performed. For low methanol loading, the reaction barriers are consistent with varying acid site density; however, at higher acid site density, the energy barriers are significantly altered by concerted interactions between acid sites that can lower reaction barriers. Confinement effects and additional methanol molecules play some role in stabilising the methanol clusters and aid the methylation process, though not to the extent as experimentally observed. This finding hints at a different type of active site being involved in the methylation process, which leads to further investigations through broader analysis of other T-sites. Future work will also consider a third acid site in the unit cell, alongside a higher reactant loading, to determine the extent to which the activation barrier can be decreased further through concerted behaviour.

References:

1 T. Maihom, B. Boekfa, J. Sirijaraensre, T. Nanok, M. Probst and J. Limtrakul, *J. Phys. Chem. C*, 2009, **113**, 6654–6662.
2 S. R. Blaszkowski and R. A. van Santen, *J. Phys. Chem.*, 1995, **99**, 11728–11738.
3 C. W. Kim, N. H. Heo and K. Seff, *J. Phys. Chem. C*, 2011, **115**, 24823–24838.
4 J. Van Der Mynsbrugge, S. L. C. Moors, K. De Wispelaere and V. Van Speybroeck, *ChemCatChem*, 2014, **6**, 1906–1918.
5 S. L. C. Moors, K. De Wispelaere, J. Van Der Mynsbrugge, M. Waroquier and V. Van Speybroeck, *ACS Catal.*, 2013, **3**, 2556–2567.
6 B. C. Knott, C. T. Nimlos, D. J. Robichaud, M. R. Nimlos, S. Kim and R. Gounder, *ACS Catal.*, 2018, **8**, 770–784.
7 W. Loewenstein, *Am. Mineral.*, 1954, **39**, 92–96.
8 J. R. Di Iorio, C. T. Nimlos and R. Gounder, *ACS Catal.*, 2017, **7**, 6663–6674.
9 T. Bučko, S. Chibani, J.-F. Paul, L. Cantrel and M. Badawi, *Phys. Chem. Chem. Phys.*, 2017, **19**, 27530–27543.
10 S. Bailleul, I. Yarulina, A. E. J. Hoffman, A. Dokania, E. Abou-Hamad, A. D. Chowdhury, G. Pieters, J. Hajek, K. De Wispelaere, M. Waroquier, J. Gascon and V. Van Speybroeck, *J. Am. Chem. Soc.*, , DOI:10.1021/jacs.9b07484.
11 J. VandeVondele, M. Krack, F. Mohamed, M. Parrinello, T. Chassaing and J. Hutter, *Comput. Phys. Commun.*, 2005, **167**, 103–128.
12 K. Yang, J. Zheng, Y. Zhao and D. G. Truhlar, *J. Chem. Phys.*, 2010, **132**, 164117.
13 S. Grimme, J. Antony, S. Ehrlich and H. Krieg, *J. Chem. Phys.*, 2010, **132**, 154104–154104.
14 G. Lippert, J. Hutter and M. Parrinello, *Theor. Chem. Acc.*, 1999, **103**, 124–140.
15 S. Goedecker and M. Teter, *Phys. Rev. B - Condens. Matter Mater. Phys.*, 1996, **54**, 1703–1710.
16 S. Nosé, *J. Chem. Phys.*, 1984, **81**, 511–519.
17 W. G. Hoover, *Phys. Rev. A*, 1985, **31**, 1695–1697.
18 G. J. Martyna, D. J. Tobias and M. L. Klein, *J. Chem. Phys.*, 1994, **101**, 4177–4189.
19 T. F. Willems, C. H. Rycroft, M. Kazi, J. C. Meza and M. Haranczyk, *Microporous Mesoporous Mater.*, 2012, **149**, 134–141.
20 T. Omojola, N. Cherkasov, A. I. McNab, D. B. Lukyanov, J. A. Anderson, E. V. Rebrov and A. C. van Veen, *Catal. Lett.*, 2018, **148**, 474–488.
21 G. Bussi, A. Laio and M. Parrinello, *Phys. Rev. Lett.*, 2006, **96**, 090601.
22 A. Laio and M. Parrinello, *Proc. Natl. Acad. Sci. U. S. A.*, 2002, **99**, 12562–12566.
23 A. Laio and F. L. Gervasio, *Rep. Prog. Phys.*, 2008, **71**, 126601.
24 K. D. Wispelaere, S. Bailleul and V. V. Speybroeck, *Catal. Sci. Technol.*, 2016, **6**, 2686–2705.
25 S. A. F. Nastase, A. J. O'Malley, C. R. A. Catlow and A. J. Logsdail, *Phys. Chem. Chem. Phys.*, 2019, **21**, 2639–2650.
26 C.-C. Lee, R. J. Gorte and W. E. Farneth, *J. Phys. Chem. B*, 1997, **101**, 3811–3817.

27 A. Zecchina, S. Bordiga, G. Spoto, D. Scarano, G. Spanò and F. Geobaldo, *J. Chem. Soc. - Faraday Trans.*, 1996, **92**, 4863–4875.
28 M. W. Anderson, P. J. Barrie and J. Klinowski, *J Phys Chem*, 1991, **95**, 235–239.
29 H. Koller, G. Engelhardt and R. A. van Santen, *Top. Catal.*, 1999, **9**, 163–180.
30 E. S. Stoyanov, I. V. Stoyanova and C. A. Reed, *Chem. - Eur. J.*, 2008, **14**, 3596–3604.
31 D. F. Plant, G. Maurin and R. G. Bell, *J. Phys. Chem. B*, 2007, **111**, 2836–2844.
32 W. Wang, A. Buchholz, M. Seiler and M. Hunger, *J. Am. Chem. Soc.*, 2003, **125**, 15260–15267.
33 C. Ortega, M. Rezaei, V. Hessel and G. Kolb, *Chem. Eng. J.*, 2018, **347**, 741–753.
34 Y. B. Monakhova and S. P. Mushtakova, *Russ. J. Phys. Chem. A*, 2014, **88**, 798–802.

Chapter 5. QM/MM study of zeolite bound methoxy groups reactivity

The work in this chapter covers a wide range of possibilities in which zeolite bound methoxy can be a reactant that could potentially initiate the hydrocarbon formation in the MTH process. Recent experimental studies highlighted that pure methoxylated zeolites are able to produce hydrocarbons. This observation indicated that C1 species, thought to be separately placed on different active sites, are able to interact. Based on our simulations, we demonstrate that it is highly unlikely that methyl groups are able to be on the same active site. However, we show a carbene moiety would be stable enough to react and possibly migrate to other sites.

5.1. Introduction

As mentioned in the Introduction, several studies[1,2] reported the possibility of pure methylated zeolite frameworks, of several types (CH_3-ZSM-5, CH_3-Y, CH_3-SAPO-34), having the potential to form a wide range of hydrocarbons (paraffins, olefins, aromatics). Recent studies[3] highlighted the formation of carbene species from methyl groups. However, previous theoretical studies showed that the direct conversion of methyl to carbene is energetically demanding, both thermodynamically and kinetically.[4,5] In order for C1 species to react and form higher order hydrocarbons, the main reactants have to be in the neighbourhood of one another and considering that only one methanol can convert on one acid site, the possibility of the C1 species migrating next to each other is analysed in this chapter.

Two potential routes ensuring the methyl groups interact with one another were investigated: i) the conversion of methanol leading to methyl transferring on a Si-O-Si basic site, which would exothermically migrate towards an Al-O-Si site and ii) the direct migration of methyl outside of the Al-O-Si active site to a second methylated active site. Furthermore, in order to gain more insight into the conditions leading to carbene formation, new potential models leading to a stable carbene on the zeolite framework and the possibility of carbene migration were investigated.

5.2. Methodology

5.2.1. Model description

In this chapter, we continue to use our QM/MM embedded cluster model as outlined in Section 3.2. The specific zeolite model used in this case was H-ZSM-5, with the active site of interest being the T12 (intersectional) position. All other settings are as described previously in Section 3.2.

Throughout, the same QM/MM and geometry optimisation setup was employed as in the Section 3.2. The transition state energies were determined by employing the Nudged Elastic Band (NEB) method[6], described in Section 2.1.5.1, in the task-farmed mode, with the reaction path represented by 5 images. For the NEB calculations, only the second nearest neighbour framework atoms, and the adsorbate atoms were displaced; comparison of this approximation against displacement of all atoms in the QM region shows small differences in the transition state energies. Specifically, the transition state in which all atoms are relaxed is 10 kJ/mol lower that with a reduced relaxed region. The transition state of the dimer method was confirmed by the single imaginary frequency obtained from vibrational frequency calculations, determined using ChemShell, with a task-farmed finite-difference approach.[7]

Where relevant, the deprotonated zeolite energy was corrected by the addition of the Jost correction,[8,9] to the calculated absolute energy, which accounts for the truncation of the MM polarisation at the end of the first (flexible) MM region. Upon the creation of charge in the structure due to the deprotonation in the QM region, the atoms in the fixed MM region would also move to a slightly lower energy position in response to the localised electron on the QM O^-. The Jost correction takes account of this by calculating the energy gained at this distance based on the dielectric constant of the material. It has the form:

$$\mathrm{E}_{Jost} = \frac{Q^2}{2\mathrm{R}}\left(1 - \frac{1}{\varepsilon}\right) \tag{5.1}$$

Q is the charge defect, R is the radius of the total cluster and ε is the dielectric constant of the material, taken as 3.38 for MFI, calculated using classical shell model methods.[10]

5.2.2. Energy analysis

In addition to the previous energy parameters mentioned in Chapter 3, specifically the adsorption (E_{ads}), methylation reaction (E_R) and activation (E_a) energies, two other thermodynamic energy descriptors are used in this chapter: the reaction energy for methyl (carbene) to migrate from one bonding site (O_A) to another (O_B) - E_{mig}, bonding energy of methyl (carbene) to the oxygen bonding site of the zeolite framework - E_{bond}, calculated as follows:

$E_{mig} = E_{OB} - E_{OA}$ (5.2), with E_{OB}, E_{OA} the absolute energies of the methyl bonded to the zeolite framework on Lewis basic sites O_B and O_A

$E_{bond} = E_{C1\text{-}Zeo} - E_{C1} - E_{Zeo\text{-}}$ (5.3) with $E_{C1\text{-}Zeo}$, E_{C1}, $E_{Zeo\text{-}}$ absolute energies of the methyl bonded zeolite framework, gas phase methyl (CH_3^+) or carbene (CH_2:) fragments and deprotonated zeolite models.

5.3. Results

5.3.1. Internal methyl migration

This study builds on the single methanol adsorption case described in Chapter 3, with the analysis taken a step further, towards methanol conversion to methoxy in two distinct ways. As mentioned in Chapter 3, it is known that methyl is most likely to bond on the oxygen neighbouring the Al site. However, for the methyl groups to end up neighbouring so they can react together, the stability of the methyl group associate on two Lewis basic sites was analysed described in Figure 5.1. In this study, the stability of the methoxy group was analysed relative to the Al-site coordinated (O_{Al}) methoxy, as we have outlined in Chapter 3, with alternative methoxy locations being on oxygen atoms neighboured explicitly by silicon atoms (O_{Si}).

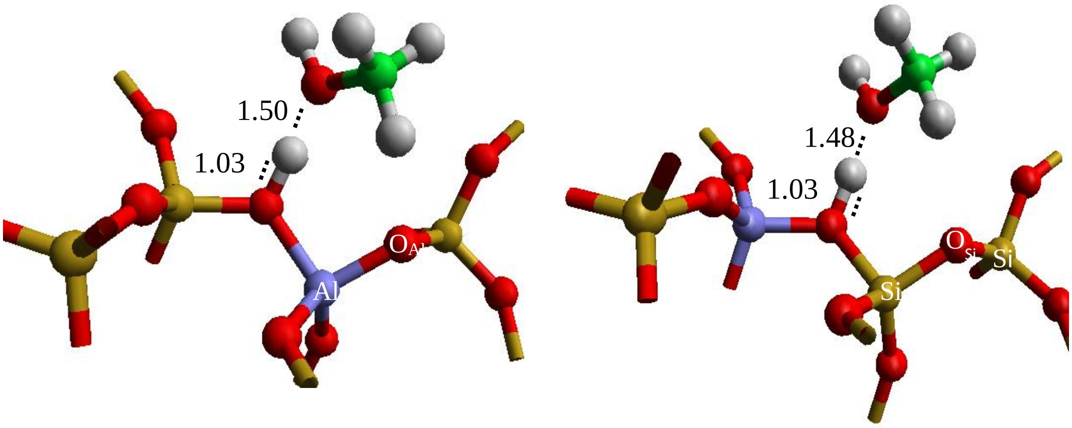

Figure 5.1. Methanol models, with methyl oriented towards aluminium (left) and towards silicon (right); and geometric assignment, with the following atoms represent as Al - purple, Si - yellow, O - red, C - green, H - white and methoxy bonding sites as O_{Al} and O_{Si} representing the Al neighbouring sites and external bonding sites, also Si and Si are represented as they will be referenced in the structural analysis.*

Methanol was adsorbed on the Brønsted acid site with the methyl group oriented towards the active site centred on the Al T-site, for the methyl to transfer on O_{Al} and outside the active site centred on the Si T-site, for a methyl transfer on O_{Si} (Figure 5.1). The optimised structures of the two configurations and adsorption energies of methanol, were similar, with the distance of the Brønsted proton and methanol molecules to the zeolite having approximately the same values, leading to comparable adsorption energies, as provided in Table 5.1. The methanol adsorption study in Chapter 3, concluded that methyl interaction does not contribute as much to the overall adsorption energy, with the "bulk" of the contribution coming from the hydroxyl group, with the current results further emphasising that. However, the activation energy for methylating a Al-O-Si site is of 225 kJ/mol, with a reaction energy of 49 kJ/mol, whereas to methylate a O_{Si} site then the activation energy is three times higher than the previous case, i.e. 748 kJ/mol with a reaction energy of 118 kJ/mol (Table 5.1).

Table 5.1. Summary of results for methanol adsorbed on active sites with methyl oriented towards aluminium ($CH_3OH.O_{Al}$) and silicon ($CH_3OH.O_{Si}$) centres, alongside methoxy formation on oxygen closer to aluminium ($CH_3.H_2O.O_{Al}$) and silicon ($CH_3.H_2O.O_{Si}$) as shown in Figure 5.1, with adsorption energies (E_{ads}), reaction energies (E_R) and activation energies (E_a) energies given in kJ/mol; geometric parameters (d) and charge (q) data are presented in Ångstroms and electronic charge (e), respectively.

	E_{ads}	E_R	E_a		
$CH_3OH.O_{Al}$	-120	49	225		
$CH_3OH.O_{Si}$	-126	118	748		
			d		
$CH_3OH.O_{Al}$	$Al\text{-}O_{Al}$	$O_{Al}\text{-}Si$	$O_{MeOH}\text{-}H_{ZeO}$	$O_{ZeO}\text{-}H_{ZeO}$	
	1.85	1.66	1.5	1.03	
$CH_3OH.O_{Si}$	$Si\text{-}O_{Si}$	O_{Si} -Si*	$O_{MeOH}\text{-}H_{ZeO}$	$O_{ZeO}\text{-}H_{ZeO}$	
	1.82	1.67	1.48	1.03	
$CH_3.H_2O.O_{Al}$	$Al\text{-}O_{Al}$	$C\text{-}O_{Al}$	$C\text{-}O_{H2O}$		
	1.84	1.48	3.14		
$CH_3.H_2O.O_{Si}$	$Si\text{-}O_{Si}$	$C\text{-}O_{Si}$	$C\text{-}O_{H2O}$		
	1.77	1.51	3.05		
			q		
$CH_3OH.O_{Al}$	Al	O_{Al}	H_{ZeO}	O_{MeOH}	C
	0.97	-0.61	0.44	-0.53	-0.25
$CH_3OH.O_{Si}$	Si	O_{Si}	H_{ZeO}	O_{MeOH}	C
	1.00	-0.61	0.43	-0.52	-0.24
$CH_3.H_2O.O_{Al}$	Al	O_{Al}	C		
	0.96	-0.53	-0.27		
$CH_3.H_2O.O_{Si}$	Si	O_{Si}	C		
	1.02	-0.49	0.27		

The methylation path, in both cases (Figure 5.2) requires the Brønsted proton to transfer completely from the active site to the methanol, in order for the dissociation of the $C_{MeOH}\text{-}O_{MeOH}$ bond and the formation of water. Similar methanol adsorption energies (~ -120 kJ/mol) are encountered, and overall structures (geometries and charges, as shown in Table 5.1) are comparable, which means that the energy to subtract the Brønsted proton from the active site on to the methanol, in both cases, is expected to be the same. Since the initial step of the methylation path, specifically, the deprotonation of the zeolite is not contributing to the significant difference on the activation barrier, between the two cases (inside and outside methylation of the active site), we conclude that the difficulty of stabilising the methyl fragment on the zeolite, is the main reason behind the considerably higher activation energy for methylating the O_{Si} as opposed to the O_{Al}.

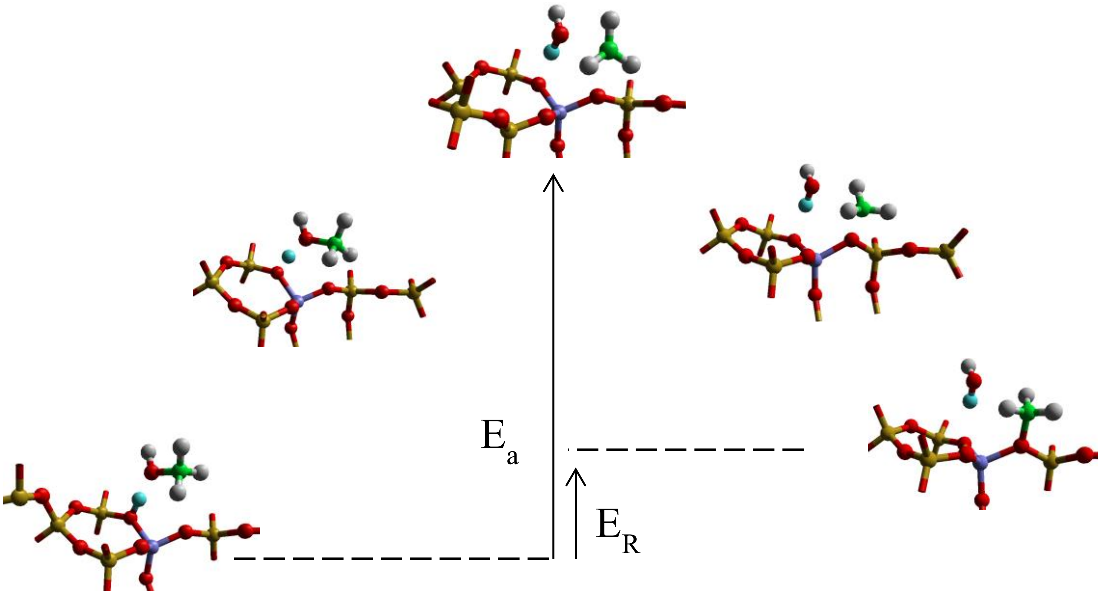

Figure 5.2. Methoxylation reaction path, with the Brønsted proton highlighted in blue for clarity.

5.3.2. Methyl migration away from the active site

The investigation was extended by analysing the possibility of a framework-adsorbed methoxy group migrating away from the active site, from O_{Al} to O_{Si}, with bonding sites presented in Figure 5.3.

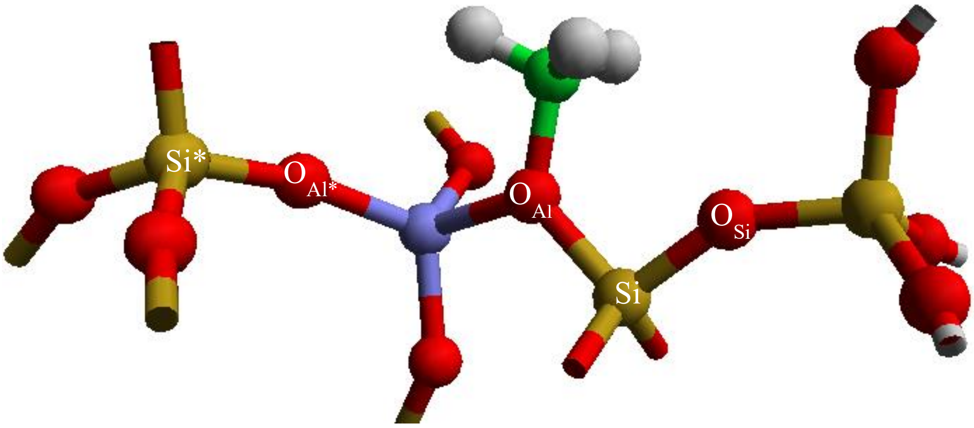

Figure 5.3. Methoxy model and geometric assignment, with the following atoms represent as Al - purple, Si - yellow, O - red, C - green, H - white and methoxy bonding sites as O_{Al} *and* O_{Al^*} *representing the Al neighbouring sites and* O_{Si} *and* O_{Si^*} *representing external bonding sites, also Si and Si* are represented as they will be referenced in the structural analysis.*

Thermodynamically, the reaction energy for methyl transfer is 125 kJ/mol. The analysis of the charges and bond lengths of the framework surrounding the methyl moiety, with detailed electronic and geometric parameters provided in Table 5.2, shows that the main structural differences determining the high endothermic reaction energy value were within the first nearest neighbour of the methyl group, since the remaining extended structure to the third nearest neighbour was similar in both cases.

Table 5.2. Summary of results for methyl (CH_3) group bonded on O_{Al*}. O_{Al}, O_{Si} sites, with bonding energy (E_{bond}) and migration energy (E_{mig}) for migration from O_{Al*} to O_{Al} and from O_{Al} to O_{Si}, given in kJ/mol. Geometric and charge observations are presented in Ångstroms and electronic charge (e), respectively. The specific methyl bonding sites were highlighted in bold.

	E_{bond}	E_{mig}				
$CH_3.O_{Si}$	-510	126				
$CH_3.O_{Al}$	-621	-14				
$CH_3.O_{Al*}$	-635					
	d					
$CH_3.O_{Si}$	O_{Al*}-Al	Al-O_{Al}	O_{Al}-Si	Si-O_{Si}	O_{Si*}-Si*	O-C
	1.71	1.76	1.57	1.81	1.69	1.52
$CH_3.O_{Al}$	O_{Al*}-Al	Al-O_{Al}	O_{Al}-Si	Si-O_{Si}	O_{Si*}-Si*	O-C
	1.7	1.85	1.69	1.61	1.60	1.47
$CH_3.O_{Al*}$	O_{Al*}-Al	Al-O_{Al}	O_{Al}-Si	Si-O_{Si}	O_{Si*}-Si*	O-C
	1.89	1.7	1.59	1.62	1.60	1.48
	q					
$CH_3.O_{Si}$	O_{Al*}	Al	O_{Al}	**O_{Si*}**	C	
	-0.59	0.96	-0.59	-0.45	-0.22	
$CH_3.O_{Al}$	O_{Al*}	Al	**O_{Al}**	O_{Si*}	C	
	-0.56	0.94	-0.51	-0.5	-0.25	
$CH_3.O_{Al*}$	**O_{Al*}**	Al	O_{Al}	O_{Si*}	C	
	-0.53	1	-0.59	-0.49	-0.3	

The methyl strongly bonds to the zeolite framework achieved between C-O_{Al} (E_{Bond} = -635 kJ/mol) as opposed to the C-O_{Si} case (E_{Bond} = -510 kJ/mol). The analysis between the O_{Al} and O_{Si} methyl bonded models, shows that the length of the C-O_{Si} bond (1.52 Å) highlights a low interaction with the zeolite framework when compared to a C-O_{Al} distance of 1.48 Å. In addition, the relative charge on C_{OSi} (-0.45 e) as opposed to C_{OAl} (-0.51 e) shows a limited charge transfer between the methyl group and the Lewis basic site of the zeolite, when the oxygen bonding site is surrounded by Si atoms which further emphasises the necessity for the methyl to stabilise closer to the Al T-site.

To further clarify the stability of methyl in different framework positions, and the factors which influence it, the energetics involved in a methyl transferring from the O_{Al} site to O_{Al*} were compared. The reaction energy for methyl to migrate from O_{Al} to O_{Al*}, is lower (-14 kJ/mol) than transferring from O_{Al} to O_{Si} (126 kJ/mol), illustrating that the methyl group is more stable on the Lewis basic sites that neighbour an Al T-site. The methyl bonding energy on O_{Al*} (E_{Bond} = -621 kJ/mol) is stronger than on O_{Al} (E_{Bond} = -635 kJ/mol), with the C-O_{Al*} bond of 1.48 Å is marginally larger than the C-O_{Al} distance (1.47 Å). In contrast, a higher negative charge is present on the C_{OAl*} (-0.30 e) than on C_{OAl} (-0.25 e), with the charge on O_{Al*} (-0.53 e) as opposed to O_{Al} (-0.51 e), highlights the instability created by the higher electronic density present at the O_{Al*} Lewis site.

To understand how multiple methyl groups might interact, simulations involving two methyl groups on the same active site were considered (Figure 5.4).

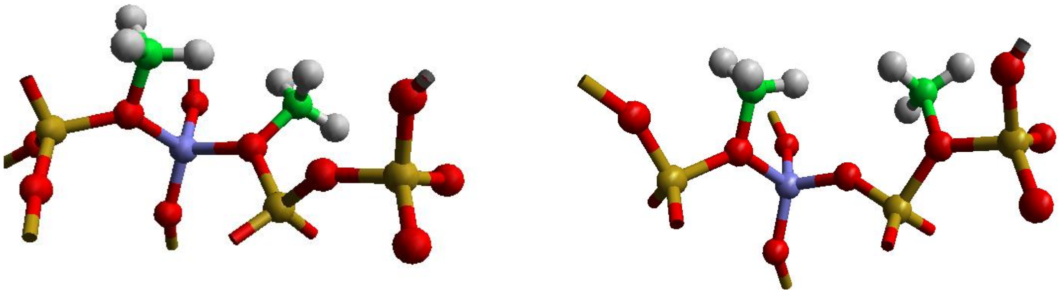

Figure 5.4. Models with additional methyl bonded on O_{Al}(left) and O_{Si} (right), with key as per Figure 5.1.

The additional methyl moiety on the active site led to a lower methyl transfer energy (81 kJ/mol) compared to the single methyl adsorption case (126 kJ/mol), due to the smaller distance between O_{Al}, O_{Si} methylation sites, as highlighted by the bond lengths presented in Table 5.3.

Table 5.3. Summary of results when two methyl (CH_3) groups are bonded on O_{Al*} and O_{Al} ($2CH_3.O_{Al}$) and on O_{Al*} and O_{Si} ($2CH_3.O_{Si}$) sites, with bonding energy (E_{Bond}) and migration energy (E_{mig}), from O_{Al} to O_{Si}, given in kJ/mol. Geometric and charge observables are presented in Ångstroms and electronic charge (e), respectively. The specific bonding sites were highlighted in bold.

	E_{Bond}	E_{mig}					
$2CH_3.O_{Al}$	-358						
$2CH_3.O_{Si}$	-277	81					
d							
$2CH_3.O_{Al}$	O_{Al*}-Al	Al-O_{Al}	O_{Al}-Si	Si-O_{Si}	O_{Si}-Si*	O_{Al*}-C	O_{Al}-C
	1.85	1.85	1.71	1.6	1.62	1.49	1.49
$2CH_3.O_{Si}$	O_{Al*}-Al	Al-O_{Al}	O_{Al}-Si	Si-O_{Si}	O_{Si}-Si*	O_{Al*}-C	O_{Al}-C
	1.86	1.72	1.57	1.77	1.71	1.48	1.52
q							
$2CH_3.O_{Al}$	O_{Al*}	Al	O_{Al}	Si	$\mathbf{O_{Si}}$	C_{Al*}	C_{Si}
	-0.09	0.01	-0.16		0.08	-0.42	-0.33
$2CH_3.O_{Si}$	O_{Al*}	Al	$\mathbf{O_{Al}}$	Si	O_{Si}	C_{Al*}	C_{Al}
	-0.11	0.09	-0.1		0.03	-0.43	-0.47

As the negative charge of the deprotonated zeolite framework is neutralised by the first methyl group, an additional (positively charged) methyl would be left with a less basic site to attack. The bonding energies of the second methyl groups added are ~250 kJ/mol higher than the when there is just a single methyl group, further highlighting the lower reaction energy needed to transfer the methyl. However, the reaction energy for the methyl migration, is lower than the single methyl case, but still considerably endothermic, 80 kJ/mol.

5.3.3. Carbene migration

Previous theoretical studies[4,5] showed that the direct formation of carbene from methyl is highly energetically demanding (E_a = 326 kJ/mol)[11], even though the presence of a carbene species has been detected experimentally.[3] In order to determine the conditions leading to the formation of carbene and understand its role on the production of hydrocarbons, several new models were analysed to determine the conditions aiding the formation of carbene. (Figures 5.5 and 5.6).

Figure 5.5. Carbene formation reactions from O_{Al} bonded methyl.

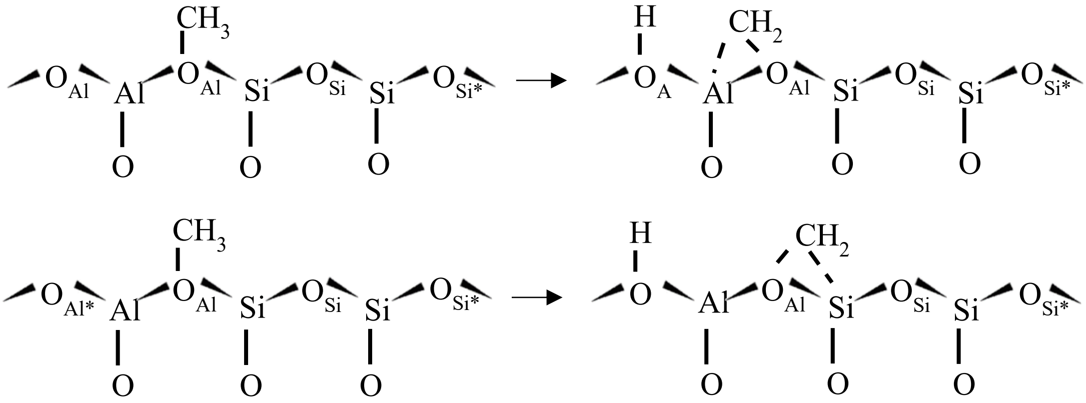

The reaction energies of carbene formation (Table 5.4) arise mainly from the difficulty of stabilising the carbene fragment on the zeolite framework in a configuration preventing the spontaneous conversion back to methyl (Figure 5.4), which was also a challenge reported in other investigations[11].

The carbene stabilises between the cation and oxygen, bonding to both atoms, specifically, Al-C 1.95, C-O_{Al} 1.54 (Figure 5.4. A) and Si-C 1.89, C-O_{Al} 1.55 (Figure 5.4. B). The carbene bonding energies to the zeolite framework, specifically, -174 kJ/mol, -141 kJ/mol, are weaker than the previous (methyl) cases, which is remotely influenced by the absence of the Brønsted proton. The model is 20 kJ/mol less reactive when the proton is removed from the active site, showing how it aids stability. Even so, the carbene bonding energy is strong enough for carbene to remain stable on the zeolite framework enough time to further react with other compounds. In turn, the reaction energy for carbene migration is significantly less energetically demanding than the previously methyl analysed cases (34 kJ/mol), due to the weaker interaction of the carbene with the zeolite framework. Since the carbene is stable on the zeolite framework, we assert that it is possible for the carbene moiety to migrate from one site to another.

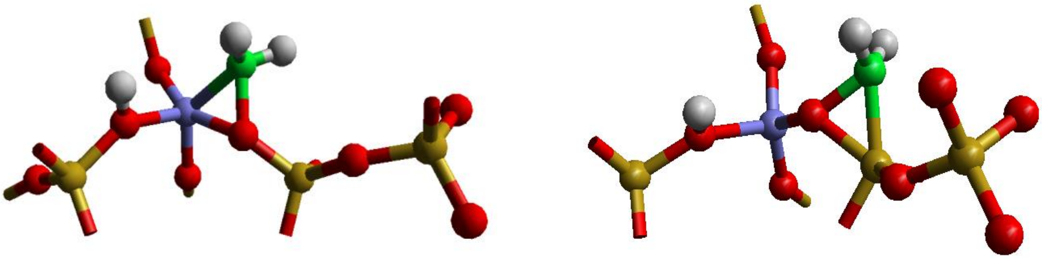

Figure 5.6. Carbene migration from Al (left) to Si (right), with key as per Figure 5.1.

Table 5.4. Summary of results for a carbene (CH_2) moiety formed from the methyl conversion on O_{Al}, bonded in the proximity of Al and Si and formed from the methyl conversion on O_{Si}, bonded in the proximity of Si and Si, with energetic parameters (reaction, migration from Al to Si - E_{mig}, bonding - E_{Bond}, energies) given in kJ/mol, geometric and charge data presented in Ångstroms and electronic charge (e), respectively. The specific bonding sites were highlighted in bold.*

	E_R	E_{Bond}	E_{mig}					
H.CH_2.Al	283	-174						
H.CH_2.Si	317	-141	34					
	d							
H.CH_2.Al	O_{Al*}-Al	O_{Al*}-H	Al-O_{Al}	O_{Al}-Si	Si-O_{Si}	O_{Si}-Si*	Al-C	C-O_{Al}
	1.91	0.97	1.94	1.63	1.60	1.59	1.95	1.54
H.CH_2.Si	O_{Al*}-Al	O_{Al*}-H	Al-O_{Al}	O_{Al}-Si	Si-O_{Si}	O_{Si}-Si*	Al-C	C-O_{Al}
	1.85	0.96	1.75	1.76	1.64	1.59	1.89	1.55
	q							
H.CH_2.Al	O_{Al*}	H	Al	O_{Al}	O_{Si}	C		
	-0.61	0.4	1.05	-0.45	-0.46	-0.56		
H.CH_2.Si	O_{Al*}	H	Al	O_{Al}	O_{Si}	C		
	-0.62	0.41	1.05	-0.53	-0.49	-0.48		

For completeness, the formation of carbene from a methyl outside the active site, specifically on a Si-O-Si site, was also investigated as follows:

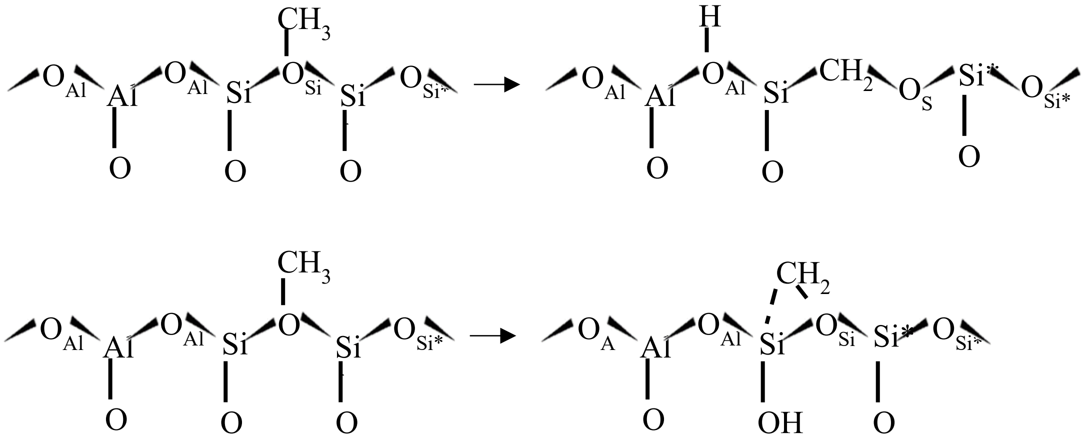

Figure 5.7. Carbene formation reactions from O_{Si} bonded methyl.

The carbene is most stable when placed within the zeolite framework, i.e. inserting itself into the framework, as presented in Figure 5.8, with a reaction energy of 103 kJ/mol (Table 5), which may be due to the flexibility of the framework.

Figure 5.8. Carbene models formed from methoxy bonded on O_{Si} site, in the proximity of Si (left) and Si (right), with key as per Figure 5.1.*

No significant difference was found when forming carbene further from the active site, based on the formation energy from methoxy in the proximity of Si* (239 kJ/mol), which shows that the silicate structure is not enhancing the stability of the carbene.

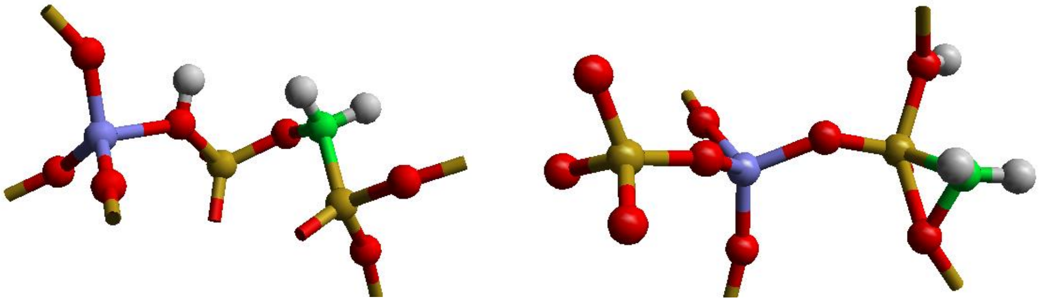

Table 5. Summary of results for a carbene (CH_2) moiety formed from the methyl conversion on O_{Si}, bonded in the proximity of Si and Si and formed from the methyl conversion on O_{Si}, bonded in the proximity of Si and Si*, with reaction energies given*

in kJ/mol, geometric and charge data presented in Ångstroms and electronic charge (e), respectively.

	E_R							
H.CH$_2$.Si	103							
H.CH$_2$.Si*	239							
	d							
H.CH$_2$.Si	O_{Al*}-Al	O_{Al*}-H	Al-O_{Al}	O_{Al}-Si	Si-O_{Si}	O_{Si}-Si*	Si-C	C-O_{Si}
	1.7	0.97	1.88	1.70	1.61	2.78	1.86	1.42
H.CH$_2$.Si*	O_{Al*}-Al	O_{Al*}-H	Al-O_{Al}	O_{Al}-Si	Si-O_{Si}	O_{Si}-Si*	Si-C	C-O_{Si}
	1.72	0.97	1.75	1.56	1.95	1.65	1.82	1.50
	q							
H.CH$_2$.Si	O_{Al*}	H	Al	O_{Al}	O_{Si}	C	O*	
	-0.59	0.40	1.06	-0.64	-0.36	-0.39	-0.49	
H.CH$_2$.Si*	O_{Al*}	H	Al	O_{Al}	O_{Si}	C	O*	
	-0.57	0.39	0.98	-0.56	-0.39	-0.41	-0.61	

5.4. Conclusions

The possibility of C1 species migrating and reacting on the same active site was modelled using QM/MM techniques, for three distinct pathways. Specifically, the formation of methoxy groups beyond the active site was both kinetically and thermodynamically demanding. Based on the methanol adsorption energy, we conclude that the rate determining step for methoxylation is not the Brønsted proton transfer to methanol but the methyl transfer to the active site. No evidence was found suggesting that methyl migration could occur; however, due to the small differences in the basicity of the oxygen atoms surrounding the active site needed to stabilise methyl, we suggest that a zeolite substituted with gallium or indium, may enhance the chances of the methyl forming beyond the active site. In addition, the direct formation of carbene from methyl is highly energetically demanding; however, due to the strong bond formed to the zeolite framework in the absence of a Brønsted proton, the carbene moiety may stabilise for enough time to react with other species.

References:

1 Y. Jiang, M. Hunger and W. Wang, *J. Am. Chem. Soc.*, 2006, **128**, 11679–11692.
2 Wei Wang, Andreas Buchholz, Michael Seiler and Michael Hunger, *JACS*, **125**, 15260–15267.
3 I. B. Minova, S. K. Matam, A. Greenaway, C. R. A. Catlow, M. D. Frogley, G. Cinque, P. A. Wright and R. F. Howe, *ACS Catal.*, 2019, **9**, 6564–6570.
4 P. E. Sinclair and C. R. A. Catlow, *J. Phys. Chem. B*, 1997, **101**, 295–298.
5 G. J. Hutchings, G. W. Watson and D. J. Willock, *Micro Meso Mat*, 1999, **29**, 67–77.
6 G. Henkelman, B. P. Uberuaga and H. Jónsson, *J Chem Phys*, 2000, **113**, 9901–9904.
7 M. F. Guest, I. J. Bush, H. J. Van Dam, P. Sherwood, J. M. H. Thomas, J. H. Van Lenthe, R. W. Havenith and J. Kendrick, *Molec Phys*, 2005, **103**, 719–747.
8 A. A. Sokol, S. T. Bromley, S. A. French, C. R. A. Catlow and P. Sherwood, *Int J Quant Chem*, 2004, **99**, 695–712.
9 W. Jost, *J. Chem. Phys.*, 1933, **1**, 466–475.
10 R. Poloni and J. Kim, *J Mat Chem C*, 2014, **2**, 2298–2300.
11 N. Govind, J. Andzelm, K. Reindel and G. Fitzgerald, *Int J Molec Sci*, 2002, **3**, 423–434.

Chapter 6. QM/MM study on the stability and formation of dimethyl ether in zeolites H-Y and H-ZSM-5

A more comprehensive study on the reactivity of methanol was conducted to gain more insight into the next step in MTH process. In this chapter, QM/MM simulations were done to model the conversion of methanol to dimethyl ether (DME) and analyse the stability of DME on several acid sites in H-ZSM-5 and H-Y. Similar to methanol adsorption in Chapter 3, the T12 intersection site is shown to bond DME the strongest, with a complete deprotonation of the acid site occurring. The conversion of methanol to DME demanded a higher activation energy than methoxylation which indicates that a stepwise (indirect) mechanism, trough methoxy, is based on DME formation.

6.1. Introduction

Since the dehydration of methanol to methoxy is energetically demanding, the direct conversion methanol to dimethyl ether (DME) was analysed as a competing reaction pathway.

Experimental studies suggest that the direct formation of DME from methanol pathway rather than the indirect reaction (via methoxy), is more likely to occur when having "isolated" acid sites[1,2] in the H-ZSM-5 framework; in contrast, the methoxylation pathway is more prevalent when having a "paired" acid site environment[1]. However both reactions are known to increase with acid site strength and density[1,3].

In this study, we determine the characteristics of the zeolite active site that will influence the stability and so, the formation of DME in order to understand what catalytic features are necessary to direct the methanol conversion towards a desired product. IR and NMR studies shown that even at low coverages, DME is both physisorbed and chemisorbed, highlighting that there are acid sites with different bonding capabilities in the zeolite. TPD experiments suggested the existence of high, medium and low temperature desorbing sites, with their characteristics remaining unclear. Previous theoretical simulations of DME adsorption employing small clusters or periodic systems (in H-ZSM-22)[2,4,5,6] reported DME being both in a physisorbed and chemisorbed state.

As discussed in previous chapters, in order to have a more accurate representation of the electrostatics involved, QM/MM methods were employed to simulate the DME formation and adsorption on several Brønsted acid sites in H-ZSM-5 and H-Y for us to establish a clear understanding of the stability of DME in the zeolite pores, and to gain more insight into the specific structural characteristics influencing the interaction between DME and the zeolite catalyst.

6.2. Methodology

In this work, we continue to use our QM/MM embedded cluster model as outlined in Section 3.2. The specific zeolite models used in this case were H-ZSM-5, with the active site of interest being the straight channel [T1 (M7)], the sinusoidal channel [T4 (Z6)] and the more open channel intersections [T12 (I2)] and the only type of active site present in zeolite H-Y. All other settings are as described previously in Section 3.2.

For the geometry optimisations of DME adsorption models were simulated as described in Section 3.2, with the exception that the QM energy has been calculated using hybrid-DFT with the Becke97-D exchange-correlation (XC) functional, [7] as provided in the NWChem[8]. In the case of methanol conversion to DME, in order to have comparable results with the previous methanol conversion analysis discussed in Chapter 5, the B97-3 XC functional[9] was used, with additional energy calculations, where highlighted, performed post-geometry optimisation using the dispersion corrected B97-D functional[7] of NWChem[8].

The transition state energies were determined by employing the Nudged Elastic Band (NEB) method[10] in the task-farmed mode, with the reaction path represented by 15 images. The transition state of the dimer method was confirmed by the single imaginary frequency obtained from vibrational frequency calculations, determined using ChemShell, with a task-farmed finite-difference approach.[11]

Where relevant, the deprotonated zeolite energy was corrected by the addition of the Jost correction,[12,13] to the calculated absolute energy, similar to Section 5.2.1, with the dielectric constant of the material, taken as 2.65 for FAU zeolites and 3.38 for MFI, calculated using classical shell model methods.[14]

6.3. Results

6.3.1. Adsorption of DME

The stability of DME in the zeolite pores was considered by investigating the adsorption of DME on a series of Brønsted acid sites of H-Y and H-ZSM-5. The models were constructed by bonding the oxygen of DME to the Brønsted proton, with the plane of DME perpendicular to that of the active site to ensure a strong guest-host interaction and stabilisation of the adsorbate.

As shown by the results in Table 6.1, the DME adsorption process is calculated to be exothermic. The highest stability is found in the T12 [I2] model (E_{ads}= -143 kJ/mol), followed by H-Y > T1 [M7] > T4 [Z6] cases. Our results find stronger adsorption than in previous small cluster theoretical studies, where E_{ads} is as -62 kJ/mol[15] or -89; -97 kJ/mol[4]. Experimental calorimetric studies report an adsorption enthalpy of -90 kJ/mol at 323 K[16]. In addition, TPD investigations reported that DME at low reactant loadings, has an adsorption enthalpy of -100; -110 kJ/mol at low and medium temperature desorption sites, and -125 kJ/mol for high temperature desorption sites[17], both in H-ZSM-5, that indicate an agreement with our simulated results.

Table 6.1. Calculated adsorption energy (E_{ads}) for the optimised models in this study using the B97-D exchange correlation functional, alongside small cluster[4,15], theoretical adsorption enthalpy at 300 K (H_{ads}, B97-D), compared to experimental[16,17] adsorption enthalpies (H_{ads}, exp), and simulated Gibbs free energies (G_{ads}, B97-D), presented in kJ/mol.

	E_{ads}, B97-D	E_{ads}, cluster	H_{ads}, B97-D	G_{ads}, B97-D	H_{ads}, exp
H-Y	-132	-62[15]; -97[4]	-105	-140	-90[16]; -125[17]
T12 [I2]	-143		-132	-153	
T4 [Z6]	-122		-103	-131	
T1 [M7]	-129		-107	-137	

The geometry optimised models are given in Figure 6.1. The deprotonation of the active site is observed in all cases, with the T12 [I2] model having the proton completely transferred on DME. Previous theoretical simulations of DME adsorption had a range of results: small clusters or periodic systems (in H-ZSM-22)[2,4,5,6] had the proton on the active site, whereas other clusters simulations[15,18] resulted in local minimas with the deprotonated zeolite by DME. IR[4,19] and NMR[20] studies, report that even at low loadings and temperatures (373 K), there is a mixture of physisorbed and chemisorbed state DME in the zeolite pores.

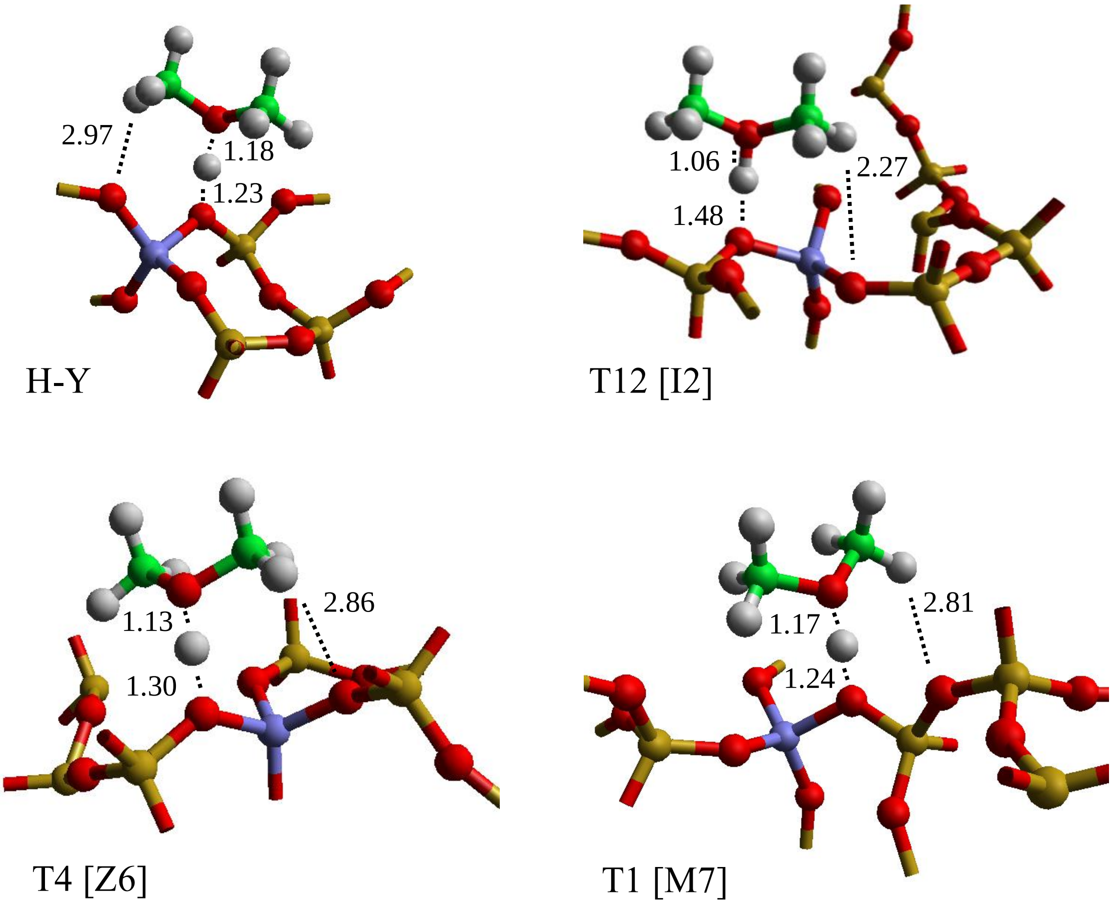

Figure 6.1. Optimised models of DME adsorption on H-ZSM-5 and H-Y sites, with atoms as follows Al (purple), Si (yellow), C (green), O (red), H (light grey). Relevant bonds are highlighted with dashed lines and distances are presented in Ångstroms.

The geometric analysis summarised in Table 6.2 demonstrates the difficulty of determining spectroscopically the type of interactions involving the Brønsted proton, which stabilises approximately at the same distance between the zeolite Lewis site and DME, ~ 1.20 Å apart from the active site and adsorbate, with the H-ZSM-5 [I2] model having the highest proton displacement, with the HB-ODME is 1.06 Å. These results highlight the shallow potential energy surface for proton transfer, with respect to the active site and can explain the interplay between physisorbed and chemisorbed states, detected experimentally.[4,19,20]

Table 6.2. Summary of geometric observables, specifically, the bond length of the Brønsted proton to the zeolite active site d(O_{Zeo}-H_B), and DME d(H_B-O_{DME}), the length between the deprotonated oxygen site and oxygen of DME d(O_{Zeo}-O_{DME}) and the distance of the closest hydrogen of the DME methyl group to the zeolite framework d(O_{Zeo*}-H_{CH3}), presented in Ångstroms.

	d(O_{Zeo}-H_B)	d(H_B-O_{DME})	d(O_{Zeo}-O_{DME})	d(O_{Zeo*}-H_{CH3})
H-Y	1.23	1.18	2.41	2.97
T12 [I2]	1.48	1.06	2.54	2.27
T4 [Z6]	1.30	1.13	2.42	2.86
T1 [M7]	1.24	1.17	2.41	2.81

The model where the DME methyl groups are closest to the active site is T12 [I2], where the distance is 2.27 Å, which is important as it shows that when the DME methyl group is closer to the framework oxygen, there is a stronger electron induced effect on O_{DME}. The strength of the induction effect is determined by the methyl - oxygen Lewis basic active site repulsion, which improve the stabilisation of the protonated DME on the active site.

Figure 6.3 shows a direct trend between the distance of the proton to DME and the active site. The linear trend shown between these two observables, indicates a correlation between the interactions occurring around the Brønsted proton.

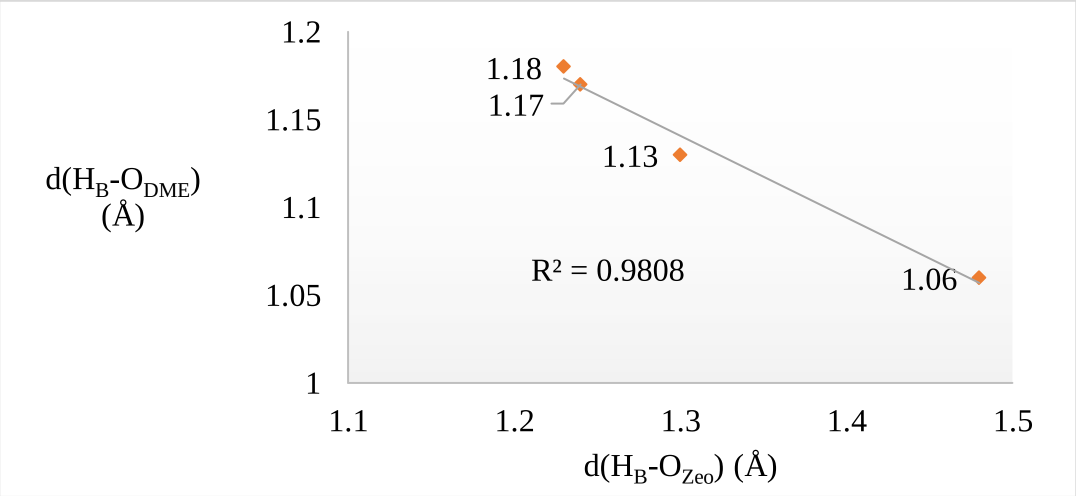

Figure 6.3. Plot comparing the distance of the Brønsted proton from the zeolite d(H_B-O_{Zeo}) and from DME d(H_B-O_{DME}), with the numbers of d(H_B-O_{DME}) also provided in the plot, presented in Ångstroms. The line is given to guide the eye, with an R^2 given to quantify error in the fit.

When comparing the adsorption energy to the distances between the Brønsted proton and the zeolite (Fig. 6.4), we note that the adsorption energy is influenced by the distance of the Brønsted proton to the zeolite. Additional analysis to understand the chemisorbed state was done by using the O_{Zeo} - O_{DME} distance as a descriptor for the Brønsted proton interaction with both the active site and DME. Figure 6.4 shows a direct correlation between E_{ads} and the O_{Zeo} - O_{DME} distance, further highlighting the nature of the interactions that take place in the zeolite pores.

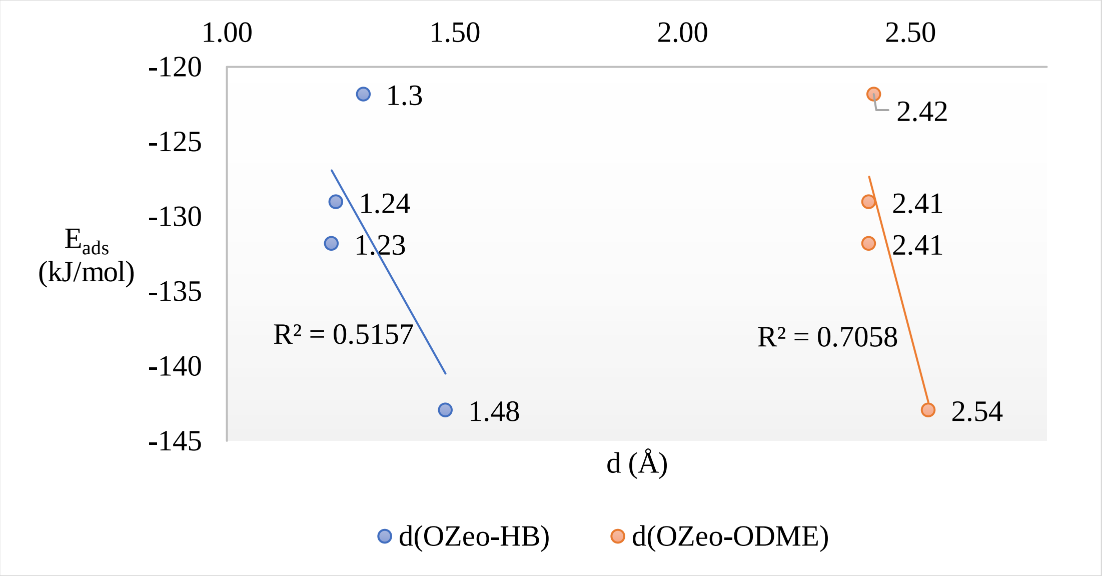

Figure 6.4. Plot of the distance (d) in Ångtroms, between the zeolite active site and the Brønsted proton, d(O_{Zeo}-H_B), or the DME molecule, d(O_{Zeo}-O_{DME}), with the adsorption energy (Eads), presented in kJ/mol, respectively. The lines are given to guide the eye, with an R^2 given to quantify error in the fit.

This correlation between the adsorption energy and geometric features surrounding the Brønsted proton may indicates that the interaction between the methyl groups of DME and the zeolite walls is limited, leaving the bonding of the oxygen (DME) to the active site to dominate the overall adsorption process. Therefore, the framework deprotonation energy (E_{dep}) of the empty zeolites and the proton affinity (E_{PA}) of DME (Table 6.3) were considered to compare the strength of the interactions exerted on the Brønsted proton. With this information, we are able to gain further understanding on the effects determining the zeolite deprotonation.

Table 6.3. Deprotonation energies (E_{dep}) of the empty zeolite clusters, proton affinity (E_{PA}) of DME and ion-pair interaction between protonated DME and zeolite site ($E_{ion-pair}$) presented in kJ/mol.

	E_{dep}		$E_{ion-pair}$
	This study	Theoretical[21]	This study
H-Y	1144	1081; 1166	-431
T12 [I2]	1131		-427
T4 [Z6]	1186		-457
T1 [M7]	1145		-430
	E_{PA}		
	This study	Experimental[22]	
DME	847	802	

The E_{dep} is calculated as 1144; 1186 kJ/mol using the B97-3 XC functional, which is in agreement with previous QM/MM work using the similar B97-2 XC functional for simulations of H-Y and H-ZSM-5, where the E_{dep} is 1081; 1166 kJ/mol.[21] The E_{PA} of DME is calculated to be 847 kJ/mol, which is also in good correspondence with the experimental PA of 802 kJ/mol determined at 300 K.[22]

Overall, the DME E_{PA} is ~300 kJ/mol less than the zeolite E_{dep} so that proton transfer is endothermic. Therefore, other factors must be considered as contributing to DME chemisorption. The highest E_{dep} is found for the T4 [Z6] site, followed by T1 [M7] > H-Y > T12 [I2], which indicates one factor influencing the complete deprotonation.

Further analysis on the bonding energy between the protonated DME and zeolite was considered, as discussed in the Methodology section, to clarify further the conditions affecting the stability of DME.

When analysing the bonding energy between the protonated DME and conjugated base active site ($E_{ion-pair}$), the T4 [Z6] has the highest bonding strength. When considering the deprotonation energy (E_{dep}) as a measure of basicity of the conjugated base active site, a direct correlation is noted between the stability of the DME ··· H^+ ··· zeolite complex, as shown in Figure 6.5.

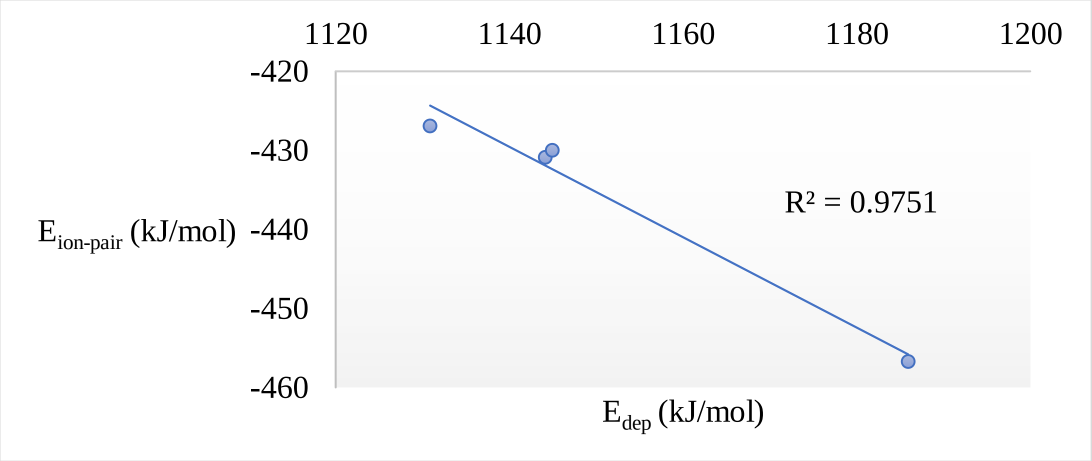

Figure 6.5. Plot of deprotonation energy (E_{dep}) against bonding strength of DME^+ to the zeolite conjugate base ($E_{ion\text{-}pair}$), presented in kJ/mol. The line is given to guide the eye, with an R^2 given to quantify error in the fit.

6.3.2. Vibrational frequency analysis

The vibrational frequencies analysis was conducted in order to clarify further our results and correlate them with IR experimental data. The vibrational frequencies for the O-H stretch were calculated in the interval of 1500-1600 cm^{-1} (Table 6.4), with the exception of the T12 [I2] model, which is 2174 cm^{-1}. The T12 [I2] anomaly is due to a smaller O-H bond. These calculated vibrational frequencies of the O-H bonds are within the limits of the experimental ABC triplet vibrational signature corresponding to the O-H…O interactions, present at the 1500-1700 cm^{-1}, 2100-2500 cm^{-1} and 2800-3000 cm^{-1} vibrational frequency intervals, when inserting DME in H-ZSM-5 and H-Y[23].

Table 6.4. Calculated IR vibrational frequencies summary of DME adsorbed in zeolites H-Y and H-ZSM5, specifically the hydrogen bonds of the Brønsted proton to the zeolite active site, O_{Zeo}-H_B, and DME, H_B-O_{DME} strech, alongside symmetric, mixed and asymmetric motion of both CH_3 groups of DME, with M_2 being the groups closest to the zeolite framework, given in cm^{-1}.

	$\upsilon(O_{Zeo}\text{-}H_B)$	$\upsilon(H_B\text{-}O_{DME})$				
H-Y	1511	1570				
T12 [I2]	1593	2174				
T4 [Z6]	1557	1592				
T1 [M7]	1513	1579				
	$\upsilon(CH_3)$					
	symmetric		mixed		asymmetric	
	M_1	M_2	M_1	M_2	M_1	M_2
H-Y	2960	2987	3069	3089	3114	3120
T12 [I2]	2989	2991	3097	3100	3140	3149
T4 [Z6]	2977	2984	3089	3093	3111	3119
T1 [M7]	2961	2965	3065	3079	3089	3107
$DME_{(g)}$	2865	2877	2920	2924	3039	3043
$DME^{+}_{(g)}$	2994	3079	3132	3151	3176	3199

IR experimental studies further confirm the existence of DME deprotonating H-ZSM-5, and in separate associated studies, the higher proportion of physisorbed DME in zeolite-Y[23], even with increasing adsorbate loadings. Figure 6.6 shows the O_{DME}-H_B distance plotted against the O_{DME}-H_B stretch vibrational frequency; a good correlation is observed between the O_{DME}-H_B bond and the corresponding vibrational frequency, which may be used to gain more insight about the interactions that occur in the zeolite pores with the adsorbate. The difference between the physisorbed and chemisorbed states are also reflected in the CH_3 frequencies in Table 6.4. The CH_3 frequencies show that when DME is protonated, they increase, similar to experimental IR reports.[23]

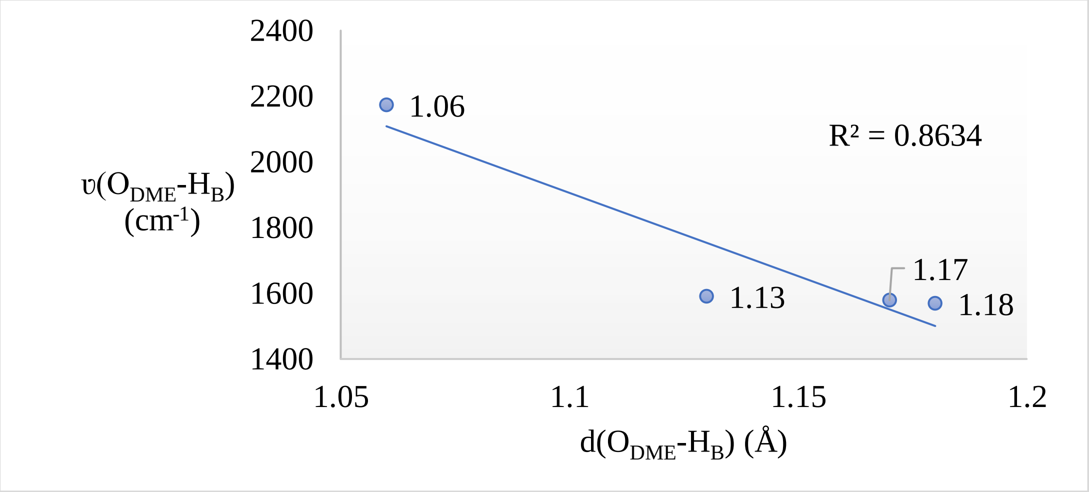

Figure 6.6. Plot of the O_{DME}*-*H_B *distance, d(*O_{DME}*-*H_B*) versus the* O_{DME}*-*H_B *stretch vibrational frequency* υ*(*O_{DME}*-*H_B*), presented in Ångtroms and* cm^{-1}*, respectively. The line is given to guide the eye, with an* R^2 *given to quantify error in the fit.*

6.3.3. Formation of DME

As mentioned in the Introduction, in addition to the methoxy formation from methanol discussed in the previous chapters, an alternative methanol conversion pathway was analysed, in order to understand more about the conditions influencing the methanol reactivity. The direct conversion of two methanol molecules to DME and water, was modelled at the T12 [I2] position ,where the highest interaction energy with methanol is calculated (E_{ads}= -142 kJ/mol – Table (3.4);Chapter (3)), which shows that open sites are better for adsorption, with the overall activation barrier determined as 238 kJ/mol.

As discussed in Chapter 3, the adsorption energy of an individual methanol molecule on the T12 [I2] site was -120 kJ/mol, and for the second methanol, the adsorption energy is -86 kJ/mol. Here, we have continued our simulations from the bidentate configuration of the two methanol molecules (R stage). A nudged-elastic band was used to model the reaction pathway to the final DME and water products. In the initial stages of the NEB, the methyloxonium rotates to align its methyl towards the oxygen of the second methanol (Rot stage). Afterwards, the C-O bond breaks to form methyl and water (B stage) leading to an overall activation energy (E_a) of 238 kJ/mol, followed by the formation of DME and water (P stage) with an exothermic stabilisation of -191 kJ/mol. The subsequent energy to desorb the two products is 152 kJ/mol. A comparison of the energy pathway with different studies is presented in Figure 6.7.

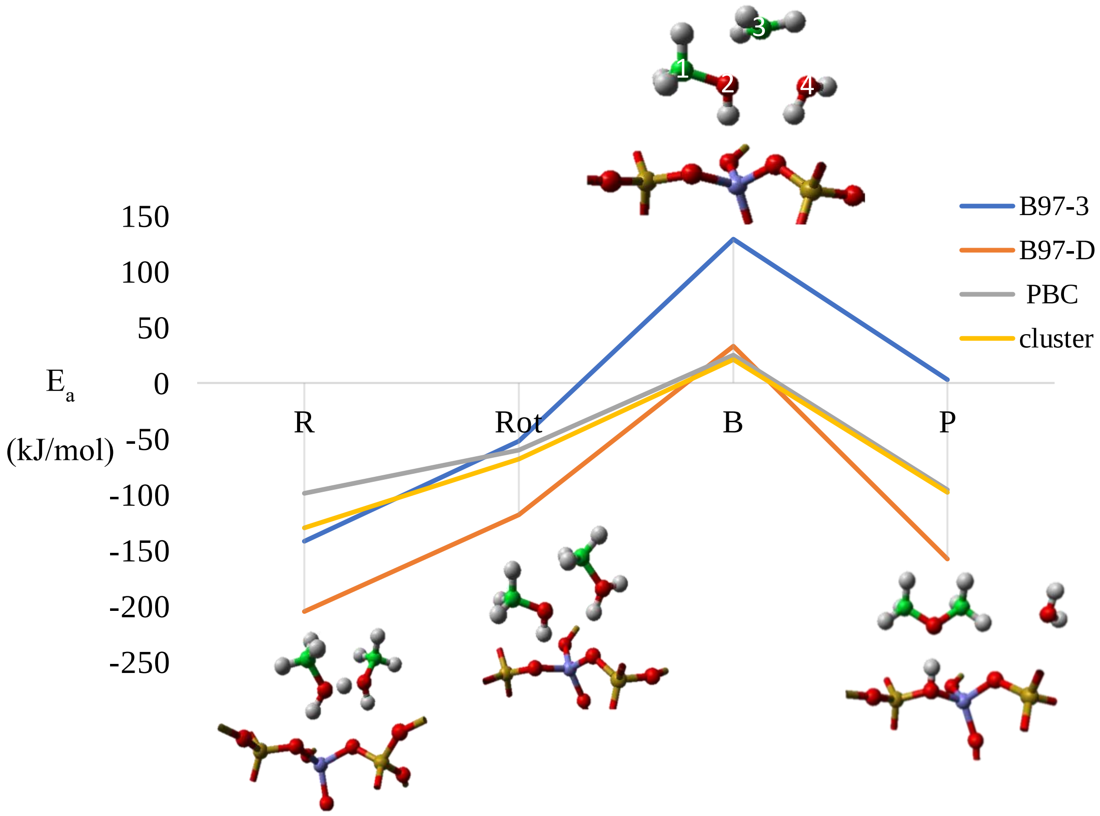

Figure 6.7. Theoretical results from small cluster[6], PBC2 and this study modelled with B97-3 and B97-D XC functionals, comparison of reaction pathway for direct conversion of bi-methanol to DME and water, at the T12 [I2] active site, with the main reaction steps illustrated, specifically R and P labels representing the adsorption of the two methanol reactants and dimethyl ether and water stages, Rot - the rotation of reactants stage, B - breaking of methanol C-O bond stage.

Previous small cluster and PBC simulations,2,[6] reported a reaction pathway with the Brønsted proton transferring back to the zeolite active site during the methanol rotation

(Rot stage) and remains there prior to the C-O bond breaking and formation of water (B stage). Furthermore, in the transition state, the methyl is closer to the methanol in the previous small cluster and PBC studies (~ 2 Å) than in our simulations (2.13 Å). These differences could be due to a different level of theory used, specifically, small cluster theoretical studies (DFT, NL-LDA, DZVP level of theory)[5],[6] with an activation energy of 151 kJ/mol, and PBC simulations in H-ZSM-22 (DFT, rev-PBE, PAW level of theory)2 with a barrier of 124 kJ/mol (Table 6.5). In the previous work, the presence of the Brønsted proton on the active site during methanol rotation may facilitate a smoother transition trough the Rot stage. In contrast, experimental studies see a higher conversion rate of methanol is achieved when having an active site with a higher acidity2 or a zeolite environment with a higher acid site density1, illustrating how proton transfer to the methanol could be influential in real systems. Since a higher acidity lowers the activation barrier, in turn it is clear that the transition state is most stabilised by the proton transfer, not the conjugate base.

Table 6.5. Comparison of energetic and geometric observables of the reaction path of methanol condensation to DME and water, with R and P labels representing the adsorption of the two methanol reactants and dimethyl ether and water stages, Rot - the rotation of reactants stage, B - breaking of methanol C-O bond stage and Des - desorption of products, with scheme clarifying the geometric observables provided in Figure 6.7.

	Energetics				
	R	Rot	B	P	Des
B97-3	-142	90	181	-126	92
B97-D corrected	-205	87	151	-191	152
PBC2	-99	39	85	-121	77
cluster[6]	-130	62	89	-119	83
	Geometric observables				
	d(C1-O2)	d(O2-C3)	d(C3-O4)		
B97-3	1.43	2.13	2.35		
PBC2	1.47	1.97	2.04		
cluster[6]	1.45	1.99	1.95		

6.4 Conclusions

In this chapter, we have first employed QM/MM simulations to model the adsorption of DME on several acid sites in zeolites H-Y and H-ZSM-5. DME bonds to the active site in an intermediary state between physisorption and chemisorption, highlighting a very broad and shallow potential energy surface for proton the transfer from the acid site to DME. The complete proton transfer is achieved at the T12 [I2] site in H-ZSM-5, which we suggest depends on the deprotonation energy of the acid site and the open configuration of DME at the active site. The strength of the zeolite conjugate base active site was shown to influence the stability of the protonated DME at the active site by the direct correlation found between the deprotonation of the active site and the ion-pair bonding energies. Vibrational frequencies analysis found that the geometry and types of interactions match with experimental data on O - H ··· O vibrational frequencies.

In addition, the direct conversion of methanol to DME was investigated and the reaction pathway determined was different from previous reports. Our work showed that the active site remained unprotonated, whereas previous work had the proton stabilising on the zeolite during the transition from methanol to DME. Our new observations shows the importance of the acidity and conjugate base formed, on the alignment of the methanol reactant prior to the main transition state (B stage).

Further investigations are necessary to determine the influence of the configuration of DME on the deprotonation of the active site and their role on the subsequent transformation of DME to olefins.

References:

1 J. R. Di Iorio, C. T. Nimlos and R. Gounder, *ACS Catal.*, 2017, **7**, 6663–6674.
2 P. G. Moses and J. K. Nørskov, *ACS Catal.*, 2013, **3**, 735–745.
3 U. Olsbye, S. Svelle, M. Bjørgen, P. Beato, T. V. W. Janssens, F. Joensen, S. Bordiga and K. P. Lillerud, *Angew Chem Int*, 2012, **51**, 5810–5831.
4 T. Fujino, M. Kashitani, J. N. Kondo, K. Domen, C. Hirose, M. Ishida, F. Goto and F. Wakabayashi, *J. Phys. Chem.*, 1996, **100**, 11649–11653.
5 S. R. Blaszkowski and R. A. van Santen, *J. Am. Chem. Soc.*, 1996, **118**, 5152–5153.
6 S. R. Blaszkowski and R. A. van Santen, *J. Phys. Chem. B*, 1997, **101**, 2292–2305.
7 S. Grimme, *Journal of Computational Chemistry*, 2006, **27**, 1787–1799.
8 M. Valiev, E. J. Bylaska, N. Govind, K. Kowalski, T. P. Straatsma, H. J. J. Van Dam, D. Wang, J. Nieplocha, E. Apra, T. L. Windus and W. A. De Jong, *Comp Phys Com*, 2010, **181**, 1477–1489.
9 T. W. Keal and D. J. Tozer, *J Chem Phys*, 2005, **123**, 121103.
10 G. Henkelman, B. P. Uberuaga and H. Jónsson, *J Chem Phys*, 2000, **113**, 9901–9904.
11 M. F. Guest, I. J. Bush, H. J. Van Dam, P. Sherwood, J. M. H. Thomas, J. H. Van Lenthe, R. W. Havenith and J. Kendrick, *Molec Phys*, 2005, **103**, 719–747.
12 A. A. Sokol, S. T. Bromley, S. A. French, C. R. A. Catlow and P. Sherwood, *International Journal of Quantum Chemistry*, 2004, **99**, 695–712.
13 W. Jost, *J. Chem. Phys.*, 1933, **1**, 466–475.
14 R. Poloni and J. Kim, *Journal of Materials Chemistry C*, 2014, **2**, 2298–2300.
15 David Lesthaeghe, Veronique Van Speybroeck, Guy B. Marin and Michel Waroquier, *Angew Chem Int*, 2006, **45**, 1714–1719.
16 G. Pope, *J Chem Soc Faraday Trans*, 1993, **89**, 1139–1141.
17 T. Omojola, N. Cherkasov, A. McNab, D. Lukyanov, J. Anderson, E. Rebrov and A. van Veen, *Catal Let*, 2018, **148**, 474–488.
18 R. S. Michael C. Payne and J. D. Gale, *The J Phys Chem B*, 1997, **101**, 4787–4797.
19 T. R. Forester and R. F. Howe, *J. Am. Chem. Soc.*, 1987, **109**, 5076–5082.
20 Z. Luz and A. J. Vega, *J. Phys. Chem.*, 1986, **90**, 4903–4905.
21 A. J. O'Malley, A. J. Logsdail, A. A. Sokol and C. R. A. Catlow, *Faraday Discuss.*, 2016, **188**, 235–255.
22 B. J. Smith and L. Radom, *J. Am. Chem. Soc.*, 1993, **115**, 4885–4888.
23 A. Zecchina, S. Bordiga, G. Spoto, D. Scarano, G. Spanò and F. Geobaldo, *J. Chem. Soc., Faraday Trans.*, 1996, **92**, 4863–4875.

Chapter 7. Summary, conclusions and future work

The initial stages of the Methanol-to-Hydrocarbons process were investigated using state-of-the-art computational techniques to describe the methanol conversion paths and further methoxy reactivity. Our study highlighted the crucial role of methanol loading on lowering the activation barrier for methoxylation by spontaneously deprotonating the active site. In addition, the reactant loading coupled with vicinal active sites determine a concerted polarization effect that lowers the methoxylation barrier. These results highlight the importance of acid site configuration in the zeolite catalyst and indicate a potential condition useful in catalyst design. The zeolite framework bonded methoxy groups were shown to be very stable, without any direct mechanism being involved in the formation of carbene compounds. However, the carbene moieties were very stable which indicates their potential involvement in either the direct formation of hydrocarbons or even migration from one active site to another. Finally, the stability and formation of dimethyl ether investigation showed that dimethyl ether is able to chemisorb and physisorb depending on the zeolite acid site which further emphasises the importance of the active site type in the zeolite catalyst.

Summary, conclusions and future work

Our study has had a strong focus on methoxylation, including the challenges posed by the observation of the process at room temperature, which we have investigated using state-of-the-art computational modelling techniques, to describe accurately the interactions occurring in the zeolite environment. Further analysis was conducted on the methoxy groups to understand their potential involvement in the production of hydrocarbons and on the formation and stability of dimethyl ether (DME) from methanol on several acid sites.

As presented in Chapter 3, our investigation started by employing static QM/MM methods to simulate the adsorption of methanol on several potential active sites of zeolites H-ZSM-5 and H-Y. A high methanol loading was found to lead to the deprotonation of the acid site, bringing the reactant closer to the transition state. Vibrational frequency analysis on these models highlighted the existence of the ABC triplet vibrational signature characteristic of the H-O-H interaction. The symmetric and asymmetric H-O-H stretch frequencies were shown to be useful in gaining insight about the closeness of the methanol molecules to each other and to the zeolite pores.

Because no mechanisms for spontaneous methanol conversion were identified in Chapter 4, Molecular Dynamics (MD) techniques were used to model the reaction environment closer to the reported experimental conditions leading to the formation of methylated ZSM-5, specifically, a methanol loading of up to five molecules and two acid sites per H-ZSM-5 unit cell. The MD simulations at room temperature showed that the methanol molecules would form stable hydrogen bonded clusters for the entire production run. In addition, these clusters would deprotonate the zeolite and stabilise the Brønsted proton in the middle of the cluster, in a Zundel configuration. The effect of the paired acid sites was emphasized when using enhanced MD simulations; Metadynamics (MTD) techniques were used to increase the speed of the sampling process and in the same time to map out the free energy surface of the methoxylation reaction in order to extract the activation barrier for methoxylation. The barriers obtained from the MTD simulations showed that varying the methanol loading had no significant effect on the conversion of methanol on an isolated acid site. Only when there are paired acid sites does a high reactant loading have an impact on the activation barrier. After deprotonating both acid sites and forming a methanol cluster in between the new zeolite conjugate bases, a polarisation effect along the methanol hydrogen bonds occurs that aids the breaking of the C-O bond and formation of methylated zeolite. Since the lowest activation barrier found was 119 kJ/mol, we suggest that future analysis on the methoxylation process should take into account the effect of framework defects such as silanol nests or extra-framework aluminium sites, as potential conversion centres for methanol. As a complementary study, the use of dealuminated zeolites or with extra-framework cations in an experimental setup would uncover the role of structure defects in the methoxylation process.

Additional analysis was conducted in Chapter 5, on the likely involvement of the methoxy groups on the formation of hydrocarbons by determining the possibility of two methyl groups migrating and stabilising next to each other in order to react. Two reaction pathways were modelled with QM/MM methods, in which methyl either was formed outside the active site or migrated from the active site to another one. Both cases were shown to be energetically unfavourable and thus excluded. As an alternative pathway, the conversion of methoxy to carbene with further migration was analysed. Although the reaction energy for carbene migration was smaller than that of methoxy, the conditions leading to carbene formation remain unclear. Future work would involve the manner in which the methyl migration might be aided by the effect of impurities such as methane or water, and the possibility of the impurities contributing to the formation of carbene from methoxy. Also, a direct mechanism involving a spontaneous hydride transfer from the methyl group of a protonated methanol could be investigated as an alternative pathway.

In addition to the methyl formation from methanol, in Chapter 6 we also analysed the reaction pathway leading to DME from methanol. A QM/MM study was conducted to determine the characteristics of the active sites that would stabilise DME by measuring the adsorption energy of DME on several acid sites of H-ZSM-5 and H-Y. Our geometry optimised models showed that DME was chemisorbed and deprotonated the zeolite framework. This phenomenon was attributed to the orientation of DME that would induce a high polarisation effect on the Brønsted proton and low deprotonation energy of the zeolite acid site. The vibrational frequency analysis highlighted a correlation between the O-H stretch frequency and the distance between the adsorbate to the adsorbant, similar to the previous QM/MM methanol case. The NEB method was used to convert methanol to DME and compared to previous reports. The reaction pathway modelled in our simulation resulted in a higher activation barrier (238 kJ/mol) than PBC (124 kJ/mol) and small cluster (151 kJ/mol) simulation studies. This difference was attributed to the transition state having the methyl group stabilised in a tilted orientation than that found by previous reports. Future work will be based on having a wider range of configurations of the initial and final state to try and find a lower saddle point on the PES of DME formation, possibly extended to MTD simulations.

To summarise, the methanol conversion was shown to be significantly influenced by the synergetic effect between paired active sites in the zeolite framework and reactant loading. The T12 site, due to its large open space available at the channel intersection, stabilises both methanol and DME, better than other sites discussed in this thesis. Finally, the reactivity of methoxy groups analysis highlighted the possibility carbene migration and participation on the formation of hydrocarbons process. Although a thorough investigation on the room temperature spontaneous methoxylation and carbene formation was conducted, the exact conditions aiding this phenomenon remain elusive. Future work on these topics would entail a more extensive analysis on a broader range of potential active sites present in the zeolite framework such as sylanol nests and external. In addition, a more comprehensive mechanistic investigation involving hydride transfer may uncover new reaction routes. Experimental work on spontaneous room methoxylation and carbene migration would focus on studying the effect of acid site density in an isolated or paired configuration. This would confirm or disprove the concerted mechanism of the paired acid sites involved on the activation of methanol and would highlight the feasibility of C1 species migration.